

博士論文

Iodine-129 in natural archives as historical
records of human nuclear activities
(天然アーカイブに記録された人為起源ヨ
ウ素 129 の分析)

Bautista, Angel Tugade, VII
バウテイスタ エンジェル トウガデ 七世

Acknowledgements

I would like to express my deepest gratitude to the following, for none of these would be possible without their help and support:

The Philippine Nuclear Research Institute – Department of Science and Technology, my home institution, for officially nominating and sending me to Japan to take PhD studies, and supporting me in all my endeavors for the past three years.

The School of Engineering, The University of Tokyo, for generously providing my scholarship, which made it possible for me to study in this prestigious university as well as live a comfortable life here in Japan.

The Micro Analysis Laboratory, Tandem Accelerator (MALT): first and foremost, Matsuzaki-sensei, my adviser and mentor, as well as all staff and students, for the guidance, help, support, and most importantly, the wonderful friendship that has continuously deepened for the past 3 years. My life and studies in Japan have been so wonderful because of all of you. Thank you.

To Prof. Siringan and his team in the Marine Science Institute, University of the Philippines Diliman, for sharing their coral samples from the Philippines and advising me in their proper handling and treatment and to their constant inputs throughout the study.

To Prof. Iizuka and his team in Hokkaido University for sharing their ice core samples from Greenland as well as to Prof. Horiuchi of Hirosaki University for advising and assisting us in the proper handling and treatment of samples.

To my doctoral thesis panel, Prof. Saito, Prof. Sakaguchi, Prof. Terai, and Prof. Yokoyama, for their time and effort and for giving their thoughts and comments. All these have greatly helped me improve my research.

To my parents (Mama and Papa), family, and friends (special mention – Zenith and Ralph; and the whole AFSJ family), who have been with me in the ups and downs of this whole three years, Thank you very much and I share this success with all of you. I wouldn't have been able to do this without you.

And lastly, to the One who made all of these possible:
Thank you very much, Lord. All of these come from you.
May I proclaim your love and glory through my works.

Abstract

Iodine-129 ($T_{1/2} = 15.7$ Ma) is a long-lived fission product that, while produced naturally in the environment, is released by human nuclear activities (HNA) such as nuclear bomb testing, nuclear fuel reprocessing (NFR), and nuclear accidents in massive amounts. Its behavior in the environment is conservative and generally known, where it is mainly transported through atmosphere and ocean circulations. Given its long half-life and the current understanding of its sources and behavior in the environment, ^{129}I is considered a good environmental tracer of HNA-derived radionuclides and the earth processes associated with its transport and cycling. These applications are used and demonstrated in the analysis of ^{129}I in natural archives such as coral, ice, and sediment core records. However, the current number of published ^{129}I records is sparse and a lot remains to be studied to explore the full potential of these applications of ^{129}I in natural archives.

In this regard, the main objective of this dissertation is to generate ^{129}I time series records in two coral cores from the northern hemisphere (Philippines) and in an ice core from the southeast dome (SE-Dome) in Greenland to explore the following applications of ^{129}I in natural archives: (1) as proxy for HNA that can be used to reconstruct the degree of influence of HNA in locations where archives are taken; (2) as a tracer of atmosphere and ocean circulations that transport ^{129}I from its sources to the locations of the archives; and, (3) as a time marker that can establish or confirm the age models of these natural archives.

To achieve this goal, a method capable of measuring ^{129}I and ^{127}I in about 1-4g of coral samples first needed to be developed. Once achieved, ^{129}I time series of two coral cores from the Pacific Ocean (Baler) and South China Sea or SCS (Parola) sides of the Philippines are constructed and compared to historical records of known HNA

and existing southern hemisphere ^{129}I coral records. Given that almost all HNA were performed in the northern hemisphere, stronger ^{129}I signals are expected in corals from the northern hemisphere. Subsequently, ^{14}C in the same corals were analyzed and compared with the observed ^{129}I signals as well as with other published ^{14}C coral records. ^{14}C in corals are more extensively studied as time marker and an oceanographic tracer and thus provide context into the capabilities of ^{129}I in terms of the said applications. Comparison between ^{129}I and ^{14}C is subsequently done in more detail through a box mixing model capable of simulating radionuclide concentrations in Baler and Parola. Lastly, ^{129}I is analyzed in an ice core from the SE-Dome site in Greenland to demonstrate the applicability of ^{129}I in an entirely different archive type. Ice/coral comparisons are complementary because they show ^{129}I signals from land/marine conditions and from high/low latitudes, respectively.

Results show that the coral ^{129}I measurement method developed in this study was capable of measuring $^{129}\text{I}/^{127}\text{I}$ in 1-4g of samples with errors of about 23% for natural-aged (pre-1950) samples and about 9.6% and 13.5% for anthropogenic-aged (post-1950) samples in Baler and Parola, respectively. This is comparable to the work of Biddulph et al. (2006), which had errors of about 35% and 8% natural and anthropogenic-aged samples, respectively, using 10-30g of corals. This was accomplished by modifying the method of Biddulph et al. (2006) in two aspects: (1) the use of inductively coupled plasma mass spectrometry (ICP-MS) instead of ISE for stable ^{127}I measurement. ICP-MS matrix effect was minimized by using ^{133}Cs internal standard and finding an optimal dilution factor for sample solutions. A 286x dilution was eventually used, which was the largest dilution that resulted to a concentration higher than the method's limit of quantification of 0.27 ppb; and (2) the addition of 0.66 mg of low-ratio iodine carrier in the preparation of target for AMS analysis,

instead of using carrier-free method. 0.66 mg of carrier was the smallest amount that forms sufficient amount of AgI for AMS measurement. It was found that error levels increase exponentially with decreasing sample size, as estimated by the equation $y = 3.6338 \ln x + 15.609$ of $1/\text{RSD}$ vs. resulting ratio of the AgI precipitate (sample + carrier). Given this, this method can achieve a target error level of about 10% with as little as 1.5 g and 22.5 g for anthropogenic- and natural-age coral samples.

^{129}I in corals from the Philippines was found to record human nuclear activities in good detail. Nearly identical bomb peaks in 1962 were observed in both Baler and Parola ($^{129}\text{I}/^{127(\text{stable})}\text{I} \sim 31.5 \times 10^{-12}$) – a potential time marker, comparable or possibly even better than the coral ^{14}C bomb curve. Nuclear fuel reprocessing and Chernobyl accident signals in 1977, 1980, and 1986 were also observed concurrently in Parola and with 9 to 11-year lags in Baler. This time lag suggests that ^{129}I reaches the South China Sea and Pacific Ocean sides of the Philippines from the atmosphere and through Pacific Ocean currents, respectively. Lastly, anomalously high $^{129}\text{I}/^{127}\text{I}$ levels were found in Parola (i.e., 22.8 to 38.9×10^{-12}), contrary to the decreasing trend observed in Baler and in published ^{129}I emission records. This finding possibly reveals unknown nuclear activities performed around the South China Sea region. These results demonstrate how ^{129}I in coral samples the Pacific Ocean (Baler) and South China Sea (Parola) sides of the Philippines provide information about how HNAs affected the country, given the different atmospheric and oceanic regimes around the country and the region.

Comparison between ^{129}I and ^{14}C is demonstrated through the box mixing model that simulated the two radionuclides in Parola and Baler. Results show that the difference between the atmosphere-to-ocean lifetimes of ^{129}I and ^{14}C is the largest factor for the observed trends in the two nuclides. In particular, the quicker (i.e., 2

years) atmospheric lifetime of ^{129}I causes a sharper, more robust bomb peak that is uniform in timing and shape, regardless of the oceanic processes in the location of the coral. The longer atmospheric lifetime (i.e., 300 years, for this model) of ^{14}C causes the broad bomb curve, which is sensitive to ocean processes, causing variations in the ^{14}C bomb curve's timing and shape. The plausibility of specific mechanisms for both ^{129}I and ^{14}C were also demonstrated, particularly: (1) "SP intrusion" (i.e., intrusion of lower- ^{14}C South Pacific waters to the North Equatorial Current (NEC), which supplies the source water in Baler) and "quick input" (i.e., a small portion of the bomb-produced ^{14}C with a form other than CO_2 that has a significantly quicker atmospheric lifetime), which causes the delay of the Baler ^{14}C bomb curve and the small pre-bomb curve peak, respectively; (2) the 1976 PDO shift (i.e., the increased contribution of northern subtropical waters and the increased upwelling in the Central American region, both due to the northward shift of the NEC bifurcation latitude), which caused the sudden jump in coral $\Delta^{14}\text{C}$ in 1976.; and (3) ^{129}I signal delay of the NFR and Chernobyl ^{129}I signals between Parola and Baler, as a result of different pathways wherein ^{129}I entered the South China Sea directly from the atmosphere, while it traveled from the North Pacific to the Baler site through the prevailing ocean currents.

These results demonstrate that coral ^{129}I records human nuclear activities, namely, nuclear bomb tests, nuclear fuel reprocessing, and nuclear accidents better than the more extensively studied ^{14}C . As a time marker, the coral ^{129}I bomb peak is also clearly better than the coral ^{14}C bomb curve because, as shown in the measurements and validated with the box mixing model, ^{129}I bomb peak appears almost in the same year as the time of atmospheric release and it is hardly affected by ocean processes primarily because of its short atmospheric lifetime. Coral ^{14}C bomb

curves, in contrast, vary in timing, shape, and magnitude depending on the oceanic processes in the location of the coral, as a consequence of the long atmospheric lifetime of ^{14}C . Nonetheless, the large difference in atmospheric lifetimes of ^{129}I and ^{14}C has caused these radionuclides to have distinct applications as oceanic tracers: coral ^{129}I signals are able to trace the speed of ocean circulation, as demonstrated by the timing discrepancy in NFR and Chernobyl signals between Parola and Baler; coral ^{14}C , on the other hand, are able to reflect large and long-term scale changes in circulation such as SP intrusion and the effects of the ENSO phases and the 1976 PDO shift.

Lastly, ^{129}I in an ice core from the Southeast (SE) dome of Greenland similarly demonstrated that ^{129}I signals from nuclear bomb testing and NFR are recorded concurrently in the ice core, specifically in years 1958, 1961, 1962 and 1965, 1969, 1972, respectively. This demonstrates that ^{129}I can also be used as a HNA proxy and a time marker not only for corals, but also for ice cores. ^{129}I thus effectively provides a direct link between two entirely different archives: coral/ice core, low/high latitude locations, and marine/land environments. The “anchor points” that these ^{129}I signals provide will enable researchers to establish/confirm their age models, and directly compare ^{129}I (and other analytes or parameters, by extension) records between different ice and coral cores, with increased confidence. Some possible environmental tracer applications that may be explored in the future, once the whole Greenland SE dome ^{129}I ice core record has been constructed, include analysis of bomb signals between Soviet and US tests, which may reveal information about the stratospheric transport of bomb test radionuclides from the Soviet and US test sites to the ice core location; and comparison from the existing Alpine ice core ^{129}I record, which may

reveal interesting atmospheric circulation patterns since Greenland and the Alpine region are located in opposite sides of the European NFR facilities.

Integrating these results, the main contributions of this dissertation are: (1) it has demonstrated that ^{129}I in coral and ice cores are excellent proxies of HNAs, particularly nuclear bomb testing, nuclear fuel reprocessing, and nuclear accidents, recording these activities in these natural archives with unprecedented detail. Thus, ^{129}I in these archives can be used to assess the effect of HNAs in the locations where the archives were taken (i.e., The Philippines and Greenland); (2) that ^{129}I in these archives also provide pertinent information about the atmospheric and oceanic pathways that HNA-derived radionuclides take from the point of release to the locations where natural archives were taken. This information can be used for nuclear safety and security in the event of future nuclear incidents and/or for studying these associated earth processes; and (3) it has demonstrated that ^{129}I in coral and ice cores provide an excellent time marker that can establish and confirm the age models of the archives as well as provide an “anchor point” that will enable us to directly relate and compare different coral and ice records. In the case of the coral archives, these applications were demonstrated in comparison to the better-known ^{14}C , which provided context and made these important applications of ^{129}I more apparent.

I believe that the results presented in this dissertation will interest studies of ^{129}I in coral and ice cores in different locations to confirm the ubiquity of the observed ^{129}I signals and their possible applications. I also believe that this dissertation will encourage investigations to ascertain the source and the possible oceanographic tracer application of the high ^{129}I levels in the South China Sea. Moreover, it may start a review of the available coral ^{14}C records, in light of the new mechanisms proposed here, particularly the SP intrusion and the quick input. These findings merit that both

^{129}I and ^{14}C be studied side-by-side in more corals from other locations to fully explore the potential of their applications. We also recommend that higher resolution and more sophisticated modeling studies be conducted for these radionuclides, given that some aspects (e.g., SP intrusion) were not modeled sufficiently in this work. More in-depth studies and representation of the mechanisms proposed in this dissertation would largely contribute to the better understanding of the dynamics and possible applications of these radionuclides in the management of nuclear energy and technology and in the study of earth processes and the environment.

Table of Contents

Acknowledgments	ii
Abstract	iii
List of Figures	xiii
List of Tables	xvi
Summary of Abbreviations	xvii
1. Introduction	1
2. Literature Review	5
2.1. Sources of ¹²⁹ I.....	5
2.1.1. Natural	5
2.1.2. Human nuclear activities	7
2.1.2.1. Nuclear weapons testing.....	7
2.1.2.2. Nuclear fuel reprocessing	8
2.1.2.3. Nuclear accidents.....	9
2.1.2.4. Known effects of HNA to the Philippines.....	20
2.2. ¹²⁹ I in the environment.....	20
2.3. ¹²⁹ I in natural archives	27
2.4. ¹⁴ C in corals	28
3. Materials and Methods	35
3.1. Corals.....	35
3.1.1. Samples and study sites	35
3.1.2. Age model	35
3.1.3. ¹²⁹ I measurement	36
3.1.3.1. Method Development	36
3.1.3.2. ¹²⁹ I measurement method summary.....	39

3.1.4. ^{14}C measurement	44
3.1.5. Box mixing model description	44
3.2. Ice core	52
3.2.1. Sample, study site, and age model.....	52
3.2.2. Sample treatment and ^{129}I measurement.....	52
4. Results and Discussion	54
4.1. Method development of $^{129}\text{I}/^{127}\text{I}$ measurement in corals	54
4.1.1. ^{127}I measurement	55
4.1.2. ^{129}I measurement	60
4.1.3. Coral $^{129}\text{I}/^{127}\text{I}$ results	61
4.2. ^{129}I in corals from the Philippines.....	66
4.2.1. Natural (pre-1950)	66
4.2.2. Bomb (1951-1976)	68
4.2.3. Nuclear Fuel Reprocessing (NFR) and the Chernobyl Accident (1977- 1996).....	69
4.2.4. Post-1996	70
4.3. ^{14}C in corals from the Philippines.....	72
4.3.1. Parola	78
4.3.2. Small pre-bomb peak.....	79
4.3.3. Baler	84
4.4. Box mixing model	92
4.4.1. ^{14}C and ^{129}I trends based on atmospheric lifetime.....	92
4.4.2. Specific coral ^{14}C trends.....	95
4.4.2.1. Intrusion of South Pacific waters.....	95
4.4.2.2. Quick input	97

4.4.2.3. PDO effect (upwelling and Kuroshio recirculation).....	97
4.4.3. Specific coral ¹²⁹ I trends	99
4.4.3.1. Pre-1962 ¹²⁹ I signals	102
4.4.3.2. Nuclear fuel reprocessing and Chernobyl accident signals	103
4.5. ¹²⁹ I in the Greenland Southeast Dome ice core	106
5. Summary and Conclusions	110
References.....	117
Appendix.....	126

List of Figures

Figure 1. Global inventories and fluxes of natural ^{129}I at steady state.	6
Figure 2. Aboveground nuclear bomb testing in megaton (Mt) fission yield.	10
Figure 3. Locations of nuclear bomb test sites per country.....	10
Figure 4. Portion of radionuclides (in Mt fission yield) injected to (a) local and regional, (b) troposphere, and (c) stratosphere by nuclear bomb tests.	11
Figure 5. Schematic diagram of transfers between atmospheric regions and the earth's surface of bomb-derived radionuclides.	12
Figure 6. General circulation of the stratosphere.	13
Figure 7. Average deposition of bomb-derived ^{90}Sr in the northern and southern hemisphere, and per 10° latitude band (inset).	14
Figure 8. General process of nuclear fuel reprocessing.....	14
Figure 9. Locations of notable NFR facilities and the Chernobyl Accident.	15
Figure 10. Airborne ^{129}I emissions of notable NFR facilities.....	16
Figure 11. Atmospheric deposition modeling of airborne ^{129}I from (a) Sellafield and (b) Mayak NFRs in year 2004.	18
Figure 12. Comparison of airborne and liquid ^{129}I releases of La Hague and Sellafield.	19
Figure 13. The global iodine cycle.	23
Figure 14. Global ocean circulation.	23
Figure 15. ^{129}I as tracer of Arctic and North Atlantic Ocean circulations.....	24
Figure 16. ^{129}I in (a) coral, (b) ice, and (c) sediment archives.....	25
Figure 17. Mean observed atmospheric ^{14}C globally (solid line) and in the northern (N.H) and southern (S.H.) hemispheres.	33
Figure 18. The global carbon cycle.	33

Figure 19. Some published (a) ^{14}C coral records and (b) their locations. Coral record details are shown in Table 3.	34
Figure 20. Locations of human nuclear activities, coral records, and major wind and ocean currents.	40
Figure 21. X-ray images of the (left) Baler and (right) Parola corals.	42
Figure 22. Iodine solvent extraction procedure.	43
Figure 23. Boxes of the mixing model.	49
Figure 24. Schematic diagram of the box mixing model.	50
Figure 25. Coral sample weights (in grams) used in this study.....	54
Figure 26. (a) $^{127}\text{I}/^{133}\text{Cs}$ (cps) and (b) ^{127}I in coral (ppm) with increasing dilution factor.	58
Figure 27. ^{127}I concentrations of (a) analyzed (diluted; in ppb) sample solutions and (b) corresponding concentration in ppm of coral.	59
Figure 28. ^{127}I (ppm) in Baler and Parola coral cores and their corresponding errors (1σ).	60
Figure 29. $^{129}\text{I}/^{127}\text{I}$ ratios of AgI precipitate (sample + carrier) in $\times 10^{-14}$	63
Figure 30. $^{129}\text{I}/^{127}\text{I}$ of Corals and their corresponding errors (1σ).	64
Figure 31. Relative standard deviation (RSD) vs. ratio of AgI precipitate.	65
Figure 32. ^{129}I from nuclear activities and as observed in coral records.	67
Figure 33. $\Delta^{14}\text{C}$ of the Parola and Baler corals compared with other published coral $\Delta^{14}\text{C}$ records from (a) locations inside and along the gyres and (b) in equatorial regions.	73
Figure 34a. Locations of ^{14}C coral records and prevailing ocean currents.....	74
Figure 35. $^{129}\text{I}/^{127}\text{I}$ ($\times 10^{-12}$) and $\Delta^{14}\text{C}$ (‰) of corals from Parola and Baler.	83
Figure 36. Upwelling regions.	88

Figure 37. El Niño Southern Oscillation (ENSO) index.	89
Figure 38. Schematic diagram of the migration of the latitude of bifurcation of the North Equatorial Current (NEC).	90
Figure 39. Pacific Decadal Oscillation (PDO) index.	91
Figure 40. PDO index regressed with sea surface temperature (SST) and sea level pressure (SLP).	91
Figure 41. Coral (a) ^{14}C and (b) ^{129}I bomb curve for Parola and Baler reproduced by the box mixing model.	94
Figure 42. Simulated ^{14}C and bomb curve for Parola and Baler with (dark lines) SP intrusion effect; (light lines) SP intrusion with quick input effect.	96
Figure 43. Simulated (a) ^{14}C and (b) ^{129}I bomb curve for Parola and Baler with SP intrusion, quick input, Kuroshio recirculation, and upwelling processes.	100
Figure 44. Simulated (a) ^{14}C and (b) ^{129}I bomb curve for Parola (red) and Baler with (dark blue) and without (light blue) SP intrusion.	101
Figure 45. Pre-1962 ^{129}I signals simulated by the box mixing model for Parola and Baler.	103
Figure 46. NFR and Chernobyl ^{129}I signal delay between Parola (red) and Baler (blue) simulated by box mixing model.	105
Figure 47. ^{129}I in the Greenland SE-Dome ice core (in 10^3 atoms/mL H_2O) and its corresponding errors (1σ).	108
Figure 48. Ice core records and HNA sources.	109

List of Tables

Table 1. Sources and inventories of ^{129}I in the environment.	5
Table 2. Summary of parameter values used in the box mixing model.	51
Table 3. Details of $\Delta^{14}\text{C}$ coral records from this study and previously published.	77

Summary of Abbreviations

AMS – Accelerator Mass Spectrometry

ENSO – El Niño Southern Oscillation

FFS – French Frigate Shoals

HNA – Human Nuclear Activities

ICP-MS – Inductively Coupled Plasma Mass Spectrometry

ISE – Iodide Selective Electrode

ITF – Indonesian Throughflow

NEC – North Equatorial Current

NECC – North Equatorial Countercurrent

NFR – Nuclear Fuel Reprocessing

PDO – Pacific Decadal Oscillation

PO – Pacific Ocean

SCS – South China Sea

SEC – South Equatorial Current

SP – South Pacific

SST – Sea Surface Temperature

1. Introduction

Iodine-129 ($T_{1/2} = 15.7 \text{ Ma}$) is the longest-lived radioisotope of iodine. It is produced naturally through cosmic ray spallation of xenon in the atmosphere and spontaneous fission of uranium in the earth's crust. Natural ^{129}I is well mixed across the environment and has been in steady-state for thousands of years. However, these natural signals have been overshadowed by ^{129}I from human nuclear activities (HNAs) such as nuclear bomb testing, nuclear fuel reprocessing, and nuclear accidents, which introduced massive amounts of ^{129}I into the environment.

The behavior of ^{129}I in the environment is conservative and its biogeochemical cycling is generally known. It is transported mainly through troposphere, stratosphere, and ocean circulations where its residence times are around 2-4 weeks, 3 months to 2 years, and 40,000 years, respectively. Given the long half-life of ^{129}I and the fact that its sources and behavior are generally known, ^{129}I is considered as a promising tracer of HNA-derived radionuclides in the environment and the earth processes (e.g., atmospheric and oceanic circulations) associated with the transport of these radionuclides.

This application is demonstrated and applied in the analysis of ^{129}I in natural archives such as coral, ice, and sediment cores. However, the current number of ^{129}I records in natural archives is sparse. In particular, there are currently only two coral cores (both in the southern hemisphere; Biddulph et al. 2006), one ice core (Alpine region; Reithmeier et al. 2006), and one marine sediment core (Jiaozhou Bay, China; Fan et al. 2016) published as ^{129}I records. Given the small number of published ^{129}I records, a lot remains to be studied to explore the potential of ^{129}I in natural archives.

Nevertheless, these studies give us a glimpse of the possible applications of ^{129}I in natural archives. ^{129}I in these archives can be used (1) as a proxy for HNAs that can

reconstruct the degree of influence of HNAs in locations where archives are taken; (2) as a tracer of atmospheric and oceanic circulations that transported ^{129}I to the locations of the archives, providing pertinent information about the spread and transport of HNA-derived radionuclides; and (3) as a time marker than can be used to establish or confirm the age models of these natural archives.

Given these, the main objective of this dissertation is to construct ^{129}I time series records in natural archives, particularly in two coral cores coming from the northern hemisphere (Philippines), and an ice core coming from Greenland, to explore the full extent of applications of ^{129}I , namely: (1) reconstruction of the effect of HNAs in locations where archives are taken; (2) as tracer of atmospheric and oceanic circulations that transport ^{129}I to these locations; and, (3) as a time marker that can be used to set age models of natural archives.

Specific objectives of this dissertation are the following:

1. First, to develop a method capable of measuring ^{129}I and ^{127}I in about 1-4 g of coral samples – the only published work about $^{129}\text{I}/^{127}\text{I}$ measurement in corals available at the time of this writing was that of Biddulph et al. (2006). This method, however, required 10-30g for analysis. Coral samples that were available for analysis for this dissertation were typically only 1-4 g. Therefore, a method capable of measuring ^{129}I and ^{127}I in smaller amounts of coral samples had to be developed for this study. Furthermore, a smaller coral sample amount requirement is more advantageous because (1) it will make subsampling along coral growth bands simpler and more specific; (2) it enables analyses with higher time resolution; or (3) it frees up other parts of the coral core for other analyses or studies. (Section 3.1.3.1 and Section 4.1.)

2. To construct ^{129}I time series of two coral cores from the Pacific Ocean or PO (east) and South China Sea or SCS (west) sides of the Philippines and compare it to existing southern hemisphere ^{129}I coral records – given that almost all nuclear activities were performed in the northern hemisphere, stronger nuclear bomb test, NFR, and possibly nuclear accident signals are expected in these coral samples. Moreover, comparison of ^{129}I from corals in the PO and SCS sides of the Philippines may differentiate signals from the atmosphere and the ocean. These records can show how HNAs have affected the Philippines given the predominant atmospheric and oceanic processes around the country. (Section 4.2)
3. To construct ^{14}C time series in the same corals from the Philippines to provide comparison with the ^{129}I record, as well as with published records of ^{14}C in other corals – compared to ^{129}I , ^{14}C in corals have been more extensively studied as tracer of ocean circulation and as a time (bomb) marker. Therefore, comparison with ^{14}C will provide context and perspective about the usefulness of ^{129}I in natural archives, in terms of our target applications. (Section 4.3.)
4. To directly compare coral ^{14}C and ^{129}I bomb signals in more detail in terms of their applications in HNA proxy, as time markers, and as ocean mixing tracers through a box mixing model that is capable of simulating ^{14}C and ^{129}I in Baler and Parola. The model is also capable of quantitatively illustrating the mechanisms that explain coral ^{14}C and ^{129}I trends, which were proposed in the previous sections. (Section 3.1.5. and 4.4.)
5. To construct ^{129}I time series of an ice core from Greenland – ice core ^{129}I records show HNA effect over land (and thus, mainly reflect atmospheric signals) and are located in high latitudes, thus complementing our corals records, which on the other hand show HNA signals in marine environments and in low latitudes. ^{129}I in

an ice core from Greenland will demonstrate the extent of applicability of ^{129}I signals and its targeted applications over differences between land/marine, high/low latitudes, and ice/coral archive types. In addition, the Greenland record builds on the existing Alpine ice core ^{129}I record, in that the Greenland has higher temporal resolution (biannual vs. Alpine record's annual/biennial resolution) and it is located at the left of the European reprocessing plants, while the Alpine record is on the right, possibly reflecting atmospheric circulation patterns in the region.

2. Literature Review

2.1. Sources of ^{129}I

Table 1. Sources and inventories of ^{129}I in the environment.

Source	^{129}I inventory (GBq)	Period of release (year)
<i>Natural</i> ¹	1,640 (steady-state ^a)	throughout time
<i>Nuclear bomb tests</i> ^{2,3}	617	1945–1980
<i>Nuclear fuel reprocessing</i> ^{2,4}		
airborne	5,146	1944–2004 ^b
liquid	27,410	1966–2004 ^c
<i>Chernobyl accident</i> ⁵	39	1986
<i>Fukushima accident</i> ⁶	8	2011

References: ¹Hou and Hou, 2012; ²Reithmeier et al., 2006; ³UNSCEAR, 2000; ⁴Reithmeier et al., 2010; ⁵Aldahan et al., 2007; ⁶Hou et al., 2013.

^ai.e., virtually constant across the earth and throughout time.

^bEstimate of total airborne ^{129}I releases from US (Hanford and Savannah River), European (La Hague, Marcoule, and Sellafield) and Former Soviet (Mayak, Seversk, and Zheleznogorsk) nuclear fuel reprocessing facilities until year 2004. However, note that at present, La Hague, Sellafield, and Mayak remain operational.

^cEstimate of total liquid ^{129}I releases from European (La Hague and Sellafield) nuclear fuel reprocessing facilities until year 2004. Note, however, that at present, La Hague and Sellafield remain operational. ^{129}I is directly released by La Hague and Sellafield to the English Channel and Irish Sea, respectively. ^{129}I from these releases are mostly contained in the northern Atlantic and Arctic Oceans (He et al. 2013).

2.1.1. Natural

Iodine-129 is produced naturally in the environment through cosmic ray spallation of xenon in the atmosphere and spontaneous fission of uranium in the earth's crust. Global inventories and fluxes of ^{129}I in steady state estimated by Fabryka-Martin et al. (1985) is shown in Figure 1. One of the largest reservoirs of natural ^{129}I is found in the ocean environment where its residence time is around 40,000 years. Since this residence time is largely longer than the average turnover time of oceans (1000 years), natural ^{129}I becomes well-mixed and relatively constant

across the earth (Moran et al. 1998). Estimate of the natural $^{129}\text{I}/^{127}\text{(stable)I}$ ratio based on shallow marine sediments and archived seaweed is 1.5×10^{-12} (Cooper et al. 1998; Moran et al. 1999). In steady-state, the total estimate of natural ^{129}I inventory is 250 kg or 1,640 GBq (Hou & Hou 2012).

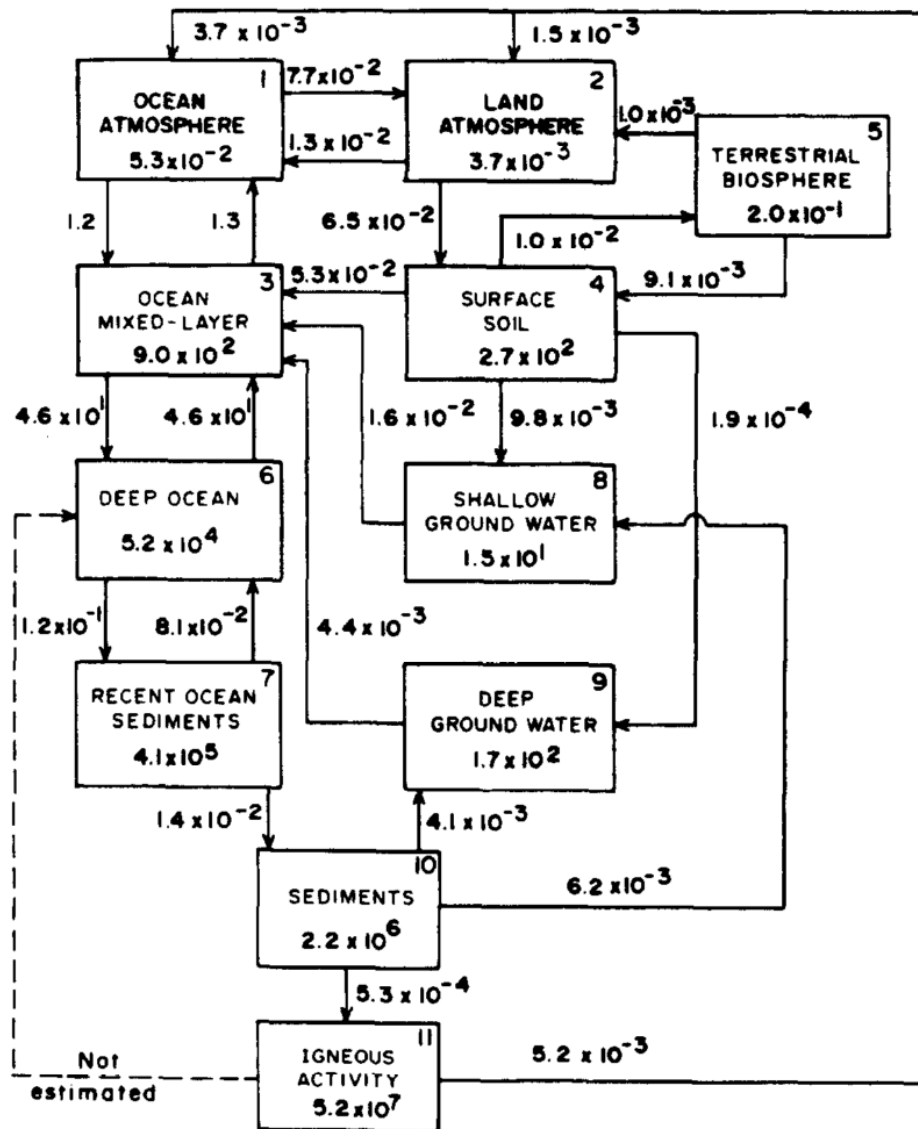


Figure 1. Global inventories and fluxes of natural ^{129}I at steady state. Inventories in grams, fluxes in grams/yr. Based from a predicted $^{129}\text{I}/\text{I}$ ratio for deep ocean of 6.4×10^{-13} . From Fabryka-Martin et al. (1985).

2.1.2. Human nuclear activities

Starting from the mid-1940s to 1950s, natural ^{129}I signals have been overshadowed by the introduction of ^{129}I from human nuclear activities (HNAs). I classified these into three types: nuclear weapons testing, nuclear fuel reprocessing, and nuclear accidents.

2.1.2.1. Nuclear weapons testing

Nuclear bomb tests aboveground were performed between 1945-1980 (Figure 2). In terms of bomb fission yield, 90% of all tests were performed in 1951-1962 primarily by the United States and Soviet Union and most notably in the year 1962. Succeeding tests from 1964 onwards were performed by China and France. Corresponding bomb test sites of different countries are shown in Figure 3.

Based on the stabilization height of the cloud formation of the bomb explosions, radionuclides released by the tests (including ^{129}I) can be apportioned to those injected locally and regionally, into the troposphere, and into the stratosphere (Figure 4; UNSCEAR 2000). Movement and seasonal residence times (determined from empirical fitting to ^{90}Sr fallout measurements) of bomb-derived radionuclides are illustrated in Figure 5. About 24% of radionuclides were injected to the local, regional, and troposphere regions and were transported by prevailing tropospheric wind patterns and are deposited back to the earth's surface in 2-4 weeks. About 76% of radionuclides derived from these bomb tests were injected into the stratosphere and were scattered widely across the world through stratospheric circulation (Figure 6). Radionuclides injected to the stratosphere take 3 months to 2 years to be deposited back to the earth's surface. Consequently, strong signals of some radionuclides related

to the bomb tests (e.g., ^{90}Sr) were measured in the northern hemisphere but were weak in the southern hemisphere (Figure 7). This is because most test sites were located in the northern hemisphere (Figure 3) and the radionuclides' atmospheric residence times were shorter than the equatorial exchange time of 2 years (Figure 5). Moreover, stronger signals are observed in mid-latitudes (e.g., 50°N) because of stronger stratosphere-troposphere exchange in these regions (Figure 6).

2.1.2.2. Nuclear fuel reprocessing

^{129}I is released as I_2 gas in the first stages of the nuclear fuel reprocessing (NFR) process when used nuclear fuel are dissolved in HNO_3 (Figure 8). Most notable facilities in terms of airborne ^{129}I emissions are Hanford and Savanna River in the United States; La Hague, Marcoule, and Sellafield in Europe; and Mayak, Seversk, and Zheleznogorsk in the former Soviet (Figure 9). In the present, NFR is done to reprocess used uranium fuel into mixed-oxide fuel for reuse in commercial nuclear power plants. In the past, however, the NFR process was used to produce weapons-grade nuclear material for the manufacture of nuclear bombs. Thus, with the exception of Sellafield and La Hague, little is known about the ^{129}I emissions of NFR facilities often because of the military nature of their operations. Consequently, most airborne NFR ^{129}I emissions had to be estimated from the amount of plutonium produced in these facilities (Reithmeier et al. 2006; Reithmeier et al. 2010). Both measured and estimated airborne ^{129}I releases from NFRs are shown in Figure 10. Airborne ^{129}I released by NFRs are mainly transported by prevailing tropospheric winds (Figure 9). Estimated transport and distribution of ^{129}I from NFRs are showed in Figure 11, based from an atmospheric deposition model by Reithmeier et al. (2010).

In recent times, improved reprocessing technologies, capture airborne ^{129}I and release it as liquid discharges instead. Such is the case for Sellafield and La Hague wherein liquid discharges are currently more than airborne emissions (Figure 12). This increasing amount of liquid discharges from Sellafield and La Hague NFRs also cause more and more ^{129}I in the northern Atlantic and Arctic Oceans to be re-emitted back to the atmosphere (Hou et al. 2009). Re-emitted ^{129}I is estimated to be about 10 GBq/yr from 1996-2004 (Figure 10d; Reithmeier et al. 2006).

NFR is the biggest contributor of ^{129}I to the environment, releasing estimated totals of 5146 GBq and 27,410 GBq of airborne and liquid releases, respectively.

2.1.2.3. Nuclear accidents

Nuclear accidents such as the Chernobyl and the Fukushima disaster also contribute to the total ^{129}I inventory in the environment. Chernobyl released about 39 GBq of airborne ^{129}I in 1986 while Fukushima released 8 GBq of both airborne and liquid ^{129}I discharge in 2011 (Aldahan et al. 2007; Hou et al. 2013). Total ^{129}I contributions of nuclear accidents may appear insignificant compared to nuclear bomb tests (617 GBq) and NFR (5146 GBq), but ^{129}I from accidents were almost single-event releases while bomb tests and NFR were released across several years. In an annual timescale, ^{129}I from nuclear accidents make a significant contribution (Figure 10d).

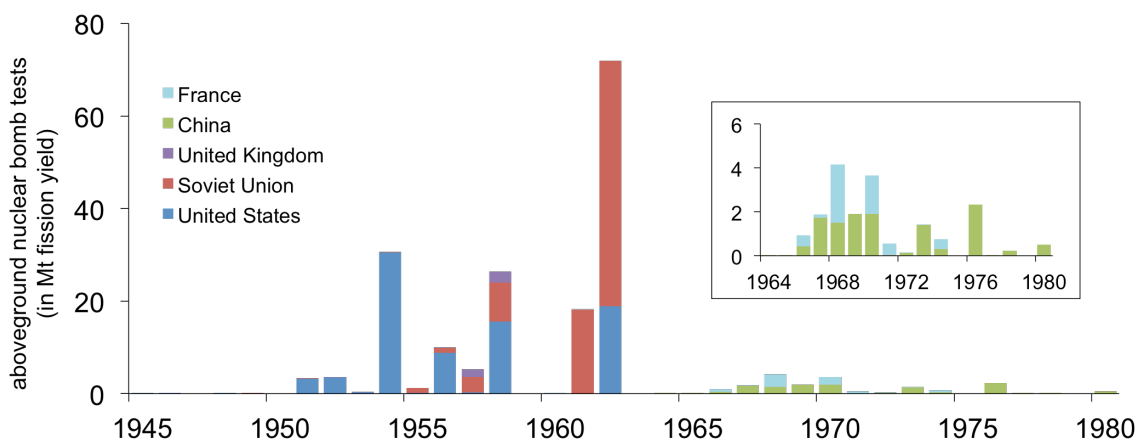


Figure 2. Aboveground nuclear bomb testing in megaton (Mt) fission yield.
Data from UNSCEAR (2000).



Figure 3. Locations of nuclear bomb test sites per country.
Soviet Union (red), United States (blue), China (green), United Kingdom (purple),
and France (aqua). From (UNSCEAR 2000).

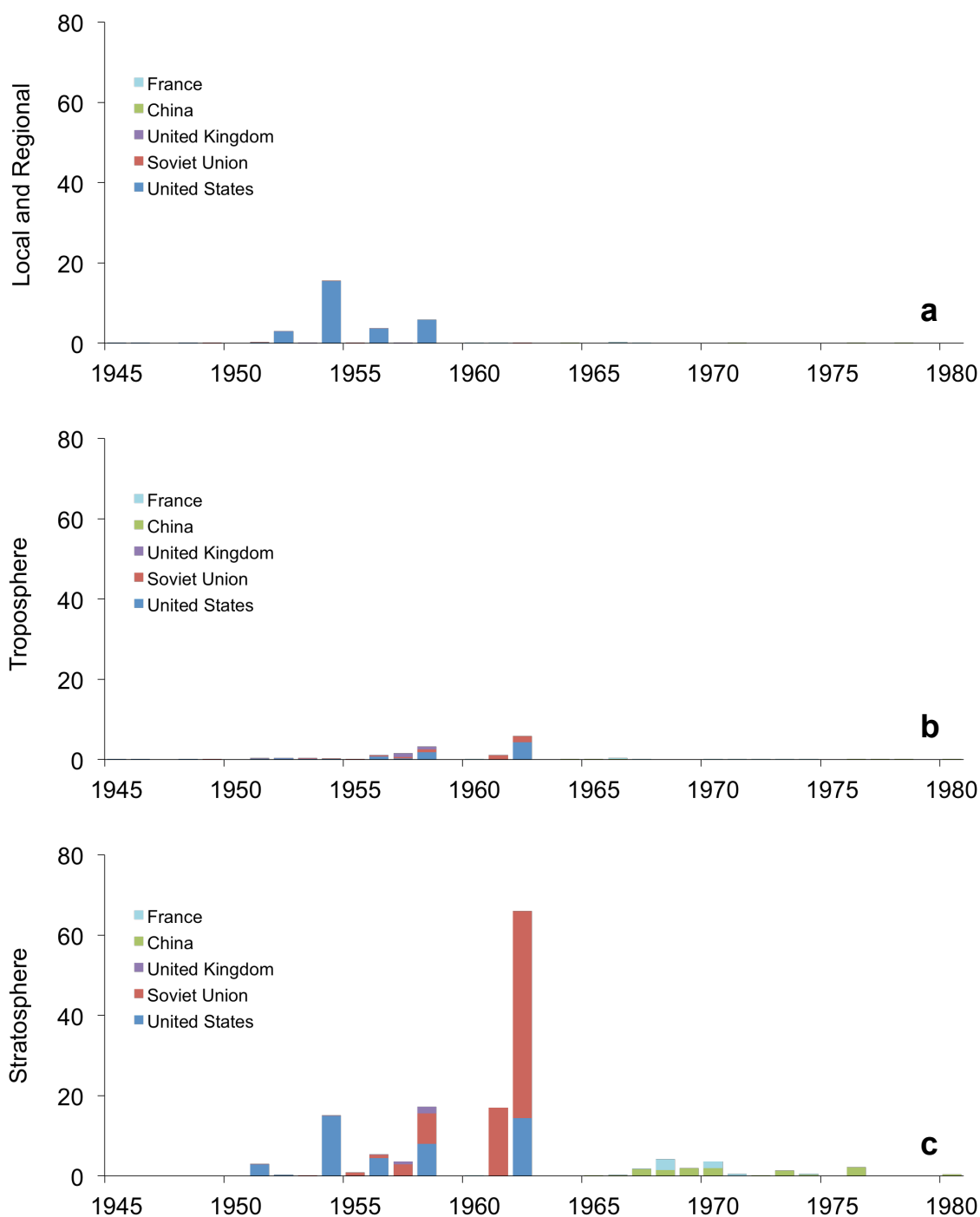


Figure 4. Portion of radionuclides (in Mt fission yield) injected to (a) local and regional, (b) troposphere, and (c) stratosphere by nuclear bomb tests.
Data from UNSCEAR (2000).

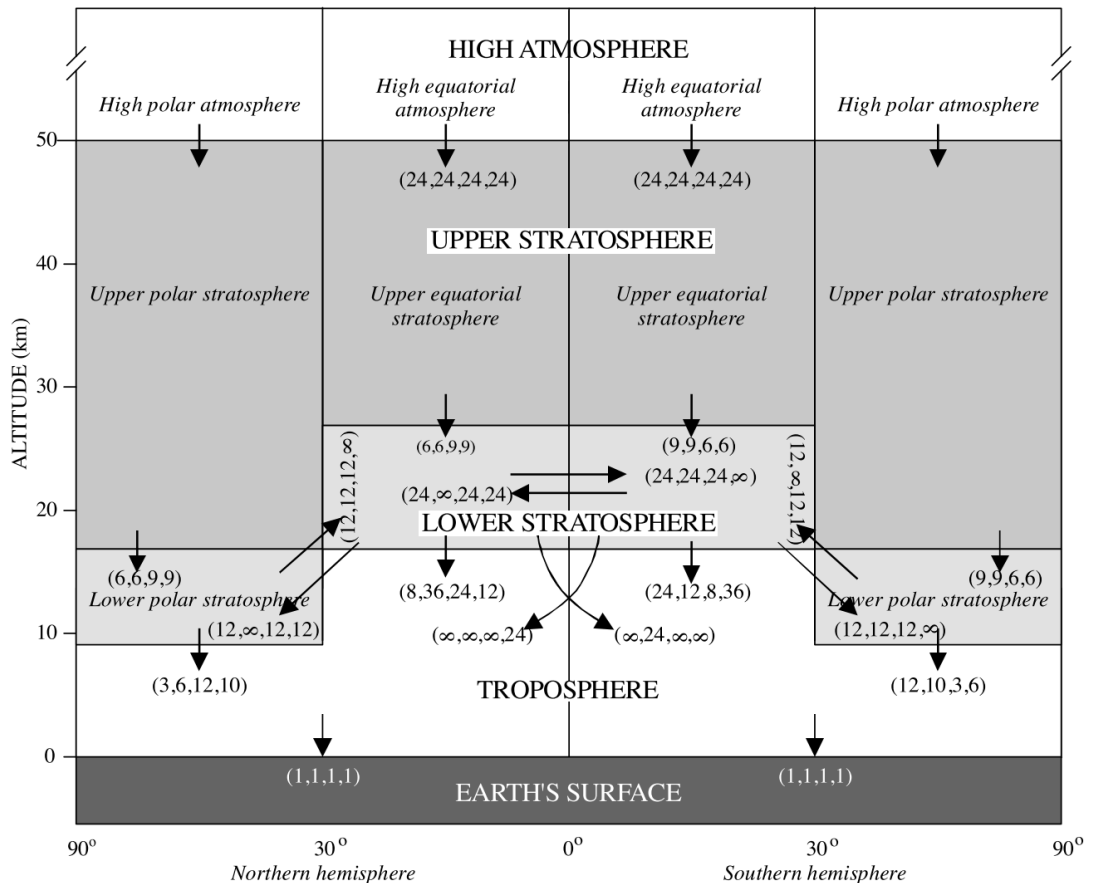


Figure 5. Schematic diagram of transfers between atmospheric regions and the earth's surface of bomb-derived radionuclides.

Numbers in parentheses are removal half-times (in months) for the following months of each year: March-May, June-August, September-November, December-February. A value of ∞ means there is no transfer during those particular months. Values were determined empirically from measurements of fallout radionuclides such as ⁹⁰Sr.

From UNSCEAR (2000).

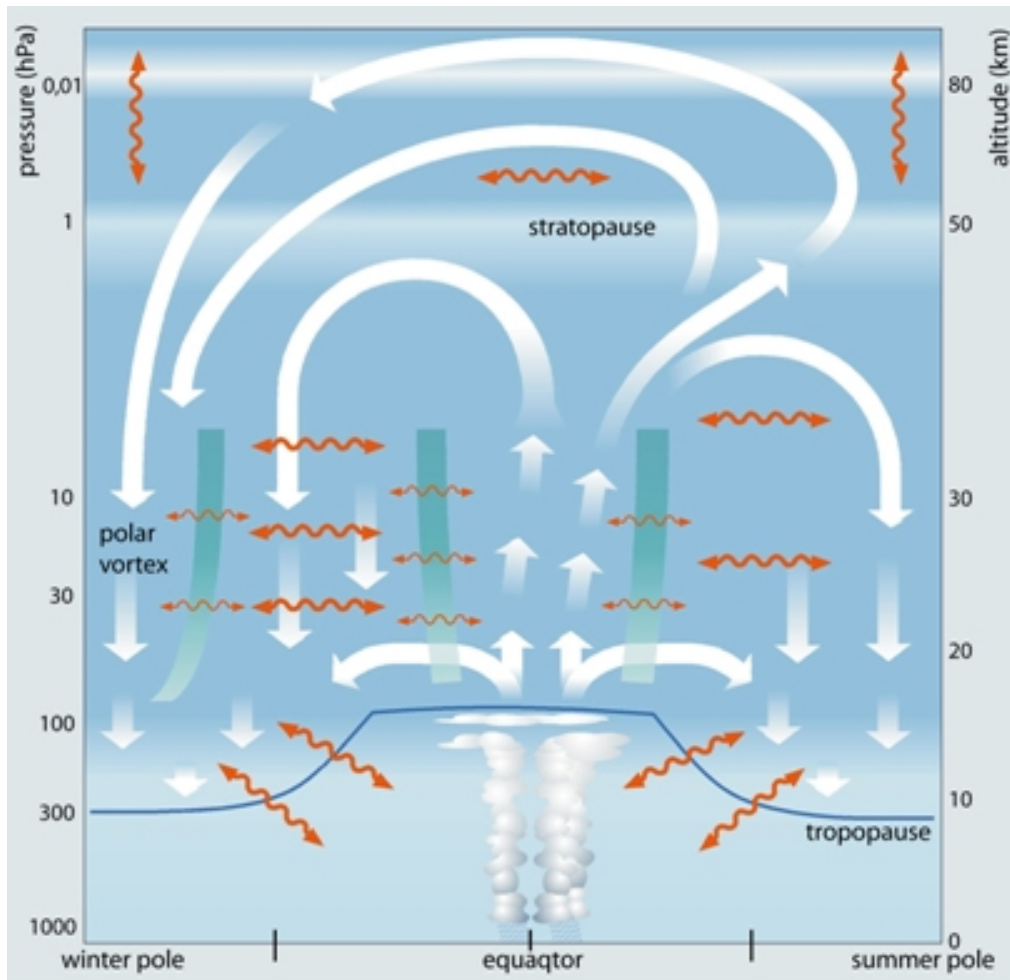


Figure 6. General circulation of the stratosphere.

From <http://weatheradvance.com/>.

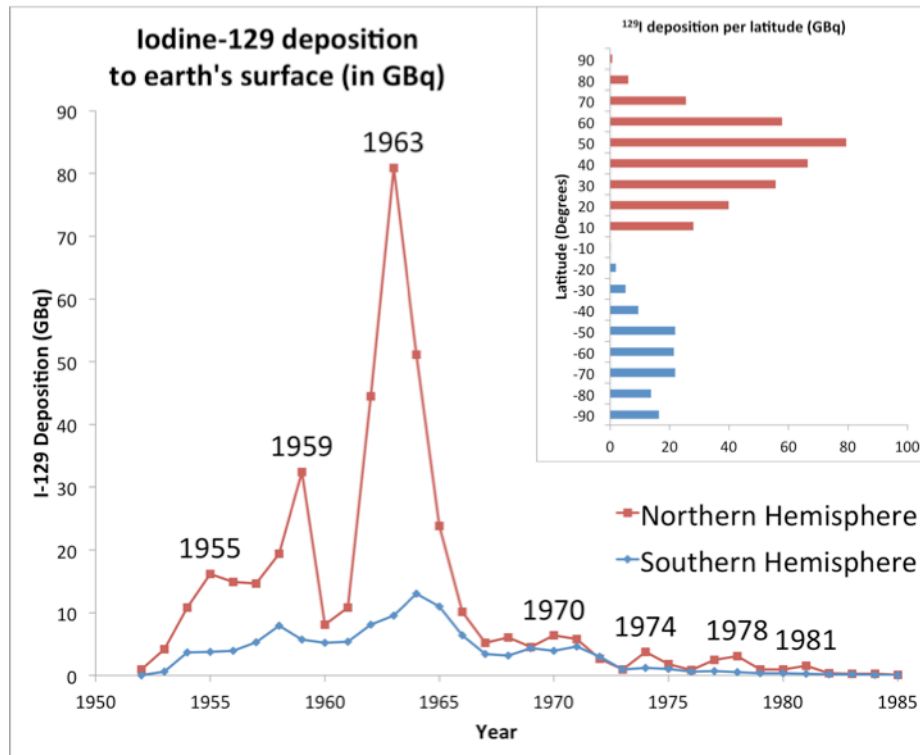


Figure 7. Average deposition of bomb-derived ^{90}Sr in the northern and southern hemisphere, and per 10° latitude band (inset).
Data from UNSCEAR (2000).

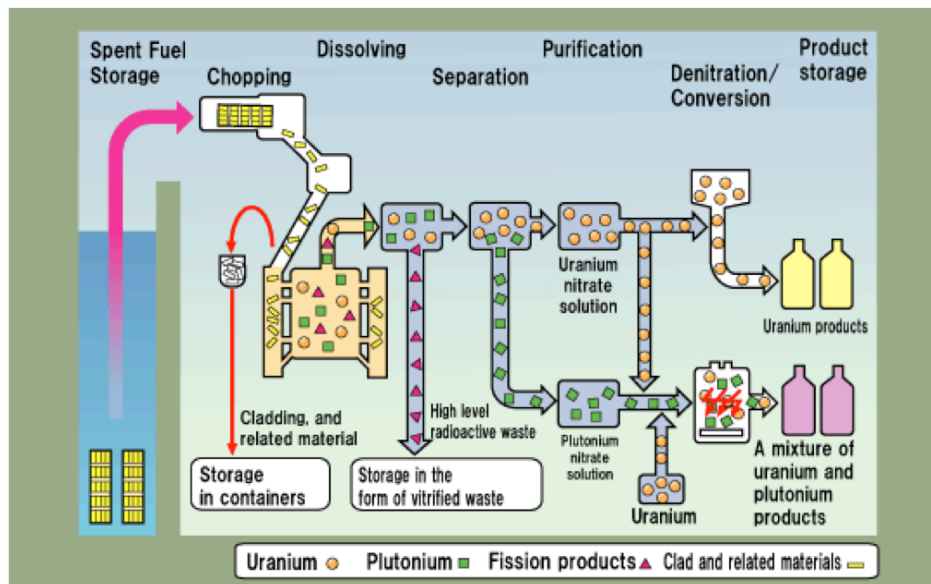


Figure 8. General process of nuclear fuel reprocessing.
From <https://www.jaea.go.jp/>.

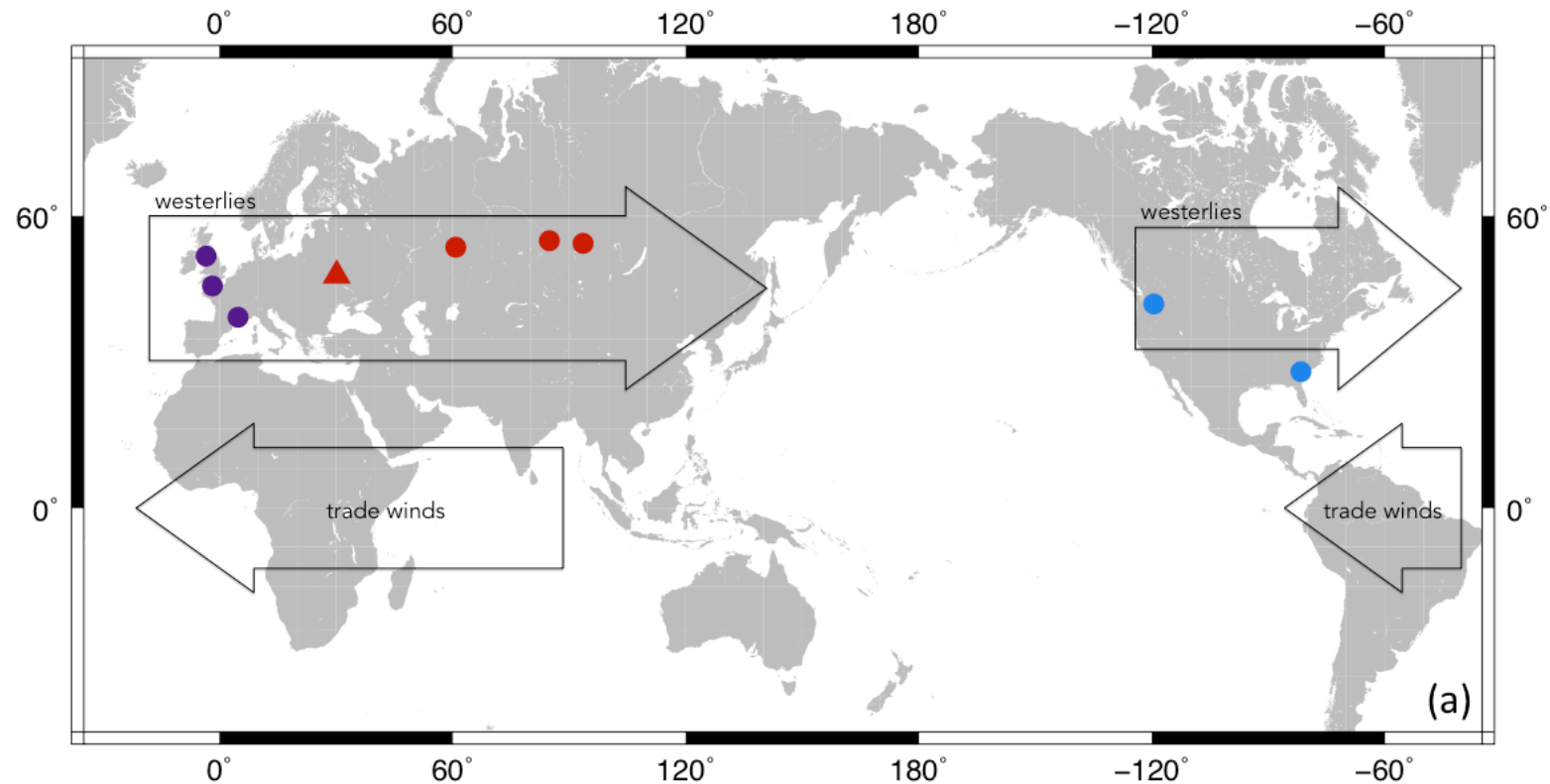


Figure 9. Locations of notable NFR facilities and the Chernobyl Accident.

NFR facilities (circles) from L-R: Europe (purple – Sellafield, La Hague, Marcoule), Former Soviet (red – Mayak, Seversk, Zheleznogorsk), United States (blue – Hanford, Savannah River); also shown is the location of the Chernobyl Accident (red triangle). Also shown are the prevailing tropospheric wind patterns (block arrows). This map was produced using the Generic Mapping Tools (Wessel & Smith 2013).

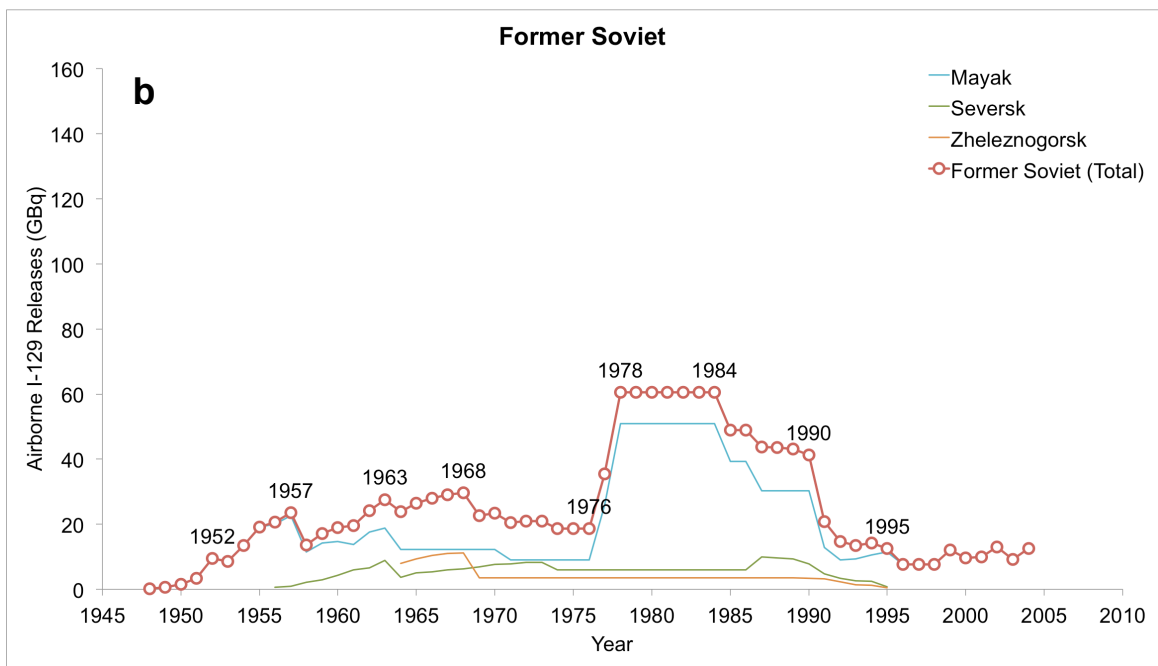
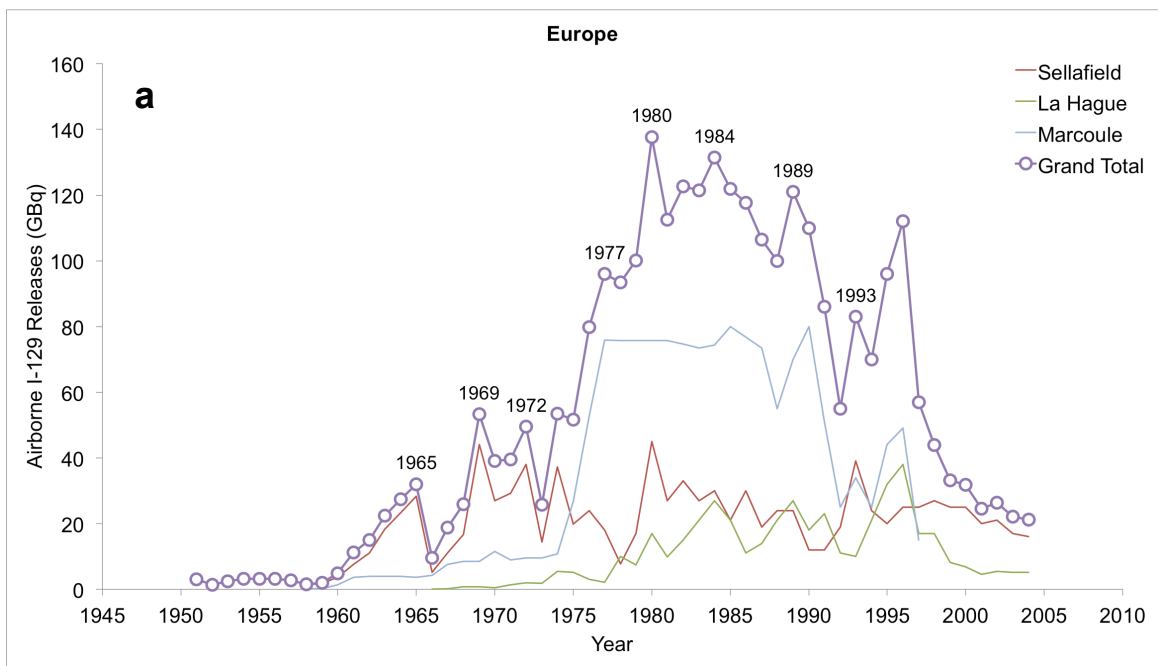


Figure 10. Airborne ^{129}I emissions of notable NFR facilities.

^{129}I emissions (in GBq) of NFR facilities in (a) Europe, (b) Former Soviet, (c) United States, and (d) their total. Data from: (Reithmeier et al. 2010; Reithmeier et al. 2006); Also shown are the contribution of the Chernobyl Accident (39 GBq; Aldahan et al. 2007) and ^{129}I re-emitted from the ocean (about 10 GBq/yr; Reithmeier et al. 2006) added to the total of NFR emissions in (d).

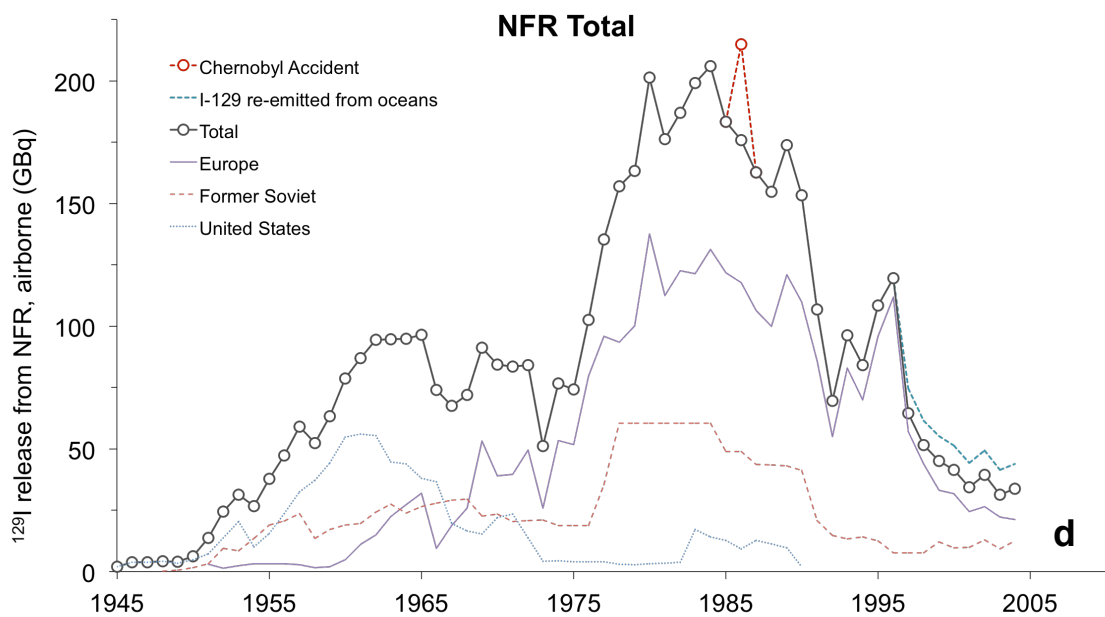
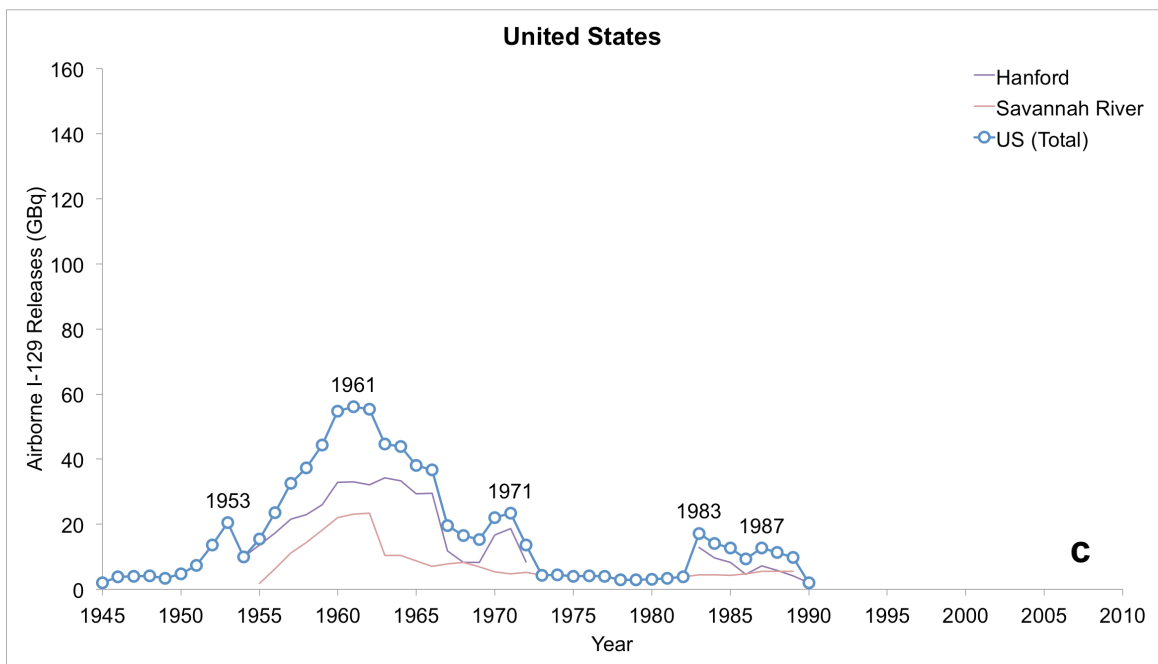


Figure 10 (continued). Airborne ^{129}I emissions of notable NFR facilities. ^{129}I emissions (in GBq) of NFR facilities in (a) Europe, (b) Former Soviet, (c) United States, and (d) their total. Data from: (Reithmeier et al. 2010; Reithmeier et al. 2006); Also shown are the contribution of the Chernobyl Accident (39 GBq; Aldahan et al. 2007) and ^{129}I re-emitted from the ocean (about 10 GBq/yr; Reithmeier et al. 2006) added to the total of NFR emissions in (d).

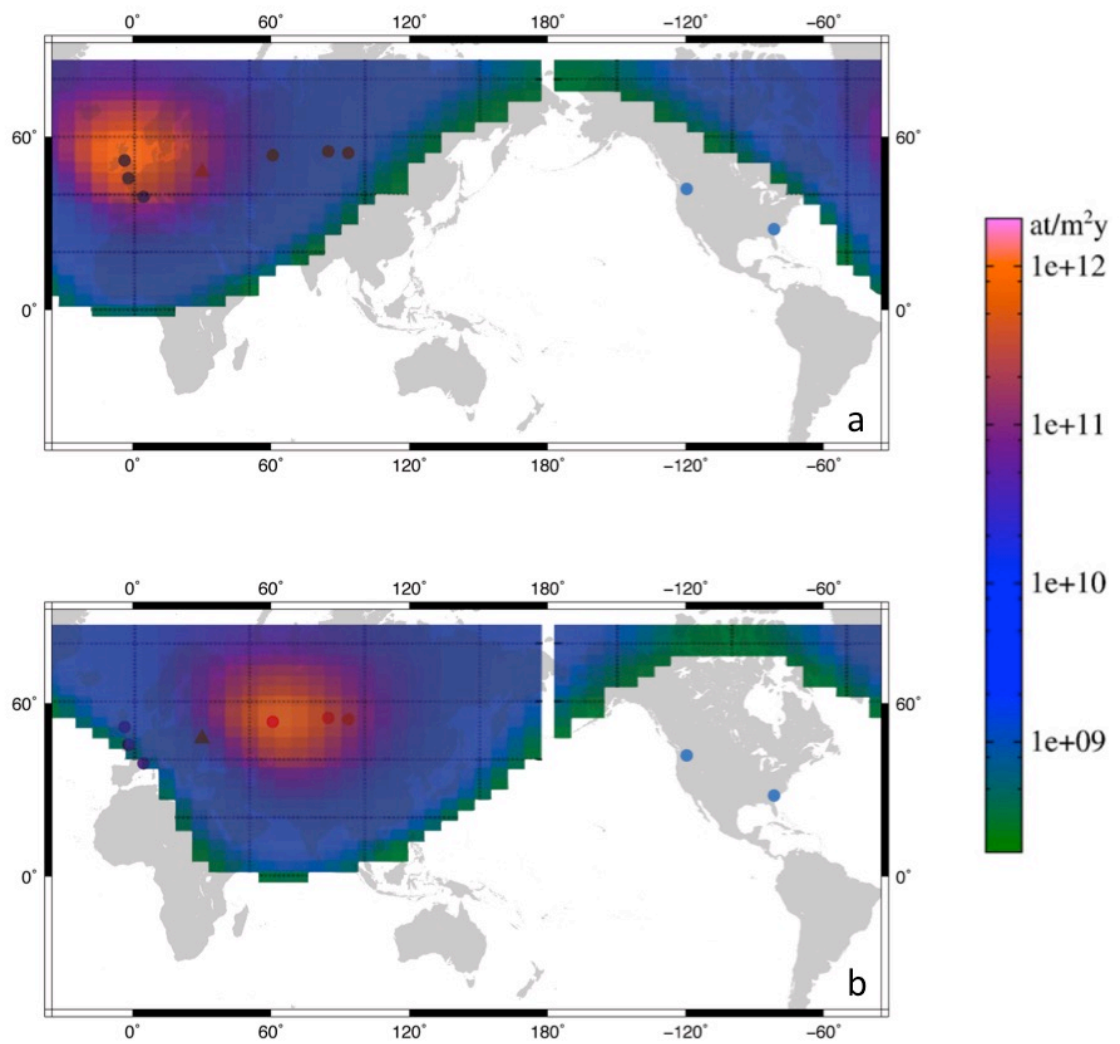


Figure 11. Atmospheric deposition modeling of airborne ^{129}I from (a) Sellafield and (b) Mayak NFRs in year 2004.
 Depositions are in $\text{atoms}/\text{m}^2\text{y}$. Adapted from Reithmeier et al. (2010).

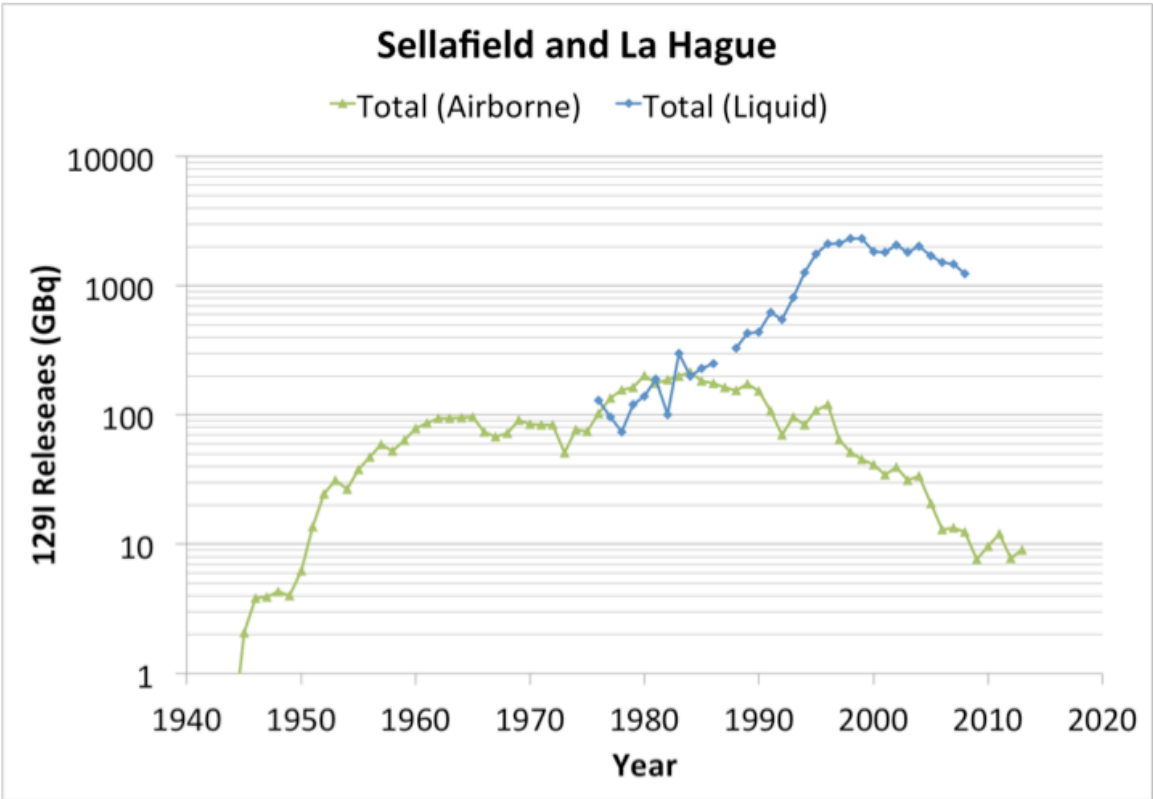


Figure 12. Comparison of airborne and liquid ¹²⁹I releases of La Hague and Sellafield.

Data from: (Reithmeier et al. 2010; Reithmeier et al. 2006; UNSCEAR 2000).

2.1.2.4. Known effects of HNA to the Philippines

Aside from actual ^{90}Sr deposition measurements and the subsequent modeling and estimation of other radionuclides from these ^{90}Sr measurements (UNSCEAR 2000; see section 2.1.2.1), little is otherwise known about the effects of HNAs on certain areas. For example, I look at the Philippines and Greenland cases (which are the study sites for coral and ice core analyses, respectively).

In the Philippines, atmospheric radioactivity monitoring started in February 2001 as a part of the international monitoring system of the Comprehensive Nuclear-Test-Ban Treaty Organization (CTBTO 2001). This system was able to detect the atmospheric signal of the Fukushima Accident in 2011 (Long et al. 2012). Regular measurements of ^{137}Cs , $^{239+240}\text{Pu}$, and a few other radionuclides in seawater and biota around the country are also being carried out since 1975 through the Asia-Pacific Marine Radioactivity Database (ASPAMARD) project of the International Atomic Energy Agency (IAEA) and United Nations Development Programme (UNDP; Duran et al. 2004). ^{137}Cs in marine sediments around the country have also been done, although the relatively quick half-life of ^{137}Cs (30.17 years) and the fact that there are no significant inputs in recent times, resulted in very low ^{137}Cs concentrations in sediments that were often undetectable with current analytical instruments (Yii et al. 2007; Duran et al. 2004). Therefore, to the best of my knowledge, little or no information is available about the effects of nuclear bomb testing, NFR, and the Chernobyl Accident to the Philippines aside from those presented in this study.

2.2. ^{129}I in the environment

Behavior of ^{129}I in the environment is conservative and its biogeochemical cycling is generally known. The general iodine cycle in the environment is shown in

Figure 13. Iodine is present in oceans mainly in the form of I^- and IO_3^- . Marine iodine can either go to marine sediments, where it eventually stays in the order of 10^6 to 10^8 years until released through brine, hydrothermal water, or volcanic activity (Fabryka-Martin et al. 1985; Muramatsu et al. 2004); or released to the atmosphere as CH_3I through biological activity. Iodine species in the atmosphere react with sunlight and are converted to I_2 or HIO . These are brought back to the earth's surface primarily through wet deposition (as I^- and IO_3^- dissolved in precipitation), or partly through dry deposition (Reithmeier et al. 2010).

Looking at the iodine cycle, prevalent transport mechanisms of ^{129}I are through troposphere, stratosphere, and ocean circulations (Figure 9, Figure 6, Figure 14) where the residence times of ^{129}I are around 2-4 weeks, 3 months to 2 years, and 40,000 years, respectively (Fabryka-Martin et al. 1985; Moran et al. 1999; UNSCEAR 2000). Given the long half-life of ^{129}I and that its sources and behavior of ^{129}I are generally known, ^{129}I has found wide applications as an environmental tracer of HNA-derived radionuclides and earth processes (e.g., atmospheric and oceanic circulations) associated with their transport.

As far as I know, there are few other HNA-derived radionuclides with known sources, with a long enough half-life and atmospheric/oceanic residence times, and is present in sufficiently detectable concentrations to be used as an environmental tracer. 3H , ^{90}Sr , and ^{137}Cs are among the frequently used tracer radionuclides but these are limited with their relatively short half-lives (12.3, 28.8, 30.2 years, respectively), which means they will have low concentrations and will be difficult to detect after a certain number of years from its release. They are also emitted by nuclear bomb testing and nuclear accidents but not NFR. NFR provides an additional source, which gives ^{129}I an advantage over other radionuclides in terms of applicability as an

environmental tracer. ^{236}U is another emerging oceanographic tracer radionuclide that is released by nuclear bomb testing, NFR, and nuclear accidents. In the present, however, less is known and studied about ^{236}U than ^{129}I (Winkler et al. 2012; Casacuberta et al. 2014; Christl et al. 2015). ^{14}C is probably the most studied and widely used radionuclide as environmental tracer and it is discussed entirely in a separate section (see section 2.4).

To illustrate the application of ^{129}I as an environmental tracer, He et al. (2013) show how liquid ^{129}I released by Sellafield and La Hague in the northern Atlantic and Arctic Oceans can be used to trace the circulations and water mass transport of these bodies of waters (Figure 15). Numerous studies about the Fukushima accident also used ^{129}I to reconstruct the accident's effects as well as to trace movement of accident-derived radionuclides across the atmospheric, seawater, and soil environment (Long et al. 2012; Hou et al. 2013; Stan-Sion et al. 2015; Honda et al. 2015; Miyake et al. 2012). Furthermore still, a review by Hou & Hou (2012) show applications of ^{129}I in geological dating in the scale of 2-80 Ma, and in the identification of sources of carbon hydrates by analysis of pore, brine, and ground waters. Yet another particular environmental application, which remains scarcely explored yet shows good potential in the study of radionuclide spread and associated earth processes, is the analysis of ^{129}I in natural archives such as coral, ice, and sediment cores.

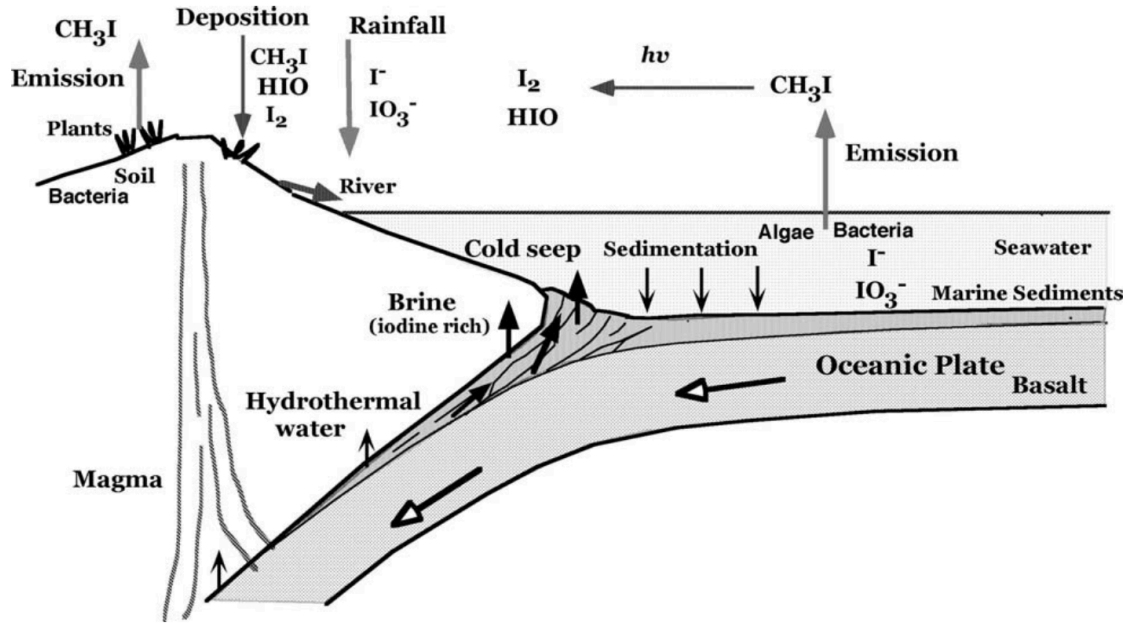


Figure 13. The global iodine cycle.
From Muramatsu et al. (2004).

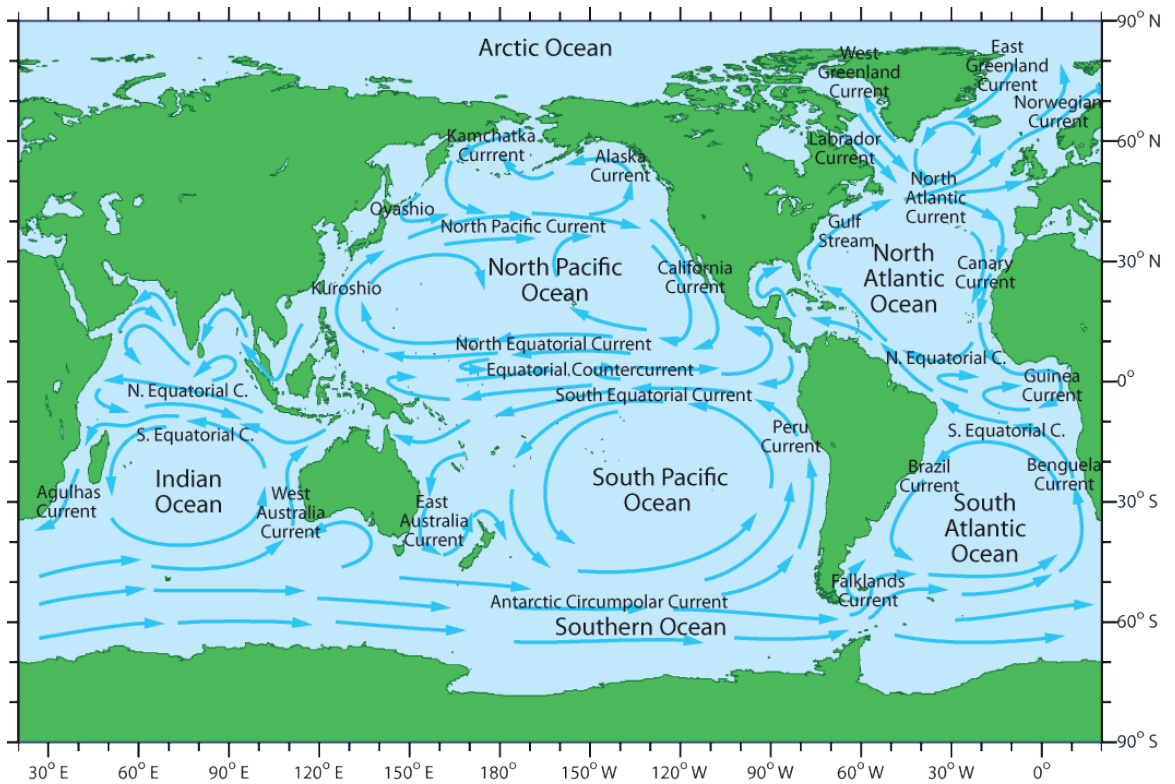


Figure 14. Global ocean circulation.
From <http://www.seos-project.eu/>.

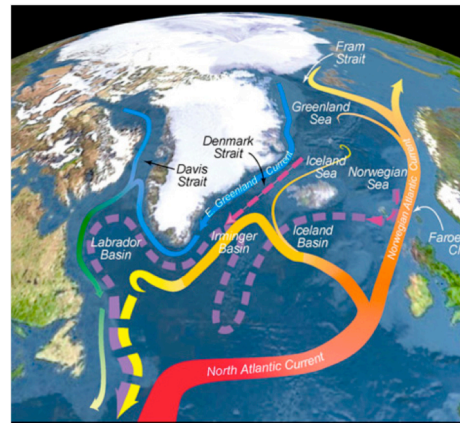
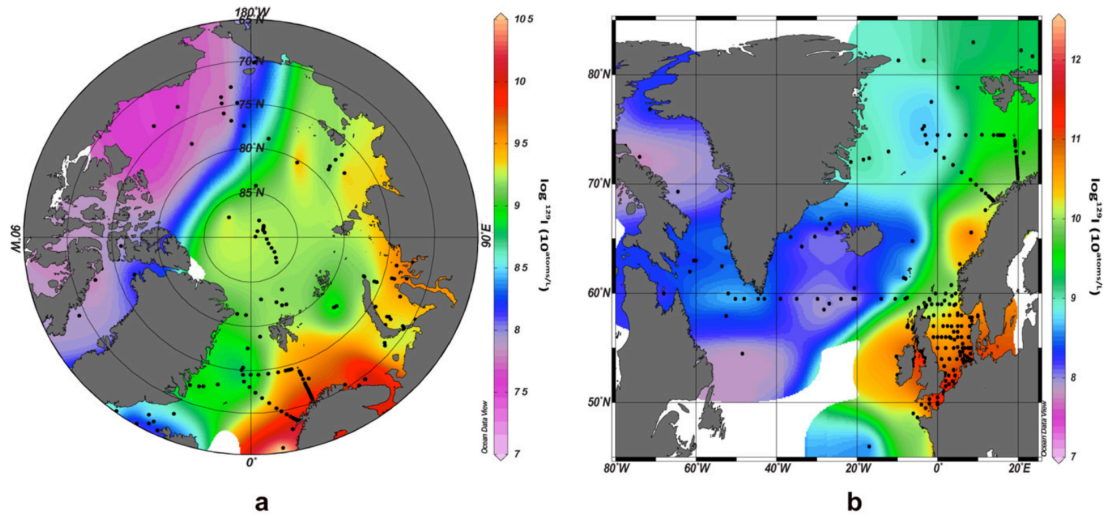


Figure 15. ^{129}I as tracer of Arctic and North Atlantic Ocean circulations. ^{129}I concentrations (top; from He et al. 2013) as tracer of (a) Arctic and (b) North Atlantic Ocean circulations. Figures showing circulation taken from nsidc.org and www.who.edu, respectively.

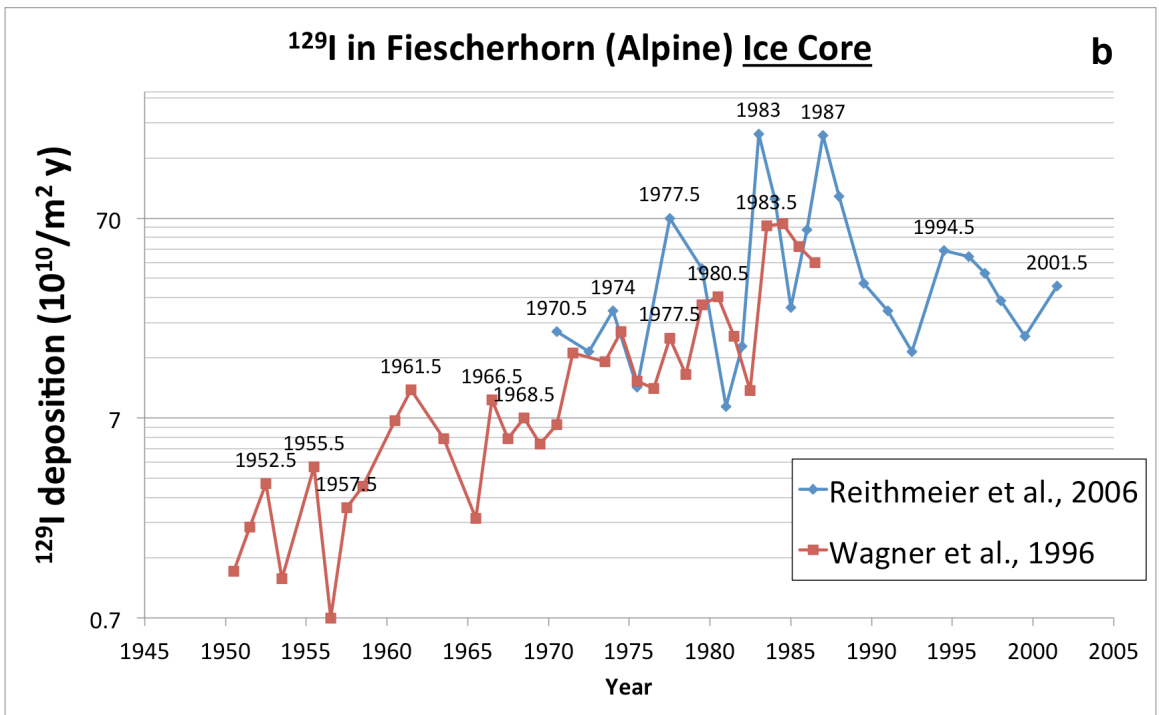
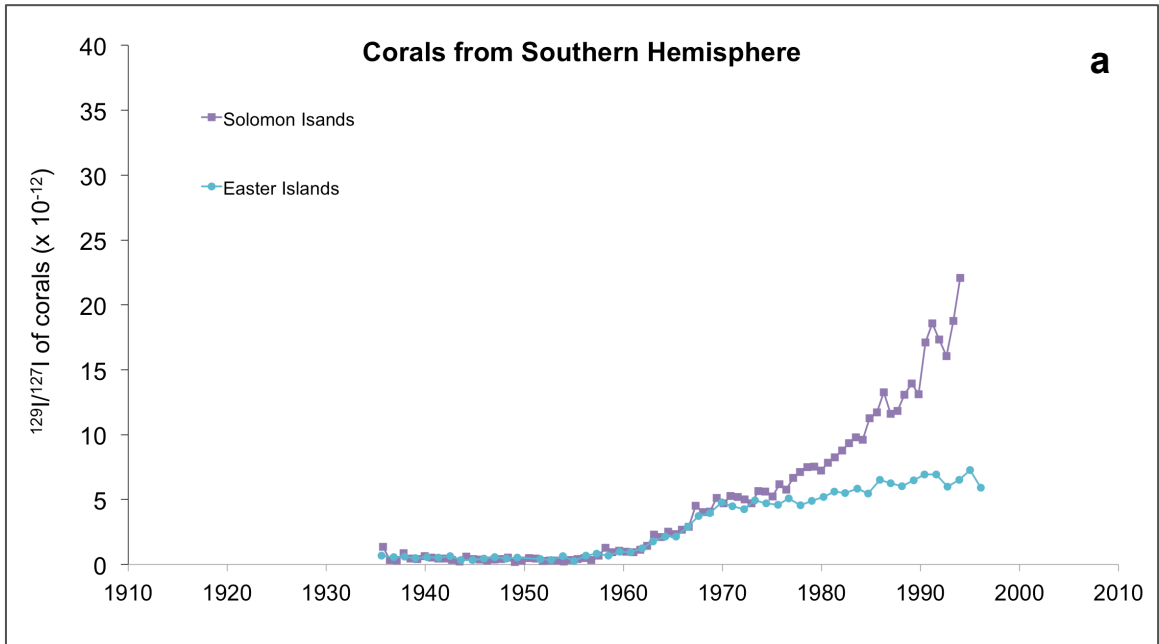


Figure 16. ^{129}I in (a) coral, (b) ice, and (c) sediment archives.

Data sources: coral – (Biddulph et al. 2006); ice – (Reithmeier et al. 2006; Wagner et al. 1996); sediment – (Fan et al. 2016). Locations of archives are shown in Figure 20.

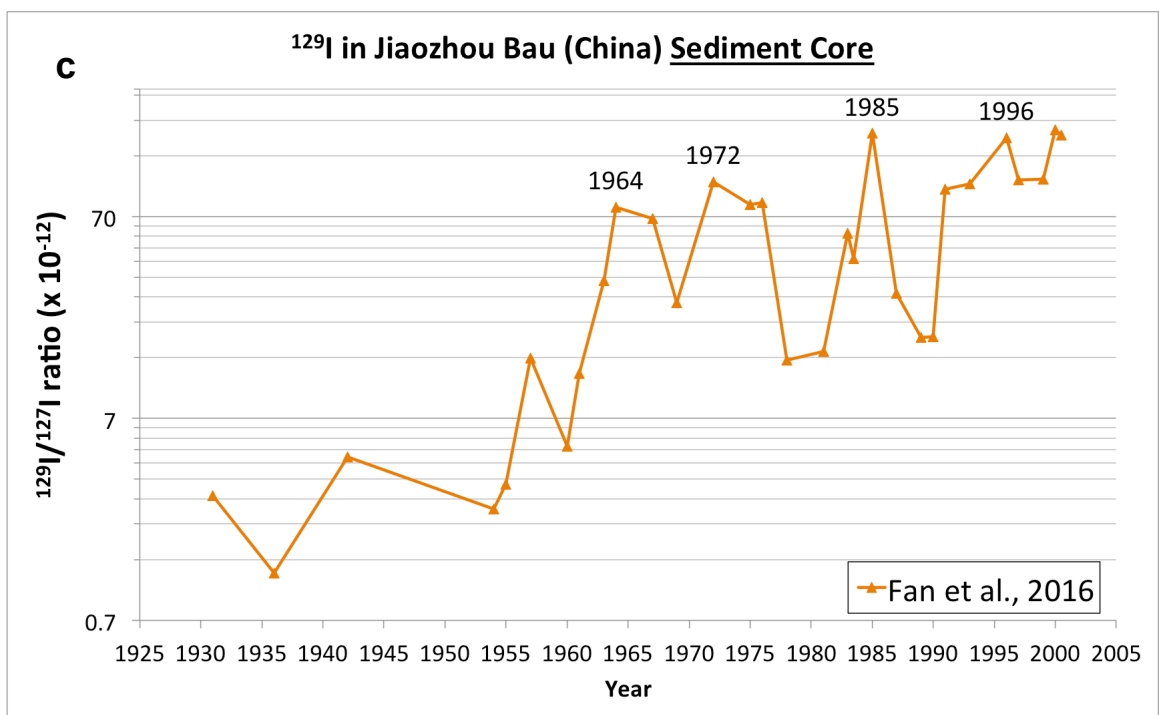


Figure 16 (continued). ^{129}I in (a) coral, (b) ice, and (c) sediment archives.
 Data sources: coral – (Biddulph et al. 2006); ice – (Reithmeier et al. 2006; Wagner et al. 1996); sediment – (Fan et al. 2016). Locations of archives are shown in Figure 20.

2.3. ^{129}I in natural archives

^{129}I time series constructed from corals from the Solomon and Easter Islands in the southern hemisphere show relatively equal natural ratios of $^{129}\text{I}/^{127}\text{I}$ until mid-1950s, where increases associated with nuclear bomb tests and NFR were subsequently observed (Figure 16; Biddulph et al. 2006). Nuclear bomb test signals (mid-1950s to 1970) showed equal rates of increase in both corals, and the authors interpreted this as the ^{129}I signal coming mainly from the atmosphere. NFR signals (1970 onwards), on the other hand, showed steeper increase in the Solomon Island coral because it was located along the South Equatorial Current, which presumably carried the NFR ^{129}I signal. In contrast, the Easter Island coral had a relatively muted response because it was located in the middle of the South Pacific Gyre (Figure 14). Corals as archives for ^{129}I take advantage of the fact that iodine is biophilic and thus tends to be relatively concentrated in organic material such as coral skeletons. Biddulph et al. (2006) reports that iodine concentration in corals are about 100x that of seawater. Therefore, it should be easier to analytically measure ^{129}I in corals, which is normally in trace levels in the environment.

^{129}I records from an Alpine ice core (Reithmeier et al. 2006) and a sediment core from Jiaozhou Bay, China (Fan et al. 2016) show more detailed features compared to the southern hemisphere coral records primarily because these archives were taken from the northern hemisphere where most of the HNAs were performed (Figure 16). In particular, the Alpine ice core show specific peaks associated with nuclear bomb tests (1950-1970). It also shows corresponding signals for NFR (1970 onwards). However, the authors were not able to explain specific peaks observed around 1980-1990 and they attributed this to age model uncertainties or the movement of ^{129}I across the ice column due to melting/refreezing of the ice. Sediment core from

Jiaozhou Bay, China show peaks associated with nuclear bomb testing in 1957, 1964, and around 1972-1976, with the latest being associated specifically to Chinese tests. It also recorded a peak around 1985-1987, which the authors associate with the Chernobyl accident. A surprisingly consistent high ^{129}I profile in 1990 onwards was contrary to the decreasing airborne ^{129}I from NFRs during this time (see section 2.1.2.2). This trend was thus interpreted to be a reflection of ^{129}I liquid discharges by European NFRs in the Atlantic and Arctic Ocean, being re-emitted to the atmosphere and transported to the Chinese region.

These studies demonstrate the application of ^{129}I in natural archives for the reconstruction of effect of HNAs in locations where archives are taken and in the study of atmospheric and oceanic circulations that transported ^{129}I to these locations.

2.4. ^{14}C in corals

Carbon-14 or ^{14}C is among the three naturally occurring isotopes of carbon and the only one that is radioactive ($T_{1/2} = 5730 \pm 40$ years). It is naturally produced in the upper troposphere and stratosphere through $^{14}\text{N}(\text{n,p})^{14}\text{C}$ reaction between thermal neutrons produced by cosmic rays, and nitrogen in the atmosphere. Natural ^{14}C exists in trace amounts in the environment. However, massive amounts of man-made or anthropogenic ^{14}C were introduced during the peak of aboveground nuclear weapons testing in mid-1950s to early-1960s. Figure 17 shows atmospheric ^{14}C influence from nuclear weapons testing. There is about 2-year delay between northern and southern hemisphere, which is probably caused by the restricted atmospheric exchange between the northern and southern hemispheres estimated to be also about 2 years (UNSCEAR 2000; Peng et al. 1998). With continued exchange and no additional

input, ^{14}C values then eventually equalize between the northern and southern hemisphere in the later years.

Similar to other isotopes of carbon, ^{14}C mainly exists in the atmosphere in the form of gaseous CO_2 . A small portion of the atmospheric CO_2 inventory is removed from the atmosphere through weathering by silicate rocks, but practically all atmospheric CO_2 is continuously exchanged between atmosphere, terrestrial plants, and ocean environments (Figure 18): CO_2 taken up by plants are converted to biomass through photosynthesis. Majority of this, however, are released back to the atmosphere through plant, soil, and animal respiration; CO_2 dissolved into the ocean surface react with water to form H_2CO_3 and its deprotonated species, HCO_3^- and CO_3^{2-} ions. All these species, together with dissolved CO_2 , are collectively known as dissolved inorganic carbon or DIC. However, this reaction is highly reversible and CO_2 may be reformed and released back to the atmosphere as easily as it was dissolved. This continuous exchange of CO_2 between atmosphere, plants, and the ocean results in long atmospheric CO_2 (and thus, ^{14}C) lifetimes. The Intergovernmental Panel on Climate Change (IPCC) and the Bern Carbon Cycle Model estimate that 50% of a pulse of CO_2 injected to the atmosphere will be removed within 30 years, a further 30% will be removed within a few centuries, and the remaining 20% may remain in the atmosphere for thousands of years (Denman et al. 2007; Joos et al. 2001). Nonetheless, portion of DIC may be transported to deeper parts of the ocean and eventually fixated to marine sediments by vertical movement of water mass and by take up of biota (e.g., phytoplankton) that sink to deep waters upon death.

DIC may also be incorporated in CaCO_3 shells or skeletons of calcifying marine organisms such as corals. Because of this, coral skeletons record ^{14}C concentrations of

surface seawater during the time of their formation, and thus are capable of storing information about variations of marine ^{14}C concentration across time. Consequently, ^{14}C in corals found wide applications as a tracer of ocean mass circulation and as a time marker, used to confirm or establish coral age dates or chronologies. Several published records of ^{14}C in corals and their corresponding locations are shown in Figure 19.

^{14}C in corals have been used to study ocean mass circulation, specifically vertical mixing and horizontal advection. ^{14}C concentrations are high in the surface ocean because ^{14}C primarily comes from the atmosphere where it is produced. Conversely, ^{14}C concentrations are relatively low in deep ocean waters. Therefore, vertical mixing processes such as upwelling or downwelling can decrease the amount of ^{14}C in the ocean surface by either introducing low ^{14}C deep waters to the surface or by transporting ^{14}C rich waters down to deeper ocean, respectively. ^{14}C in corals from eastern equatorial (Galapagos; Guilderson & Schrag 1998) and southwest subtropical Pacific Ocean (Australia [Abraham Reef], Rarotonga; Druffel & Griffin 2004; Guilderson et al. 2000) record the intensity, frequency, and duration of such upwelling events.

^{14}C in corals can also reflect horizontal advection, made possible by differences in ^{14}C concentrations between specific locations. For example, ^{14}C coral records from Western Indonesia (Langkai) show relative contributions of waters from the ^{14}C -rich North Pacific and the low ^{14}C South Pacific to the Indonesian Throughflow, which varies depending on the direction of the monsoon (Fallon & Guilderson 2008). ^{14}C variations between locations are made larger with the massive amounts of ^{14}C introduced by nuclear weapons testing.

Massive introduction of man-made ^{14}C into the environment caused a major increase in coral ^{14}C levels, marked by a ubiquitous broad peak that often starts at around 1955. This “bomb peak” practically became a time marker that can be used to confirm or establish coral age dates or chronologies. This is, however, not as straightforward because the ^{14}C coral bomb peak varies in timing, magnitude, and shape, depending on the location of the coral (Mahadevan 2001; Grottoli & Eakin 2007). This is caused by differences in ^{14}C concentrations between northern and southern hemispheres, because most nuclear weapons tests were performed in the northern hemisphere (Peng et al. 1998; see Figure 3 for bomb test site locations) and by the effect of physical oceanic processes in the location of the corals.

Looking at some published records of ^{14}C in corals (Figure 19), ^{14}C bomb signal rises and peaks most rapidly in corals located inside the North and South Pacific Gyres. This is because seawater in these locations have long surface residence times and are thus exposed to more atmosphere-ocean CO_2 exchange (e.g., French Frigate and Rarotonga; Druffel 1987; Guilderson et al. 2000; Grottoli & Eakin 2007). This is followed by corals in gyre-fed locations, which show a slight delay in timing of their maximum (e.g., Tamba, Abraham Reef, Japan; Guilderson et al. 2004; Druffel & Griffin 2004; Konishi et al. 1981) West equatorial corals exhibit an even more delayed timing for both onset of increase and peak maximum. Mahadevan (2001) attributes this to increased convection in these locations. Waters from these locations are a mixture of North and South Pacific waters, as the North and South Equatorial Currents (NEC and SEC) converge to feed the North Equatorial Countercurrent (NECC) that supplies the waters in these locations (e.g., Tamba, Nauru; Guilderson et al. 1998; Guilderson et al. 2004). Lastly, east equatorial corals exhibit the most delayed increase in ^{14}C , which in the most recent data available (1982), still has not

reached its peak maximum. This is because of the strong upwelling in this this region, which brings up low ^{14}C waters from the deep ocean (Galapagos; Guilderson & Schrag 1998).

Coral ^{14}C records can also reflect large-scale climate regime shifts such as the El Niño Southern Oscillation (ENSO) and the Pacific Decadal Oscillation (PDO). ^{14}C record of a coral from Solomon Islands (Tambora) show that during El Niño years, the Solomon Sea gets more low ^{14}C east equatorial water transported by the South Equatorial Current (SEC) and less of the relatively higher ^{14}C subtropical water, possibly due to a southward shift of the SEC during El Niño (Guilderson et al. 2004). Galapagos coral also records an abrupt ^{14}C shift in 1976 that coincide with a negative-to-positive phase shift of the PDO, possibly caused by a change in the source of upwelling water in this location (Guilderson & Schrag 1998; Grotoli et al. 2003).

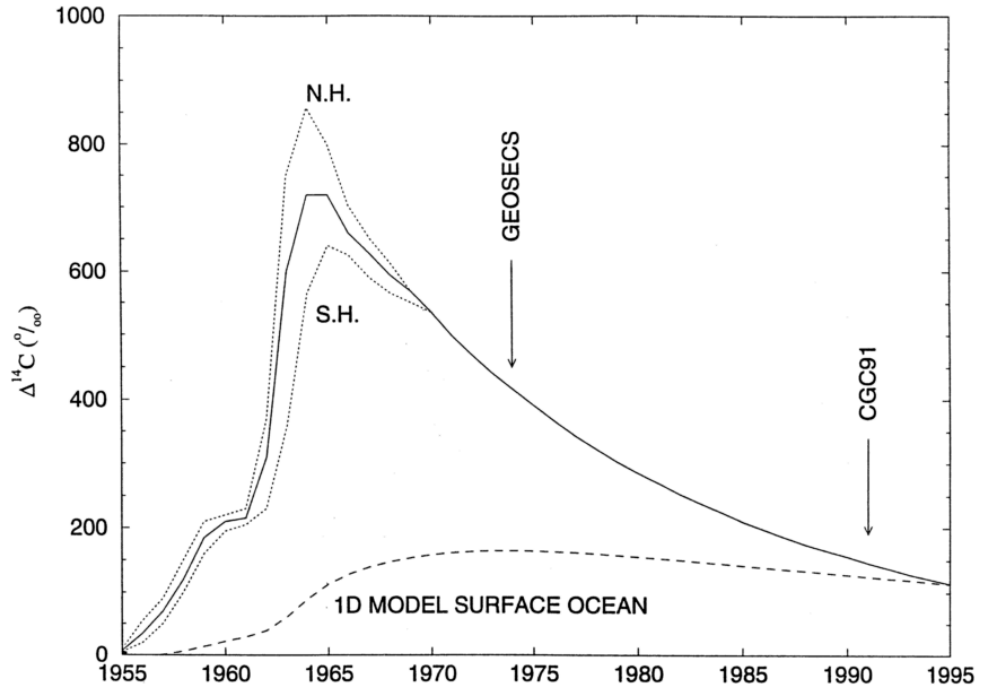


Figure 17. Mean observed atmospheric ^{14}C globally (solid line) and in the northern (N.H.) and southern (S.H.) hemispheres.
From Peng et al. (1998).

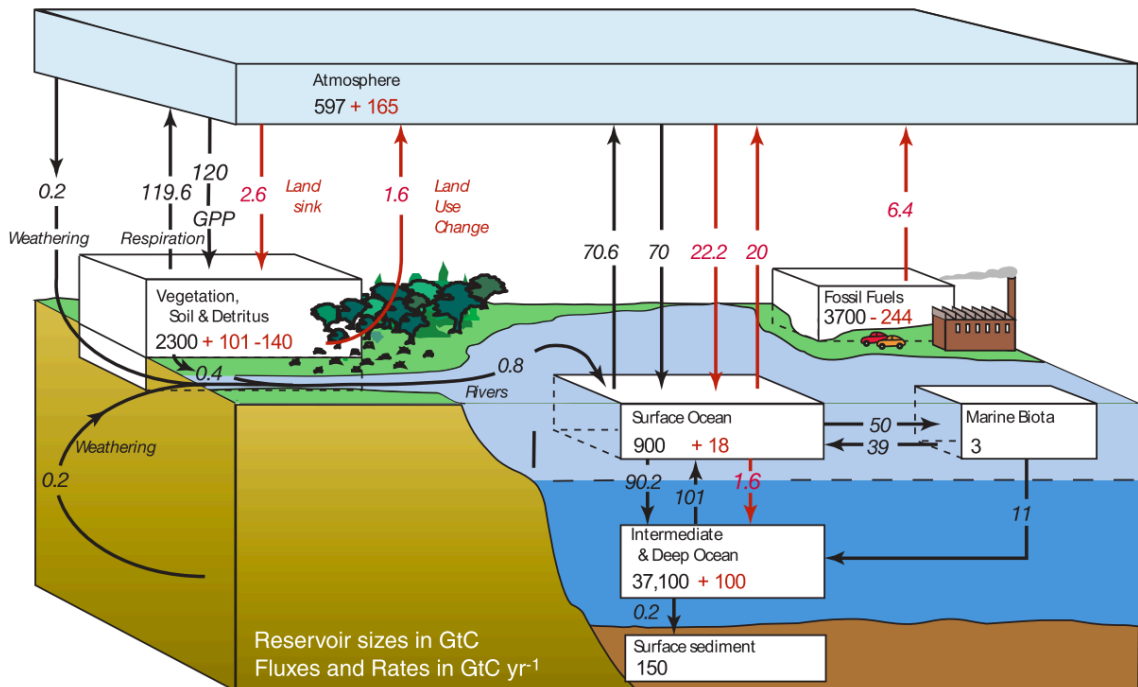


Figure 18. The global carbon cycle.
Inventories in gigaton carbon (GtC) and fluxes are in GtC/yr. Pre-industrial or natural carbon fluxes in black arrows, anthropogenic carbon fluxes in red arrows. From Denman et al. (2007).

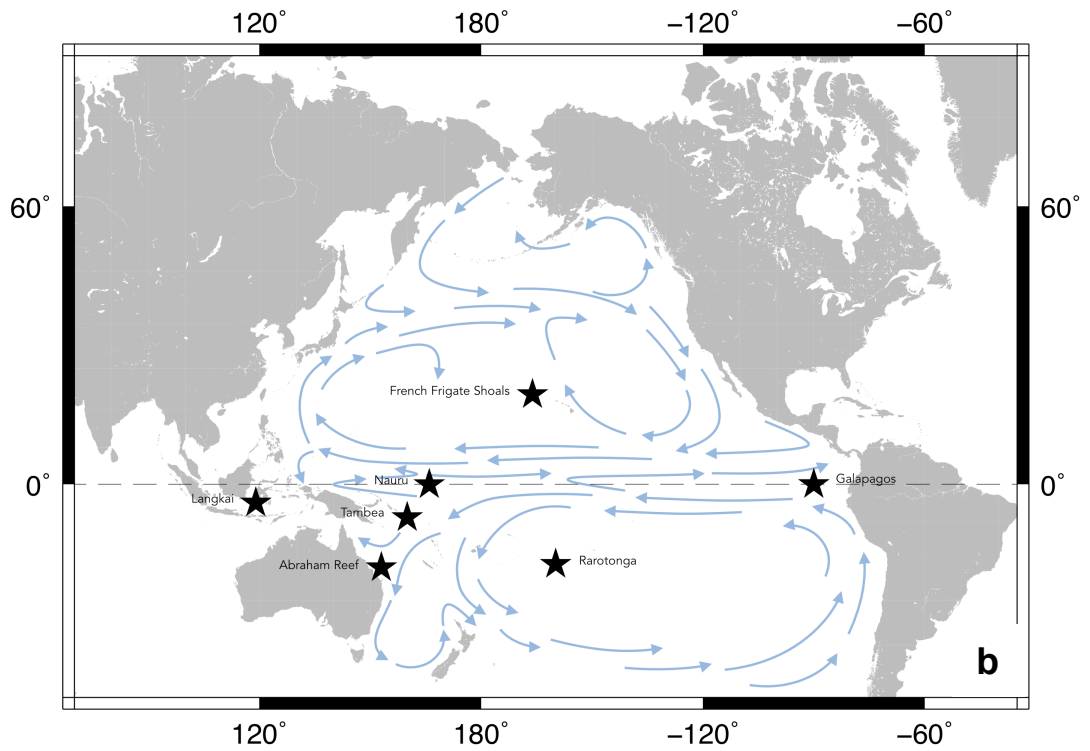
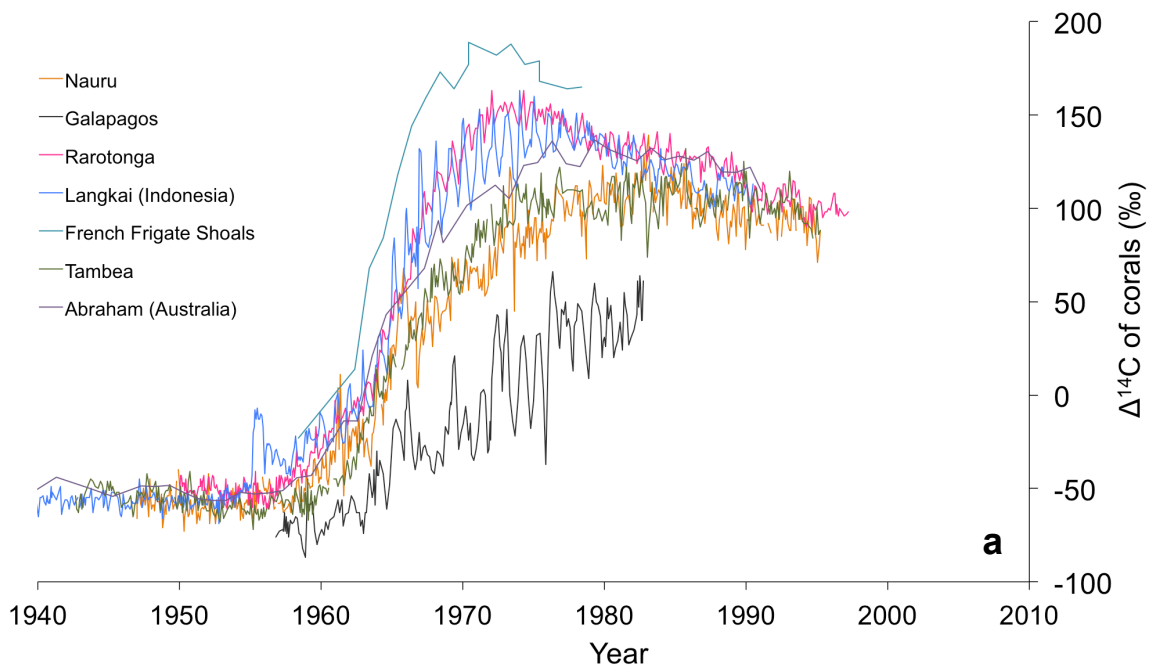


Figure 19. Some published (a) ^{14}C coral records and (b) their locations. Coral record details are shown in Table 3.

This map was produced using the Generic Mapping Tools (Wessel & Smith 2013).

3. Materials and Methods

3.1. Corals

3.1.1. Samples and study sites

Two *Porites spp.* coral cores were drilled in Baler Bay (15°46'N 121°38'E, 3.8m depth) and inside the Parola atoll lagoon of the Spratlys Islands (11°27'N 114°21'E, 10m depth) in the Pacific Ocean (east) and South China Sea (west) sides of the Philippines, respectively. The Philippines is a particularly interesting site because US nuclear bomb tests were performed over the Pacific and signals from these tests, as well as any other signal from across the Pacific Ocean, can be brought directly to the Philippines by trade winds, the North Equatorial Current, and the North Pacific Gyre (Figure 20a); the South China Sea, in contrast, is semi-enclosed and has its own unique and interesting ocean circulation patterns (Figure 20b).

3.1.2. Age model

Portions of the coral cores were x-rayed to reveal annual pairs of low- and high-density growth bands (Figure 21). Preliminary coral age models were constructed by counting back these annual bands from the date of sampling. In the case of Parola, the preliminary age model was further refined using an additional independent age model constructed by comparing coral Sr/Ca measurements (Ramos 2016) and sea surface temperature (SST) variations in the coral location, as estimated by NOAA's Extended Reconstructed Sea Surface Temperature (ERSST; Smith et al. 2008). Coral Sr/Ca, in general, inversely follows SST variations (Shen et al. 1996). Independent age models based on these two methods were found to agree within 2-3 years. An error of ± 0.5 year (arising from disparities between the actual subsampling vs. the distances from the top part of the core used in the Sr/Ca age model) and ± 2.5 years (error of the age

model based on annual band counting, as seen in the comparison with Sr/Ca) are estimated for the age models of Parola and Baler, respectively.

3.1.3. ^{129}I measurement

3.1.3.1. Method Development

At the time of this writing, the only published work about $^{129}\text{I}/^{127}\text{I}$ measurement in corals that was available as reference was that of Biddulph et al. (2006). In their method, about 10-30g of coral samples (*Porites* spp.) are first washed and sonicated in dilute acid to remove external contamination. Samples are then completely dissolved in 1:4 (v/v) $\text{H}_3\text{PO}_4:\text{H}_2\text{O}$ (requires 10.5 mL acid per gram of coral). From the resulting solution, a 50 mL aliquot is obtained for stable ^{127}I measurement using an iodide selective electrode (ISE). The remaining solution is then subjected to multiple solvent extraction steps using CHCl_3 and NaNO_2 . The CHCl_3 phase from this procedure presumably contains iodine from the sample in the form of I_2 . This phase is subsequently added to Ag powder and I_2 is transferred to this solid phase as AgI. CHCl_3 is then evaporated, and the Ag-I solid is rinsed with H_2O and pressed into an aluminum cathode for ^{129}I measurement by Accelerator Mass Spectrometry (AMS).

While this method can measure ^{129}I directly without the use of carrier, it consequently requires a large amount of coral sample. Using smaller coral amounts lowers iodine concentration in the Ag-I solid mixture to levels that may not be detectable by AMS. It also lowers the volume of the resulting coral- H_3PO_4 solution (using the same H_3PO_4 concentration) such that there may not be enough solution for both ^{127}I and ^{129}I measurements (e.g., using 5g of coral results in 52.5mL of solution; ISE uses 50 mL of solution and only 2.5mL will remain for ^{129}I measurement).

However, available coral samples for this dissertation were only typically 1-4 g. Furthermore, A smaller coral sample amount requirement is desired because (1) it will make subsampling along coral growth bands simpler and more specific – subsampling of coral cores and assigning corresponding subsample age dates are often made based on coral growth bands, which are observed through x-ray or luminescence imaging. These growth bands are seldom straight and are best observed by first cutting the coral core sample into slabs prior to imaging (growth bands are difficult to observe on a thick, cylindrical coral core). A small sample requirement may only require working with one slab. A large sample requirement may require as much as more than half of the core and this would mean working on the whole core and cutting uncertainly across it, or working with multiple slabs to be able to both cut faithfully through growth bands and meet the sample amount requirement. Thus, a smaller sample amount requirement is also desired because (2) it enables analyses with higher time resolution or (3) it frees up other parts of the coral core for other analyses or studies.

Given these, I aimed to develop a method capable of measuring ^{129}I and ^{127}I in smaller amounts of coral samples, with the same (or at least acceptable) levels of accuracy and precision. To accomplish this, I modified the method of Biddulph et al. (2006) generally in two aspects: (1) the use of inductively coupled plasma mass spectrometry (ICP-MS) instead of ISE, which will lower the volume requirement for ^{127}I analysis from 50 mL to less than 1 mL; and (2) the use of carrier addition instead of carrier-free method in the preparation of target for AMS analysis, which may enable ^{129}I AMS measurement even with small coral amounts.

Step-by-step procedures for method development are as follows: outer layer of the coral samples were removed by dissolution using 1% (w/w) HCl. Samples were then dissolved completely using 10.5 mL per gram coral of 1:4 (v/v) 85%

H₃PO₄:H₂O. From the resulting solution, a 1 mL aliquot was obtained for ¹²⁷I measurement using ICP-MS. ¹³³Cs internal standard was used and calibration curves using 0, 0.5, 1, 2, and 5 ppb of ¹²⁷I were constructed to ensure measurement accuracy. To minimize matrix effect, dilution factors of 36x, 72x, 143x, and 286x were performed and compared.

Low-ratio Woodward iodine carrier (¹²⁹I/¹²⁷I ratio = 1.5 x 10⁻¹⁴) was then added to the remaining solution (minimum amount was determined to be 0.66mg). Solvent extraction and back extraction using CCl₄ and NaNO₂ was subsequently performed. This procedure is similar to that used by Biddulph et al. (2006) but more closely follows the method reported by Muramatsu et al. (2008; Figure 22). This procedure is more suitable for carrier addition method. From the resulting aqueous phase, AgNO₃ and HNO₃ were added to precipitate the extracted iodine as AgI. Subsequently, AgI precipitate was rinsed once with 10% NH₃ and then twice with deionized H₂O, dried in 80°C for 12 hours, pressed with Nb in aluminum cathodes, and analyzed by AMS in the MALT facility, the University of Tokyo.

Details of the ¹²⁹I AMS measurement are: typical current of 5 μA; sequential injection; cycle sequence of 0.8 ms for ¹²⁷I⁻ and 100 ms for ¹²⁹I⁻; 3.48 MV terminal voltage, +5 charge state for both ¹²⁷I and ¹²⁹I, and a background of ¹²⁹I/¹²⁷I < 2 x 10⁻¹⁴. Complete specifications of the MALT AMS facility is reported by Matsuzaki et al. (2015).

Results of the method development are detailed in Section 4.1. Summary of the final method for measuring ¹²⁹I and ¹²⁷I in coral samples are shown in the following section.

3.1.3.2. ^{129}I measurement method summary

The final method for $^{129}\text{I}/^{127}\text{I}$ measurement in corals used in this study is as follows: Based on annual growth bands, coral subsampling on generally annual and biennial bases were done for Parola and Baler, respectively. Typical sample weights were 2-4g for Baler and 1-1.5g for Parola. Outer layer of the samples were removed by dissolution using 1% (w/w) HCl (resulted to about 11% sample loss). Samples were then dissolved completely using 10.5 mL/ gram coral of 1:4 (v/v) $\text{H}_3\text{PO}_4:\text{H}_2\text{O}$. An aliquot (diluted 286x) was obtained from the resulting solution and analyzed for ^{127}I using inductively coupled plasma mass spectrometry (ICP-MS) analysis. The rest of the solution was used for AgI accelerator mass spectrometry (AMS) target preparation.

AMS target preparation involves solvent extraction and back-extraction using CCl_4 and NaNO_2 for iodine purification (Figure 22). 0.66mg of low-ratio iodine carrier ($^{129}\text{I}/^{127}\text{I}$ ratio = 1.5×10^{-14}) was added to form enough AgI precipitate. AgI precipitation from the solution was done through the addition of AgNO_3 in acidic conditions. AgI was then pressed with Nb in aluminum cathodes and analyzed by AMS in the MALT facility, the University of Tokyo.

Results are reported as $^{129}\text{I}/^{127}\text{I}$ or the ratio of the radioisotope I-129 to the stable isotope I-127. Typical errors for post-1950 Baler and Parola were 9.6% and 13.5%, respectively, while pre-1950 Baler error were about 23%.

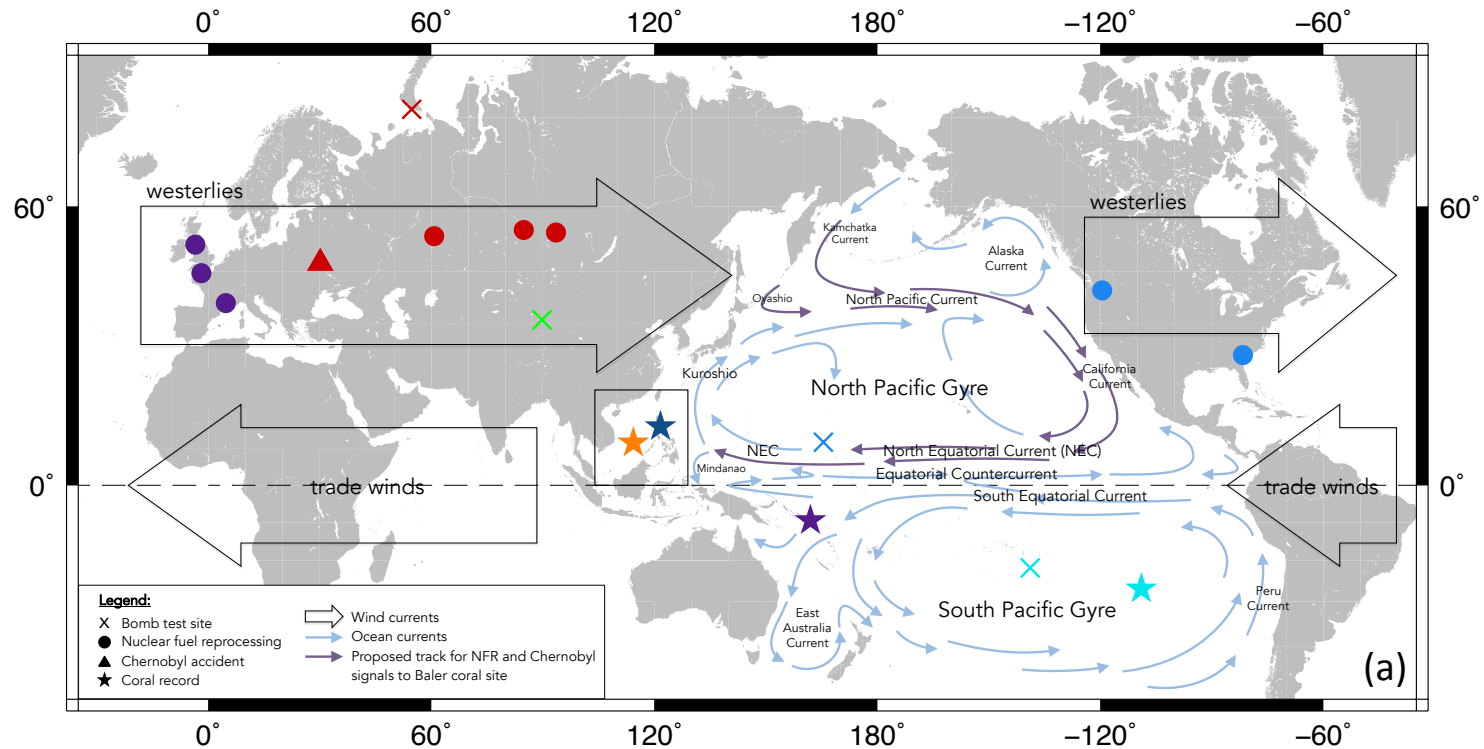


Figure 20. Locations of human nuclear activities, coral records, and major wind and ocean currents.

(a) Locations of major nuclear bomb test sites (crosses, from top-bottom): Soviet Union, China, United States, France; NFR facilities (circles, from L-R): Europe (purple – Sellafield, La Hague, Marcoule), Former Soviet (red – Mayak, Seversk, Zheleznogorsk), United States (blue – Hanford, Savannah River); Chernobyl Accident (red triangle); coral records (stars, from L-R): Parola, Baler, Solomon Is., and Easter Is.; Major wind (block arrows) and ocean currents (blue and violet arrows); Proposed track of NFR and Chernobyl ^{129}I signals around the Pacific towards the Baler coral site (violet arrows); Area marked by the square is shown in (b). This map was produced using the Generic Mapping Tools (Wessel & Smith 2013).

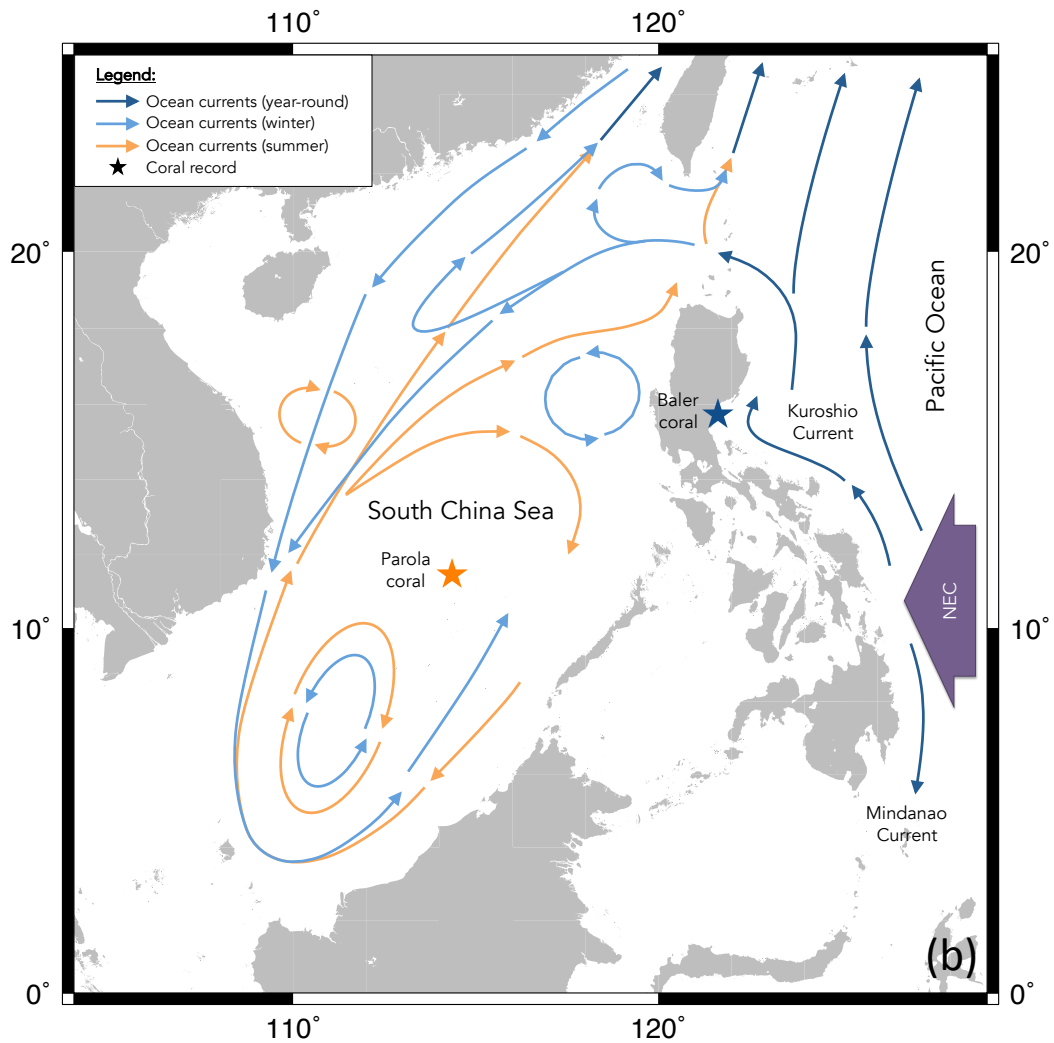


Figure 20 (continued). Locations of human nuclear activities, coral records, and major wind and ocean currents.

(b) Locations of Parola (orange star) and Baler (blue star) coral records; major ocean currents (arrows; Hu et al. 2000) year-round (dark blue), during winter (light blue) and summer (orange). This map was produced using the Generic Mapping Tools (Wessel & Smith 2013).

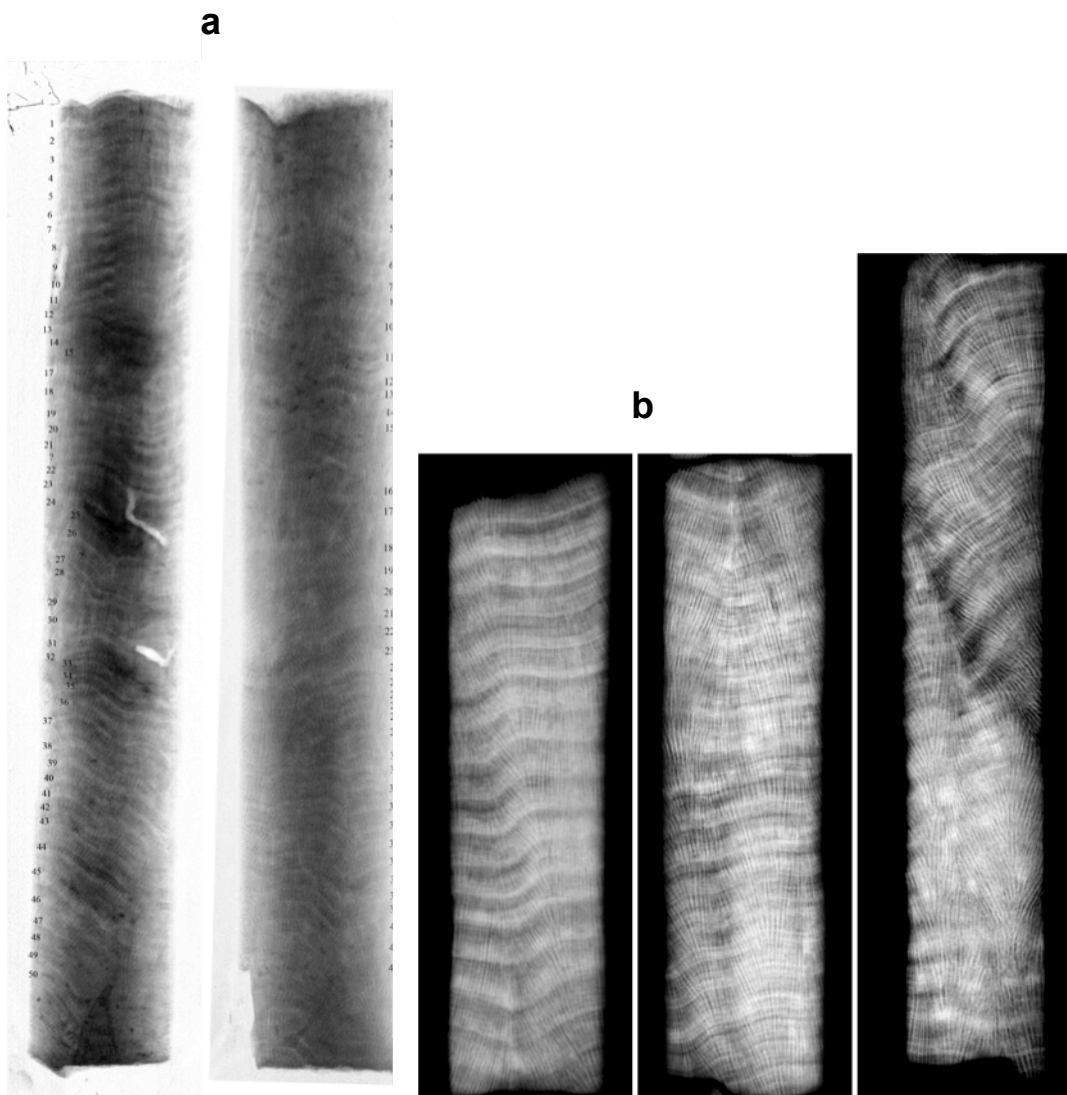


Figure 21. X-ray images of the (left) Baler and (right) Parola corals.

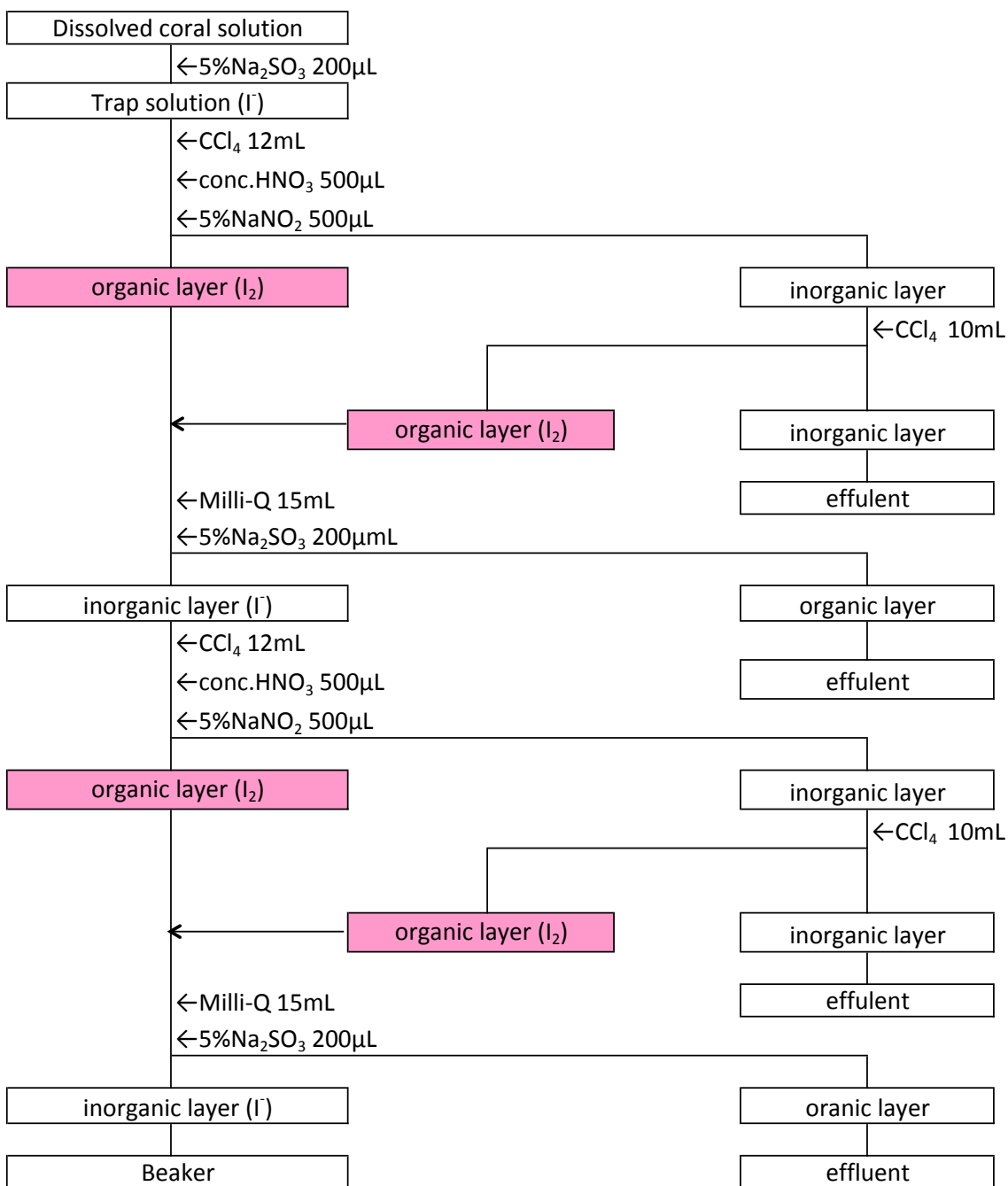


Figure 22. Iodine solvent extraction procedure.

3.1.4. ¹⁴C measurement

10-15 mg of subsamples were collected from each annual growth band for ¹⁴C measurement. These were dissolved in 85% H₃PO₄ under vacuum to produce CO₂ gas. Evolved CO₂ was then cryogenically purified and trapped in a vacuum line then subsequently transformed to graphite using hydrogen and iron catalyst. These were then analyzed by Accelerator Mass Spectrometry (AMS) in the MALT facility, the University of Tokyo. Results are reported as Δ¹⁴C (‰) as defined by Stuiver & Polach (1977) and include δ¹³C correction. The standard used was NIST new oxalic acid (OXII). Typical errors (1σ) are between ± 3 to 6 ‰.

Details of the ¹⁴C AMS measurement are: typical current of 20 μA; sequential injection; cycle sequence of 0.4 ms for ¹³C⁻ and 100 ms for ¹⁴C⁻; 4.8 MV terminal voltage, +4 charge state for ¹²C, ¹³C, and ¹⁴C, and a background of ¹⁴C/¹³C < 3 x 10⁻¹⁶. Complete specifications of the MALT AMS facility is reported by Matsuzaki et al. (2015).

3.1.5. Box mixing model description

The general concept of the box mixing model used in this dissertation is that a certain fraction (denoted by *k*) of a simulated radionuclide amount (e.g., atoms) moves through different atmosphere and ocean boxes, and that *k* is inversely proportional to the lifetime of the radionuclide in that box. The basic description of the model is given by an atmosphere and an ocean box described by the equations:

$$A_t = [I^o + A_{t-1}(1 - k_{A-O})]\Delta t \quad \text{Equation 1}$$

$$O_t = [A_{t-1}k_{A-O} + O_{t-1}(1 - k_{out})]\Delta t \quad \text{Equation 2}$$

A_t and O_t are the amounts (e.g., atoms) of the simulated radionuclide in the atmosphere and ocean at time, t , respectively; I° is an initial, one-time radionuclide input, arbitrarily put in the atmosphere boxes at $t = 1962.0$ (i.e., from nuclear bomb testing); k_{A-O} is the fraction of radionuclide amount in the atmosphere, at any time t , that moves to the ocean box; and k_{out} is the fraction of radionuclide moving out of the ocean box. I assigned k_{A-O} as $1/4 \times$ lifetime of radionuclide in the atmosphere, which for ^{14}C and ^{129}I are 2 and 300 years, respectively. Since k_{A-O} represents the lifetime of the radionuclide in the atmosphere-ocean system, considering the flux for ocean-to-atmosphere (k_{O-A}) can be neglected. k_{out} , on the other hand, represents all processes that decrease radionuclide concentration from the ocean box that were not specifically considered in the model (e.g., migration to deep ocean waters, absorption by biota, diffusion, etc.) and are generally empirically determined.

Figure 23 shows the scheme used to simulate ^{14}C and ^{129}I in the two corals located in the South China Sea (Parola) and Pacific Ocean (Baler) sides of the Philippines. Parola is roughly considered to be a single, isolated system owing to the semi-enclosed nature of the South China Sea (i.e., no advection). This estimation was compensated with a relatively faster k_{out} . Baler, on the other hand, was simulated using 25 boxes, $10^\circ \times 10^\circ$ in size, each with the structure shown in Figure 24, and all interconnected with an advection flux (k_{adv}) that circulates clockwise to simulate the movement of the North Pacific Gyre (Figure 6). Thus for the Baler system, Equations 1 and 2 become:

$$A_{y,t} = [I^\circ a_y + A_{y,t-1}(1 - k_{A-O})]\Delta t \quad \text{Equation 3}$$

$$O_{y,t} = [A_{y,t-1}k_{A-O} + O_{y,t-1}(1 - k_{out} - k_{y,adv}) + O_{y-1,t-1}k_{y-1,adv}]\Delta t$$

$$\text{Equation 4}$$

where y is the box number; a_y is a multiplier that varies with the latitude of the location of the box (also applied for the Parola system) based on observed latitudinal variations of radionuclide deposition (Figure 7); and $k_{y,adv}$ the flux of radionuclide advecting out of the box. The term $O_{y-1} k_{y-1,adv}$ represents the amount of radionuclide advecting into the ocean box O_y , from the previous ocean box O_{y-1} . This notation is consistent except for box 1 (Baler), where box 25 advects into. Values of k_{adv} for each box are based on actual current velocities around the North Pacific Gyre, as determined by Maximenko et al. (2009).

To simulate the effect of a “quick deposit” of a small portion of bomb-derived radionuclide, the atmosphere component was split into two boxes – A_{quick} and A_{slow} , which has different atmosphere-to-ocean fluxes $k_{A-O,quick}$ and $k_{A-O,slow}$. The initial radionuclide input is also divided to the two atmosphere boxes as follows:

$$I_{quick} = I^o \chi_{quick} \quad \text{Equation 5}$$

$$I_{slow} = I^o (1 - \chi_{quick}) \quad \text{Equation 6}$$

where χ_{quick} is the fraction of radionuclide input that deposits quicker than the rest (i.e., designated as 1.5% for this experiment). There are now two separate atmospheric boxes depositing into the same ocean box. The atmosphere and ocean box equations then become:

$$A_{y,t,(quick/slow)} = [I_{(quick/slow)}a_y + A_{y,t-1,(quick/slow)}(1 - k_{A-O,(quick/slow)})]\Delta t$$

Equation 7

$$O_{y,t} = [A_{y,t-1,quick}k_{A-O,quick} + A_{y,t-1,slow}k_{A-O,slow} + O_{y,t-1}(1 - k_{out} - k_{y,adv}) + O_{y-1,t-1}k_{y-1,adv}]\Delta t$$

Equation 8

To simulate increased upwelling in boxes 13-15 (i.e., corresponding to the upwelling area in Central America, as discussed in Chapter 4.4.2.3.), an additional term k_{upw} was added. To simulate the contribution of the Kuroshio recirculation gyre in the Baler site, the terms k_{recirc} and $O_{3,t-1} k_{recirc}$ were added to ocean boxes 3 and 1 (Baler), respectively:

$$O_{y,t} = [A_{y,t-1,quick}k_{A-O,quick} + A_{y,t-1,slow}k_{A-O,slow} + O_{y,t-1}(1 - k_{out} - k_{y,adv} - * k_{upw} - ** k_{recirc}) + O_{y-1,t-1}k_{y-1,adv} + *** O_{3,t-1}k_{recirc}]\Delta t$$

Equation 9

*, **, *** - terms only for boxes 13-15, 3, and 1 (Baler), respectively.

Lastly, to simulate the intrusion of South Pacific waters to the North Equatorial Current (specifically, in boxes 1, 21-25), another isolated system, *SP*, was created, which was similar to the Parola system with the only differences being the radionuclide input was 2 years late, its magnitude 75% of the original, and its k_{out} being slightly different (See Section 4.3.2.1.). Its effect on boxes 1 and 21-25 is expressed in the model as:

$$\begin{aligned}
O_{y,t} = & [A_{y,t-1,quick}k_{A-O,quick} + A_{y,t-1,slow}k_{A-O,slow} \\
& + [O_{y,t-1}(1 - k_{out} - k_{y,adv}) + O_{y-1,t-1}k_{y-1,adv}] * (1 - \chi_{intrusion,y}) \\
& + O_{SP,t-1}\chi_{intrusion,y}]\Delta t
\end{aligned}$$

Equation 10

where $O_{SP,t-1}$ and $\chi_{intrusion}$ represent the radionuclide concentration and degree of intrusion of *SP* to box *y*, respectively. The atmospheric terms remain independent from the *SP* intrusion because theoretically, intruding South Pacific waters are also subjected to the same atmospheric deposition from the time they enter the northern hemisphere, until they mix with the North Equatorial Current.

In the equations used here, $A_{y,t}$, $O_{y,t}$, and I° have unit amounts (e.g., atoms), while k values have the unit wk^{-1} (*per week*), which denote the fraction of radionuclide that is mixing/movement to and from boxes, per time step. All values that we used for the different parameters in these equations are summarized in Table 2.

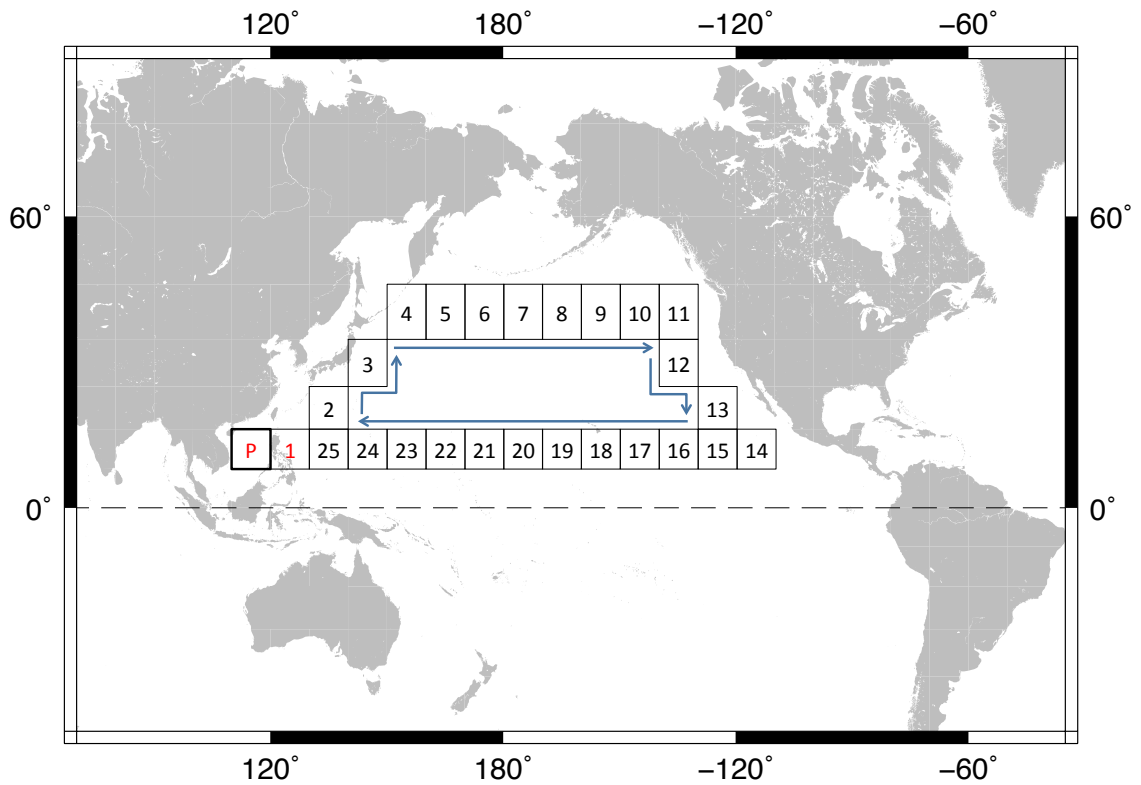


Figure 23. Boxes of the mixing model.

Shown are the Parola system (box P), which is isolated from the other boxes ($k_{adv} = 0$); and the Baler system (boxes 1-25) where Baler is located in box 1 and the direction of advection is shown by the blue arrows. This map was produced using the Generic Mapping Tools (Wessel & Smith 2013).

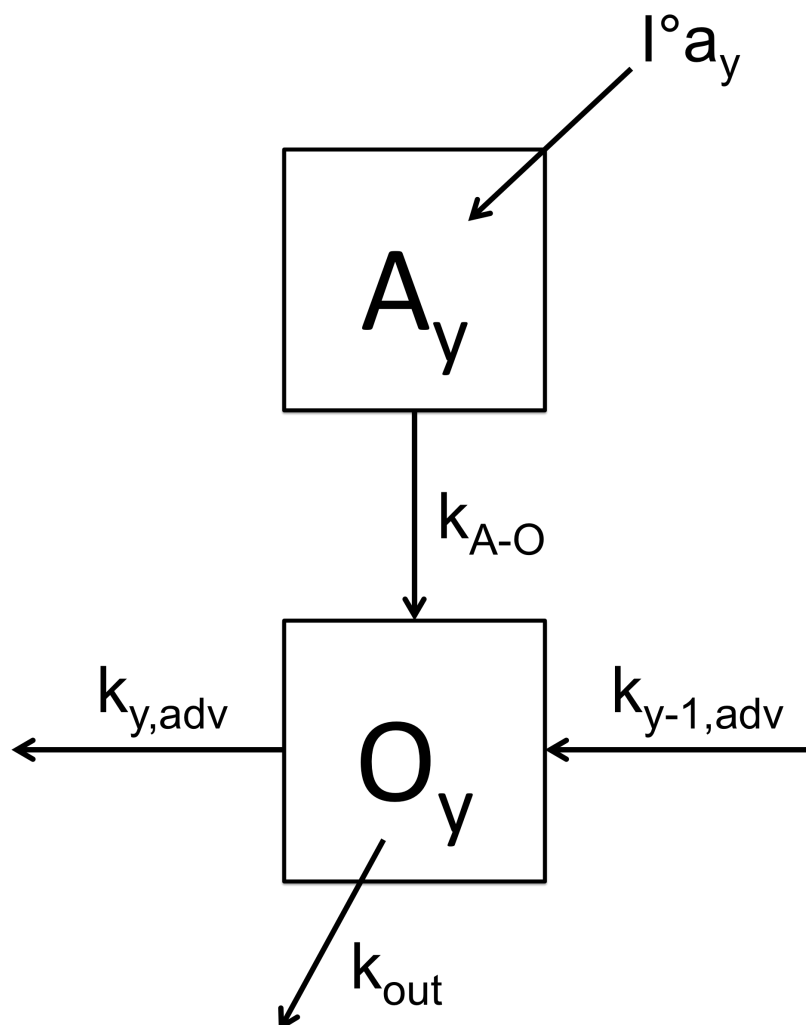


Figure 24. Schematic diagram of the box mixing model.

A_y and O_y are the amounts of the simulated radionuclide in the atmosphere and ocean boxes at position y ; I^0 is the one-time radionuclide input multiplied by a certain factor a_y , which varies with the latitude of the location of the box; k_{A-O} is the fraction of radionuclide moving from the atmosphere to the ocean box; $k_{y,adv}$ and $k_{y-1,adv}$ are the fractions of radionuclide advecting out of the box, and into the box from the previous ocean box (O_{y-1}), respectively; k_{out} is the fraction of radionuclide moving out of the ocean box and represents all processes that decrease radionuclide amount in the ocean that were not specifically considered in the model (e.g., migration to deep ocean waters, absorption by biota, diffusion, etc.).

Table 2. Summary of parameter values used in the box mixing model.

Parameter (unit)	Parola	Baler		South Pacific (SP)
I° (amount)	1000	1000		1000
a_y	See below ^a	See below ^a		See below ^a
k_{A-O} (wk ⁻¹)	See below ^b	See below ^b		See below ^b
k_{out} (wk ⁻¹)	4.982×10^{-3}	3.197×10^{-3}		3.996×10^{-3}
k_{adv} (wk ⁻¹)	–	0.0859 for boxes 1-4, 16-25; 0.0205 for boxes 5-15		–
χ_{quick}	0.015	0.015		0.015
k_{upw} (wk ⁻¹)	–	0.015 ^c		–
k_{recirc} (wk ⁻¹)	–	0.02 ^d		–
$\chi_{intrusion}$	–	<i>pre-1976</i>	<i>post-1976</i>	–
Box 21	–	0.05	0	–
22	–	0.1	0	–
23	–	0.15	0.05	–

^a0.111 for boxes Parola, SP, 1, and 14-25; 0.155 for boxes 2,13; 0.161 for boxes 3,12; 0.221 for boxes 4-11.

^b 3.836×10^{-2} for ¹²⁹I, $k_{A-O,quick}$; 2.557×10^{-4} for ¹⁴C, $k_{A-O,slow}$; These were based from 1/4 x lifetime of radionuclide in the atmosphere (i.e., 2 years for ¹²⁹I and 300 years for ¹⁴C), but expressed in weeks, which is the time step used in these simulations.

^conly used on boxes 13-15, post-1976.

^donly used on boxes 1 and 3, post-1976.

3.2. Ice core

3.2.1. Sample, study site, and age model

The ice core analyzed in this dissertation was drilled at the Southeast Dome site (SE-Dome) in Greenland (67.18°N, 36.37°W; 3,170 masl) in May 2015. The total length of the core is 90.45m and the full details of its sampling is reported by Iizuka et al. (2016). The SE dome site is characterized by high amounts of precipitation, which results to a high ice core accumulation rate of about 1 m/yr. This accumulation rate was used for constructing the preliminary age model of the ice core used in this dissertation.

3.2.2. Sample treatment and ¹²⁹I measurement

Ice core samples were stored and processed in low temperature facilities in the Institute of Low Temperature Science, Hokkaido University in Hokkaido, Japan and in the National Institute of Polar Research, Tachikawa, Tokyo, Japan. Subsampling at 0.5m intervals (corresponding to a time resolution of about 0.5 year) were done inside the low temperature facilities using electric saws, with a subsequent surface cleaning step using ceramic knives. Samples were then put inside capped, plastic containers (cleaned with 1% HNO₃), weighed, and stored until ¹²⁹I pretreatment.

Around 200mL of sample was used for ¹²⁹I measurement. AMS target preparation likewise involved solvent extraction and back-extraction using CCl₄ and NaNO₂ for iodine purification (Figure 22) albeit only being one-step (i.e., coral procedure involved two repeating steps; ice core solvent extraction is only until the first return to the aqueous phase). 0.75mg of low-ratio Woodward iodine carrier (¹²⁹I/¹²⁷I ratio = 1.5 x 10⁻¹⁴) was added to form enough AgI precipitate. AgI precipitation from the solution was done through the addition of AgNO₃ in acidic

conditions. AgI was then pressed with Nb in aluminum cathodes and analyzed by AMS in the MALT facility, the University of Tokyo. ^{127}I content of the ice core samples were determined to be negligible as they were below the instrument detection limit of our ICP-MS system, which is 0.089 ppb (Section 4.1.1).

Results are reported as atoms ^{129}I / mL of H_2O , which is calculated from the results of AMS measurement ($^{129}\text{I}/^{127}\text{I}$ of the sample + carrier), and the known amount of iodine carrier added. Blank measurements and corrections were performed for the AMS analysis, from target preparation to actual measurement.

4. Results and Discussion

4.1. Method development of $^{129}\text{I}/^{127}\text{I}$ measurement in corals

Typical sample amounts used in this study were between 2-4 g for Baler and 1-1.5 g for Parola (Figure 25; weights were taken after washing with 1% HCl and drying). More specifically, ranges of sample amounts were 1.24 to 8.02 g and 0.79 to 4.00 g for Baler and Parola, respectively. Removing the outermost layer of the coral samples using 1% (w/w) HCl generally resulted to an 11% sample loss. Moreover, similar to the report of Biddulph et al. (2006), 10.5 mL of 1:4 (v/v) 85% $\text{H}_3\text{PO}_4:\text{H}_2\text{O}$ (or simply 2.1 mL of 85% H_3PO_4) is needed to completely dissolve one gram of coral sample.

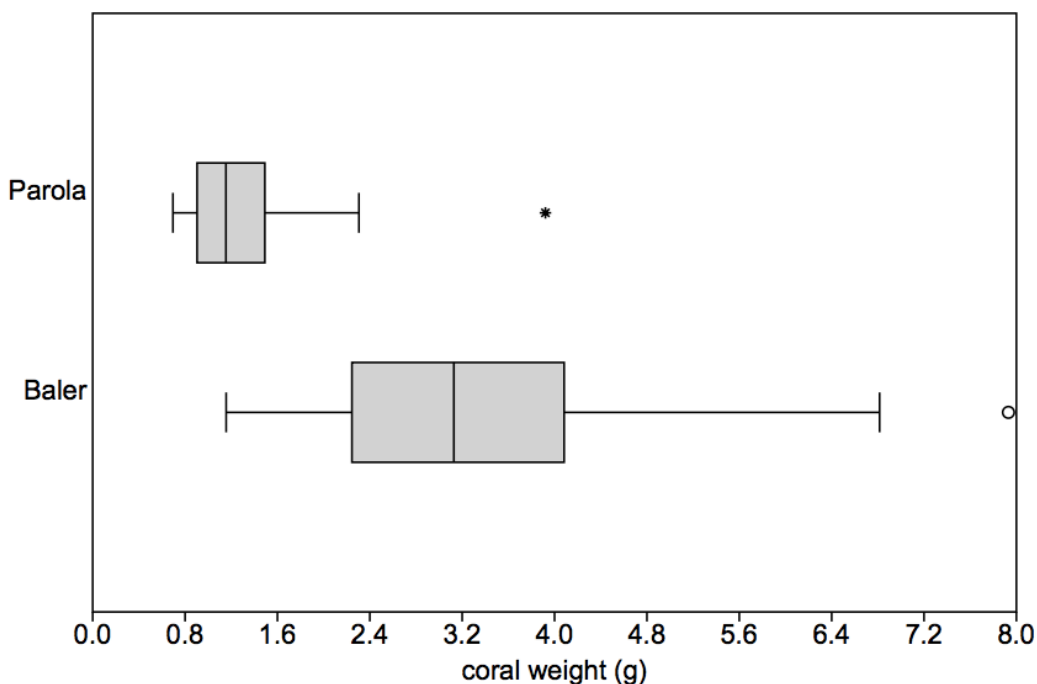


Figure 25. Coral sample weights (in grams) used in this study.

$n = 46$ for both Baler and Parola. Shaded region represents the interquartile range (IQR) or the 25%-75% of the data population (which in this case is 2.3-4.0g and 0.9-1.5g for Baler and Parola, respectively), while the line inside the IQR represents the median (3.1g and 1.1g for Baler and Parola, respectively). Whiskers represent 1.5 x IQR to the left and right of the IQR.

4.1.1. ^{127}I measurement

Inductively coupled plasma mass spectrometry (ICP-MS) is one good option for ^{127}I measurement for our intended purpose particularly because it can easily measure ^{127}I in parts per billion (ppb) levels often with only less than 1 mL of sample solution. However, one factor that should be closely looked at when performing ICP-MS measurements is the matrix effect.

Matrix effect arises when the matrix of the standard solutions used to make the calibration curve is different from that of the sample solutions. This results to difference in signal output between standard and sample (additional matrix in the sample often suppress the signal) and thus an incorrect calibration. In the case of this study, while both standards and samples are adjusted to 1.7% H_3PO_4 matrix, the sample solutions have a lot of Ca^{2+} , CO_3^{3-} , and probably other trace elements in its matrix all coming from the dissolved coral.

One measure I took to compensate for matrix effect is the addition of ^{133}Cs internal standard. Since matrix effect can cause instrument signal discrepancies between standards and samples, a known amount of ^{133}Cs (in this case, 10 ppb) was added to both standard and sample solutions and was used to normalize any variations in signal output. Specifically, the constructed calibration curve is expressed as $^{127}\text{I}/^{133}\text{Cs}$ (signal in cps) vs. $^{127}\text{I}/^{133}\text{Cs}$. (concentration in ppb) and this was used to calculate unknown ^{127}I concentrations in the samples. A good internal standard is: not present in the sample; does not spectrally interfere with sample matrix or analyte elements and masses; and, its mass is near the mass of the analyte (Thomas 2013). ^{133}Cs fulfills these requirements for measurement of ^{127}I . Response of the ICP-MS system was highly linear with ^{127}I concentration within our calibration of 0 to 2 ppb

(average $R^2 = 0.999$, number of calibration curves, $n = 13$) and even up to 5 ppb ($R^2 = 0.995$, $n = 6$).

Using this method, an average calibration curve slope (S) of 0.041 and blank standard deviation (σ) of 0.00011 ($n = 13$) was determined. Using these, instrument detection limit (IDL) and limit of quantification (LOQ) were calculated to be 0.089 and 0.27 ppb of ^{127}I , respectively for our method and ICP-MS system. IDL is defined as the lowest amount of analyte in a sample that can be detected by the method but not necessarily quantitated and is equal to $3.3\sigma / S$. On the other hand, LOQ is the lowest amount of analyte that can be quantitatively measured by the method with suitable precision and accuracy and is equal to $10\sigma / S$ (ICH 2005). Calculated values were in $^{127}\text{I}/^{133}\text{Cs}$ (ppb/ppb) and the amount of ^{133}Cs added (10 ppb) was multiplied to these values to get IDL and LOQ in ^{127}I ppb.

Another measure that I used to compensate for matrix effect is dilution of sample solutions. As dilution factor of sample solution increases, matrix effect should decrease. This is illustrated in a trial coral analysis performed using dilution factors of 36x, 72x, 143x, and 286x, where both $^{127}\text{I}/^{133}\text{Cs}$ (cps) and the calculated ^{127}I in coral (ppm) plateau with increasing dilution factor (Figure 26). While it is ideal to decrease matrix effect by increasing dilution infinitely, dilution factor should only be increased until the resulting ^{127}I concentration of the sample solution after dilution is equal or just above the LOQ (0.27 ppb). Based from the report of Biddulph et al. (2006), ^{127}I in their corals samples have a mean concentration of 3.4 ppm. A coral sample with this ^{127}I concentration, when dissolved with 10.5 mL of 1:4 (v/v) $\text{H}_3\text{PO}_4:\text{H}_2\text{O}$ per gram of coral and subsequently diluted to 286x, will yield about 1 ppb of ^{127}I sample solution, which is safely above the LOQ of 0.27 ppb. Therefore, I decided to use a dilution factor of 286x for the rest of the samples in this study.

Resulting ^{127}I concentrations of analyzed (diluted; in ppb) sample solutions and their corresponding concentration in ppm of coral are shown in Figure 27. Resulting ^{127}I concentrations of diluted sample solutions were mostly between 1-1.5 ppb. Entire range was between 0.6-2.1 ppb. These are all above the LOQ and within calibration range. From these, calculated ^{127}I in corals (ppm) were mostly between 3.7-5.4 ppm. These results agree with the report of Biddulph et al. (2006), wherein ^{127}I concentrations varied little throughout the coral core (Figure 28) and were about 100x higher than that in seawater (~52 ppb), confirming the biophilic nature of iodine.

Measurements have an average relative standard deviation (1σ) of $1.8\% \pm 0.8\%$ and is shown as error bars in Figure 28. Repeat experiments ($n = 4$), wherein the whole procedure was performed on the same sample twice show an average standard deviation of 0.09 ppm of ^{127}I in coral, demonstrating the repeatability of the method. ^{127}I values and corresponding 1σ errors are summarized in **Appendix A**.

Using a dilution factor of 286x, this ^{127}I measurement method only required 0.0175 g or roughly 17.5 μL of the sample solution and was able to measure ^{127}I in corals with an acceptable degree of accuracy and precision.

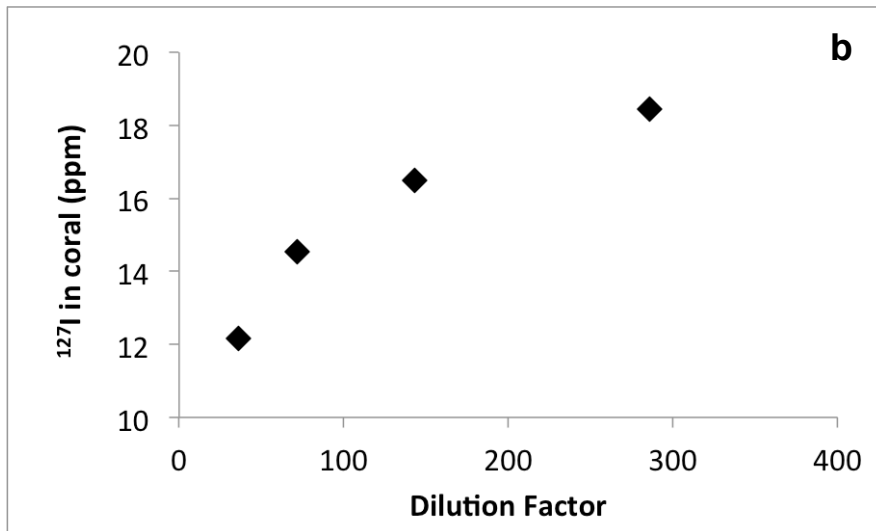
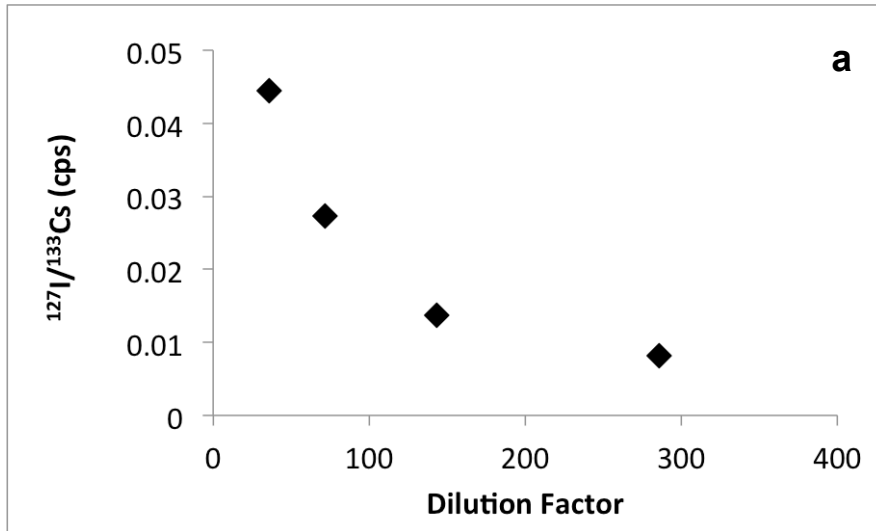


Figure 26. (a) $^{127}\text{I}/^{133}\text{Cs}$ (cps) and (b) ^{127}I in coral (ppm) with increasing dilution factor.

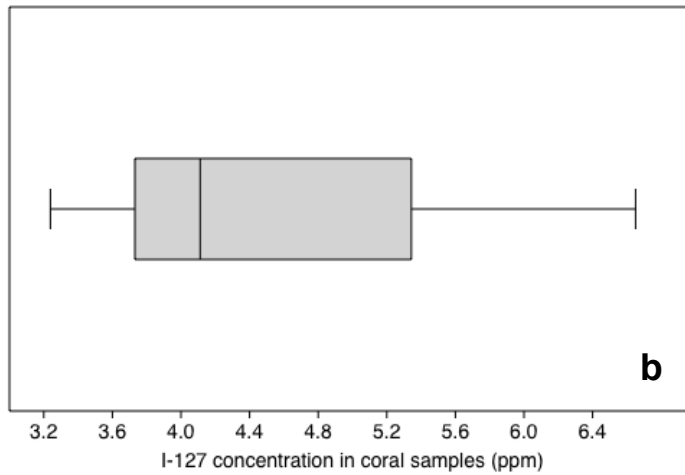
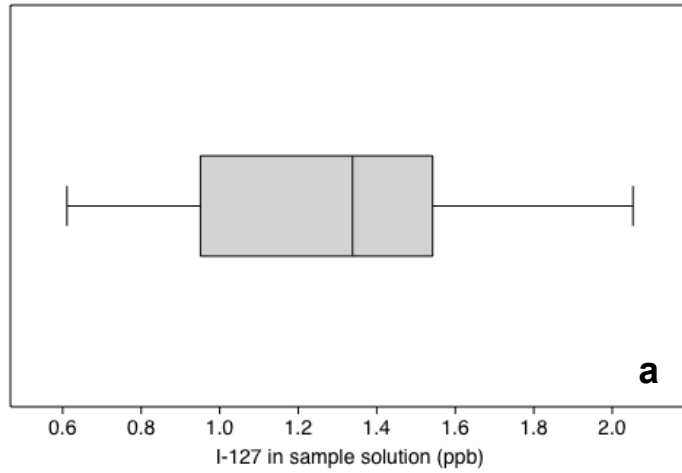


Figure 27. ^{127}I concentrations of (a) analyzed (diluted; in ppb) sample solutions and (b) corresponding concentration in ppm of coral.
 n = 93. Shaded region represents the interquartile range (IQR) or the 25%-75% of the data population, while the line inside the IQR represents the median. Whiskers represent 1.5 x IQR to the left and right of the IQR.

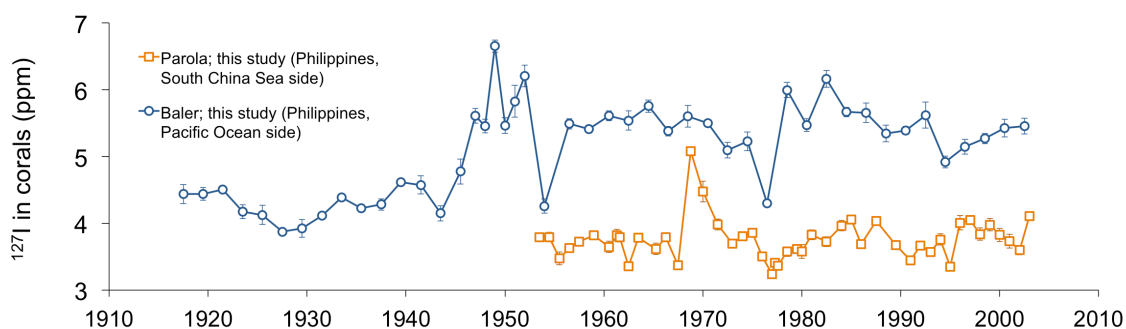


Figure 28. ¹²⁷I (ppm) in Baler and Parola coral cores and their corresponding errors (1σ).

4.1.2. ¹²⁹I measurement

Low-ratio iodine carrier ($^{129}\text{I}/^{127}\text{I}$ ratio = 1.5×10^{-14}) was added to remaining sample solutions prior to solvent extraction. Iodine carrier is added to increase the amount of iodine in the solution to enable formation of enough AgI precipitate for AMS measurement. However, adding too much carrier will down the native ¹²⁹I signal of the sample. Therefore, the ideal is to add as little amount of carrier as possible, just enough to produce sufficient AgI precipitate for AMS measurement. The resulting $^{129}\text{I}/^{127}\text{I}$ ratio should also be sufficiently higher than that of the carrier.

With this purpose in mind, I first tried using 0.33 mg of carrier but was unsuccessful in forming enough precipitate for AMS analysis. Next I tried using 0.66 mg and consistently found that enough AgI precipitate (i.e., sample + carrier) can be produced with this amount of carrier. Thus, I used 0.66 mg of iodine carrier for the rest of the samples.

Measurement of the blank, which contains only iodine carrier, resulted to a $^{129}\text{I}/^{127}\text{I}$ ratio of $(1.8 \pm 0.7) \times 10^{-14}$, which is close to the expected value of 1.5×10^{-14} . The resulting $^{129}\text{I}/^{127}\text{I}$ ratio of the AgI precipitate is shown in Figure 29. Ratios were mostly in the range of 6.5 to 26.7×10^{-14} , and the minimum value obtained was 2.7×10^{-14} . These values are well above the carrier $^{129}\text{I}/^{127}\text{I}$ ratio of 1.5×10^{-14} , and thus

fulfill our intended purpose. Relative standard deviations of the measurements are typically between 8.4% and 19.1%. AMS measurement is the main source of error for the entire method and is a drawback for using smaller sample sizes. This is discussed in more detail in the next section.

4.1.3. Coral $^{129}\text{I}/^{127}\text{I}$ results

Resulting $^{129}\text{I}/^{127}\text{I}$ ratios of the corals from this study and those reported by Biddulph et al. (2006) are shown in Figure 30. Discussions about how these results record the history of human nuclear activities and reflect atmospheric and oceanic circulations are discussed separately in Section 4.2. Discussions here are more focused on the comparison of results using the method discussed here and that in the work of Biddulph et al. (2006).

$^{129}\text{I}/^{127}\text{I}$ ratios of different coral records are best compared in parts dated before year 1950 because ^{129}I during this period is presumed to come only from natural sources, which is relatively constant. Natural ^{129}I marine reservoir is relatively constant geographically and across time because its long oceanic residence time of ^{129}I (40,000 years; Fabryka-Martin et al. 1985) is greatly longer than the turnover time of oceans (1000 years; Moran et al., 1998). Coral records from Baler, Solomon, and Easter islands demonstrate this by having relatively uniform $^{129}\text{I}/^{127}\text{I}$ ratios before the 1950s, compared to the large discrepancy observed after the year 1950. More specifically, corals from Solomon and Easter islands have pre-1950 ratios of about 5×10^{-13} , while the Baler record only has a slightly higher average ratio of about 1.4×10^{-12} . Parola coral was not long enough to include pre-1950 record. Estimate of the natural $^{129}\text{I}/^{127}\text{I}$ ratio based on shallow marine sediments and archived seaweed is 1.5×10^{-12} (Moran et al. 1999; Cooper et al. 1998). Average pre-1950 ratio of the Baler

record is thus closer to this widely accepted shallow ocean natural ratio and this adds confidence to the accuracy of our method.

It is difficult to verify the accuracy of $^{129}\text{I}/^{127}\text{I}$ ratios of corals post-1950, wherein human nuclear activities have introduced massive amounts of ^{129}I to the environment, because of the variability $^{129}\text{I}/^{127}\text{I}$ ratios depending on the location and age date of the coral record (He et al. 2013) and because of the absence of any reference material or any previous estimates for corals in the northern hemisphere. However, it is interesting to note that nearly identically peaks were observed in Baler ($^{129}\text{I}/^{127}\text{I} = 33.2 \times 10^{-12}$) and Parola (29.7×10^{-12}) in the year 1962. This year marks the highest peak of aboveground bomb testing throughout history (UNSCEAR 2000).

Typical errors for anthropogenic (post-1950) Baler and Parola were 9.6% and 13.5%, respectively, while natural (pre-1950) Baler errors were about 23%. The study by Biddulph et al. (2006), on the other hand, had average anthropogenic- and natural-age errors of 8% and 35%, respectively (Figure 30). The method presented here was able to measure ^{129}I and ^{127}I in corals with accuracy and precision, comparable to the work of Biddulph et al. (2006), even with sample sizes of only about 1-4 g. Our method performed better (i.e., had lower error levels) for natural-age (low ^{129}I) coral samples. Results of anthropogenic-age samples were also acceptable albeit with larger (by about 1.6% to 5.5%) error levels. Parola samples, in particular, had errors of about 13.5% because of the small sample size used in the measurement (Figure 25).

In particular, I found that error levels exponentially increase with decreasing AgI precipitate ratio (i.e., ratio of the sample + carrier; Figure 31a). Fitting a logarithmic function to the 1/RSD vs. precipitate ratio gives the equation $y = 3.6338\ln(x) + 15.609$ with an R^2 value of 0.85429 (Figure 31b). Using this equation and given an average ^{127}I concentration of 4.5 ppm and a natural and anthropogenic $^{129}\text{I}/^{127}\text{I}$ ratio of

20 and 1.5×10^{-12} , respectively, measurement of $^{129}\text{I}/^{127}\text{I}$ with a target error level of 10% (i.e., AgI precipitate should have $^{129}\text{I}/^{127}\text{I}$ ratio of about 0.213×10^{-12}), is possible with our method using 1.5 g and 22.5 g of anthropogenic- and natural-age coral samples, respectively. Measurement using smaller sample sizes is also possible, but error levels will increase exponentially with decreasing sample size. The expected error of this method, using our instrument measurement system, may be estimated for any sample size through the equation of the fitted line ($y = 3.6338\ln(x) + 15.609$) shown in Figure 31b. Summary of the method developed here is shown in Section 3.1.3.2.

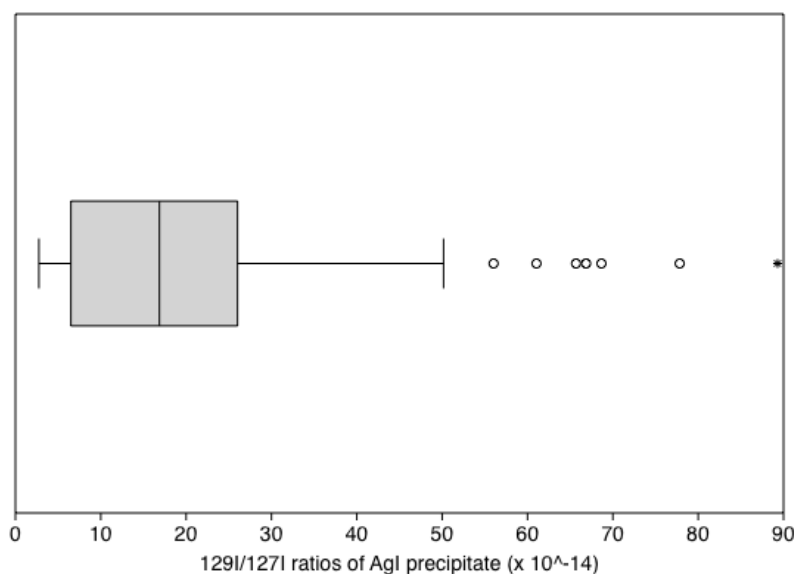


Figure 29. $^{129}\text{I}/^{127}\text{I}$ ratios of AgI precipitate (sample + carrier) in $\times 10^{-14}$. $n = 93$. Shaded region represents the interquartile range (IQR) or the 25%-75% of the data population (which in this case is 6.5-26), while the line inside the IQR represents the median (16.9). Whiskers represent $1.5 \times \text{IQR}$ to the left and right of the IQR.

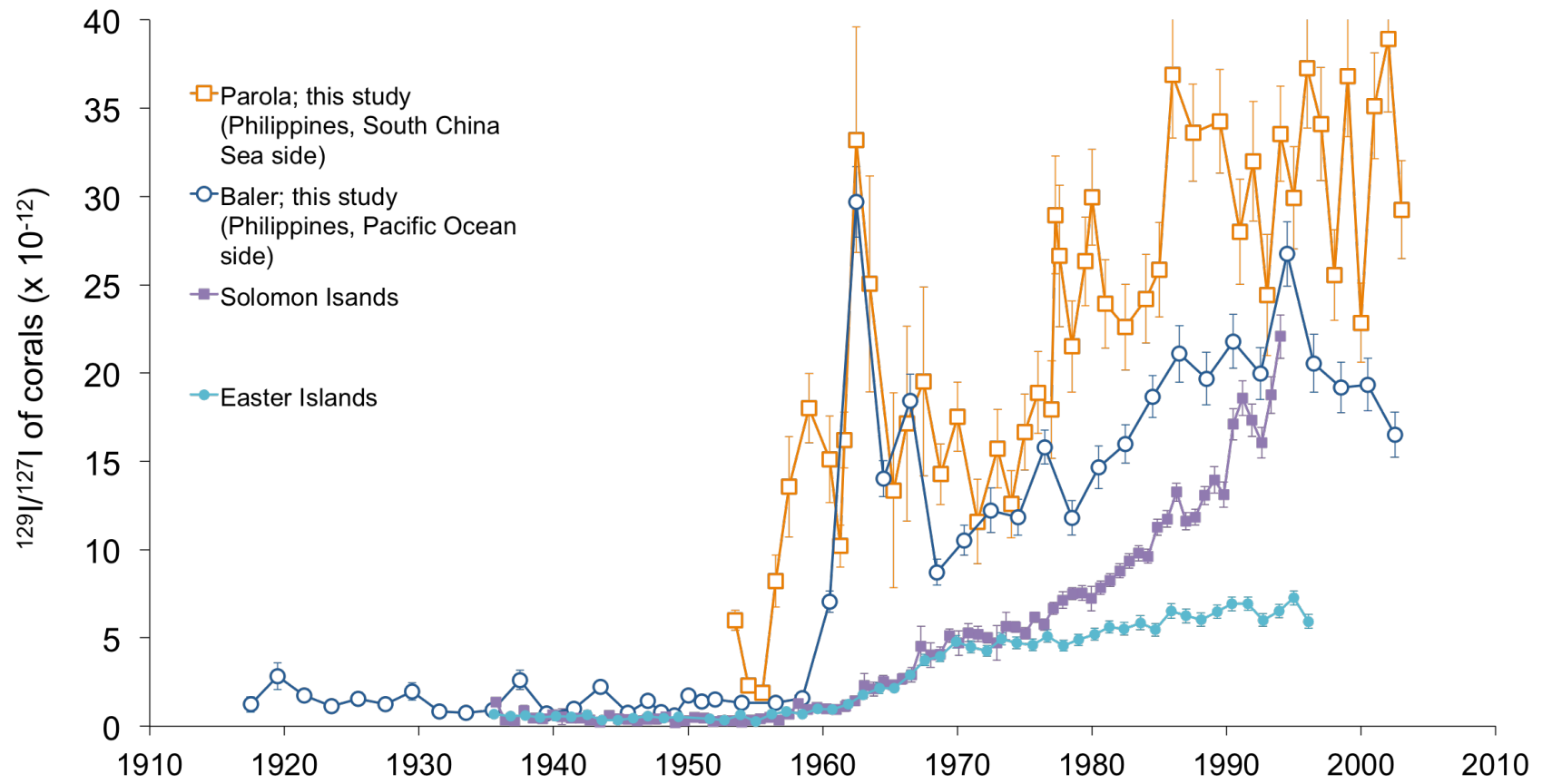


Figure 30. $^{129}\text{I}/^{127}\text{I}$ of Corals and their corresponding errors (1σ).

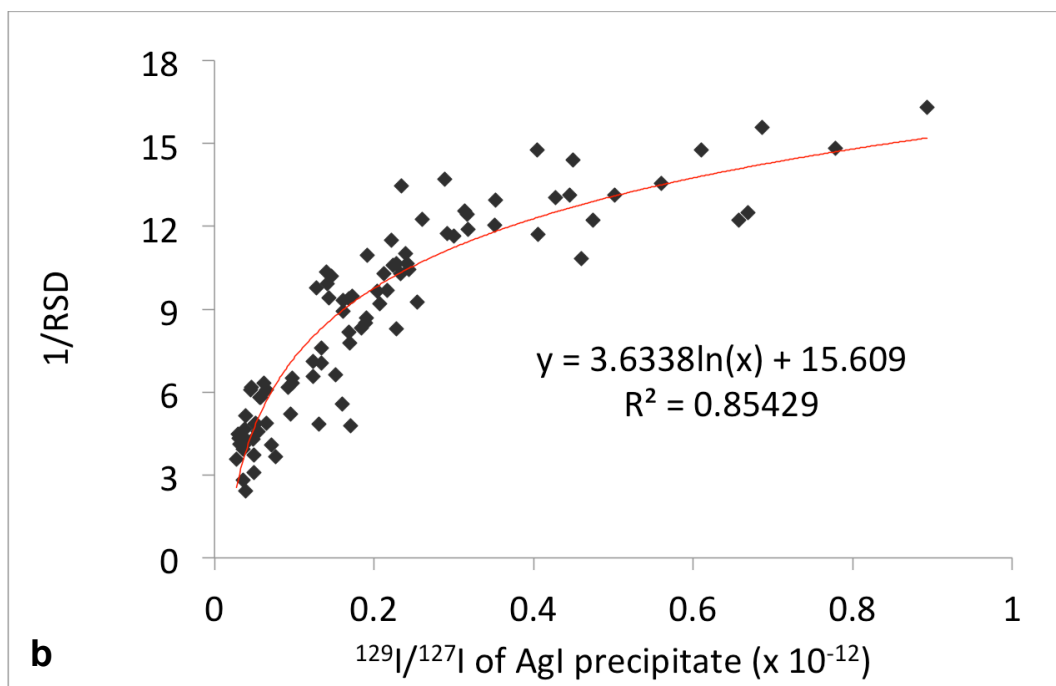
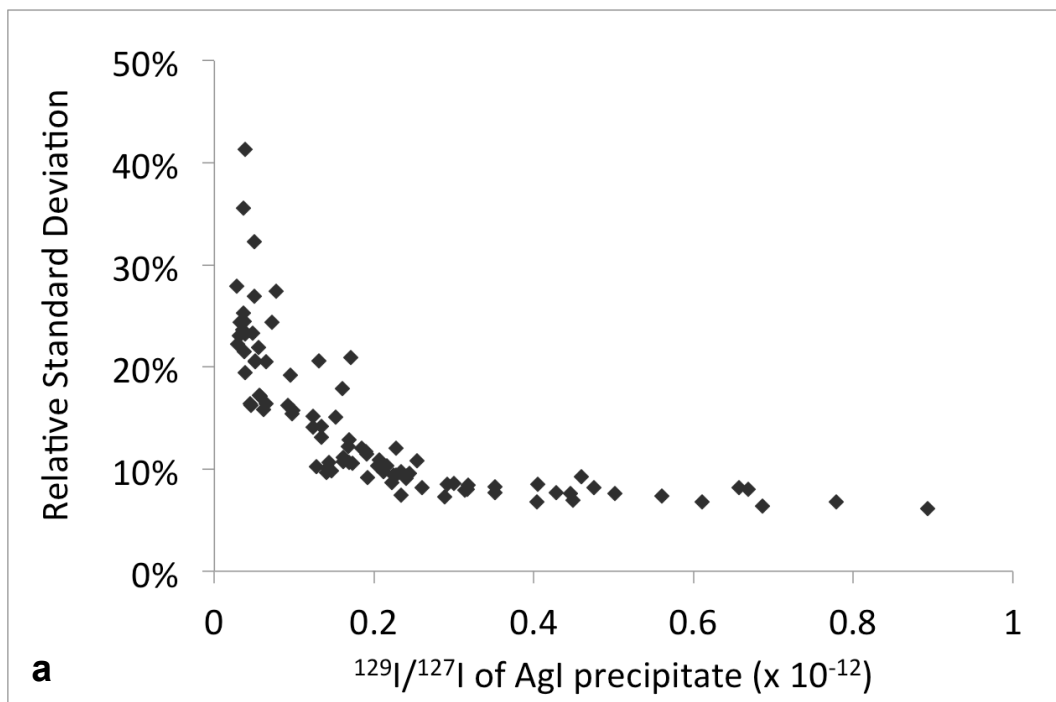


Figure 31. Relative standard deviation (RSD) vs. ratio of AgI precipitate.
 (a) RSD vs. $^{129}\text{I}/^{127}\text{I}$ ($\times 10^{-12}$) of the AgI precipitate; (b) $1/\text{RSD}$ vs. $^{129}\text{I}/^{127}\text{I}$ ($\times 10^{-12}$) of the AgI precipitate, fitted with a logarithmic function (red line).

4.2. ^{129}I in corals from the Philippines

Figure 32 shows the $^{129}\text{I}/^{127(\text{stable})}\text{I}$ time series profiles of the Baler (Pacific Ocean side) and Parola (South China Sea or SCS side) corals as well as southern hemisphere coral records from the Solomon and Easter Islands (Biddulph et al. 2006). For raw data of ^{127}I , $^{129}\text{I}/^{127}\text{I}$, and corresponding error values, see **Appendix A**. Discussion of results is done in four phases: natural (pre-1950), bomb (1951-1976), nuclear fuel reprocessing (NFR) and the Chernobyl accident (1977-1996), and post-1996.

4.2.1. Natural (pre-1950)

Before 1950, virtually no human nuclear activities were releasing ^{129}I to the environment (Figure 32a and b). Therefore, ^{129}I during this phase is presumed to come only from natural sources. Estimate of the natural $^{129}\text{I}/^{127}\text{I}$ ratio based on shallow marine sediments and archived seaweed is 1.5×10^{-12} (Moran et al. 1999; Cooper et al. 1998). Baler ^{129}I ratios agree with this estimate, having an average pre-1950 $^{129}\text{I}/^{127}\text{I}$ ratio of $1.4 \pm 0.7 \times 10^{-12}$. Moreover, corals from Baler, Solomon, and Easter islands show relatively uniform $^{129}\text{I}/^{127}\text{I}$ ratios before the 1950s. This demonstrates that natural ^{129}I concentration in the oceans was practically constant across hemispheres and across time. This well-mixed global ^{129}I ocean reservoir is the result of the long oceanic residence time of ^{129}I (40,000 years) being largely longer than the turnover time of oceans (1000 years; Moran et al., 1998).

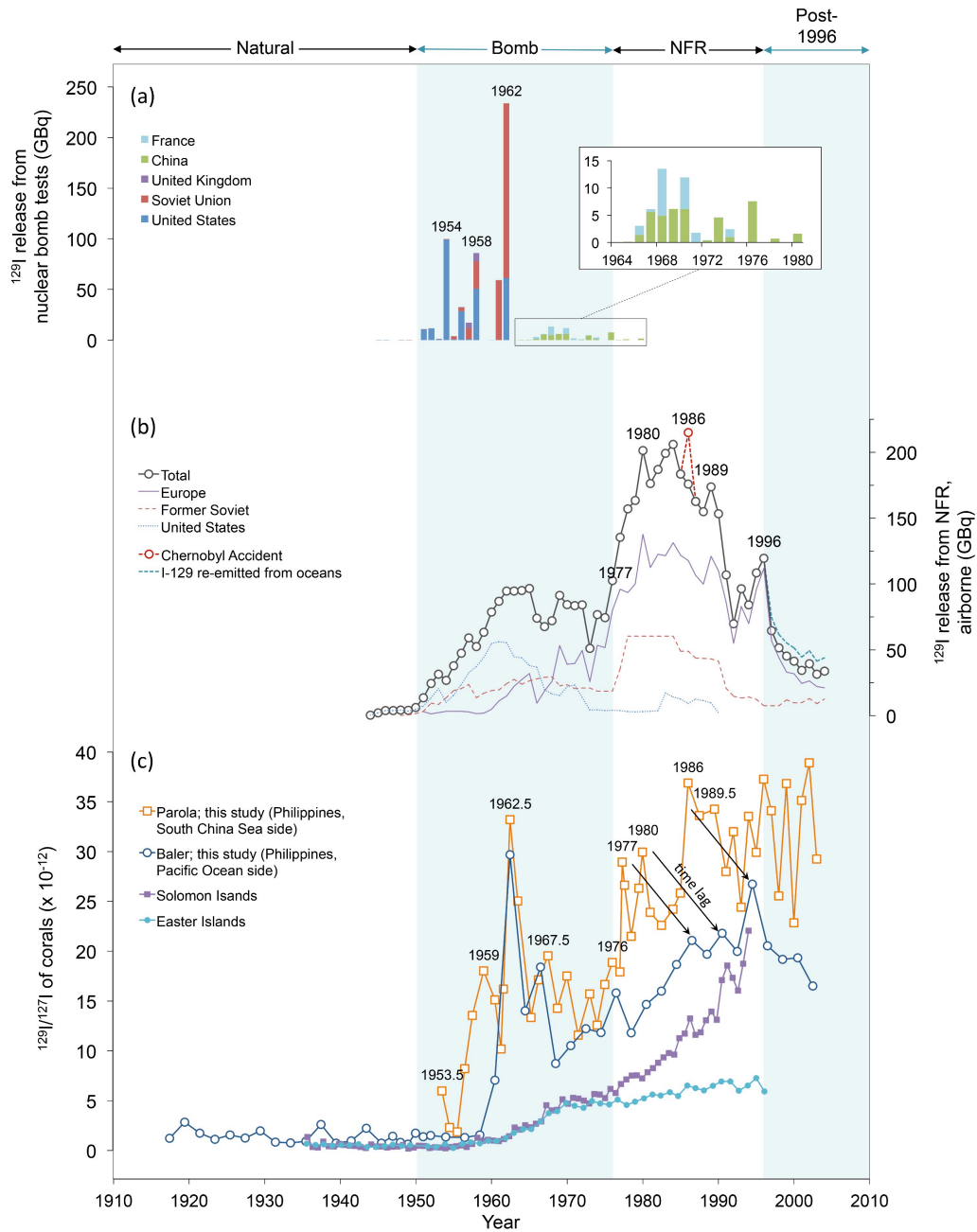


Figure 32. ^{129}I from nuclear activities and as observed in coral records.

(a) ^{129}I released from nuclear bomb tests of various countries in GBq, estimated from fission yield using a fast fission yield of 1.6% (Reithmeier et al. 2006); (b) Airborne ^{129}I emissions from nuclear fuel reprocessing (NFR) facilities in Europe, Former Soviet, United States, and their total (Reithmeier et al. 2010; Reithmeier et al. 2006); also shown are the contribution of the Chernobyl Accident (39 GBq; Aldahan et al. 2007) and ^{129}I re-emitted from the ocean (about 10 GBq/yr; Reithmeier et al. 2006) added to the total of NFR emissions; (c) $^{129}\text{I}/^{127}\text{I}$ of corals from the northern (Parola and Baler, this study) and southern hemispheres (Solomon and Easter Islands; Biddulph et al. 2006); Alternating white and blue bars show different phases of dominant ^{129}I contribution as discussed in this paper: natural (pre-1950), bomb (1951-1976), NFR (1977-1996), and post-1996.

4.2.2. Bomb (1951-1976)

Years 1951-1976 mark the height of nuclear bomb testing, with the United States and the former Soviet Union performing tests in 1951-1962, and China and France in 1964-1976 (Figure 32a).

For years 1951-1962, the peak of the bomb tests was in 1962. This event appears to be recorded almost identically in the Baler ($^{129}\text{I}/^{127}\text{I} = 33.2 \times 10^{-12}$) and Parola corals (29.7×10^{-12}), which are both in the northern hemisphere. This signal was not observed in corals from the southern hemisphere (Solomon and Eastern Islands), and this is expected because the residence time of ^{129}I in the atmosphere (2-4 weeks in the troposphere and 3 months to 2 years in the stratosphere) is faster than the atmospheric exchange between the northern and southern hemispheres (2 years). This observation also agrees with the observed global ^{90}Sr deposition measurements (Figure 7; UNSCEAR 2000).

The 1962 ^{129}I bomb peak offers a new time marker that can be used to set age models of modern corals from the northern hemisphere. It will be interesting to compare this to the coral ^{14}C bomb peak, which is a broad peak that varies in timing, magnitude, and shape, depending on the oceanic regime in the location of the coral (Mahadevan 2001). I hypothesize that the ^{129}I bomb peak will be more uniform in shape and timing than the ^{14}C bomb peak, regardless of oceanic regime, mainly because of the shorter atmosphere-to-ocean residence time of ^{129}I compared to that of ^{14}C (7-10 years). This should result to a sharper ^{129}I peak that is less affected by oceanic processes. The ^{129}I bomb signal is ubiquitous around the northern hemisphere, only differing in magnitude between different latitudes (Figure 7; UNSCEAR 2000; Reithmeier et al. 2006).

Also notable are the pre-1962 bomb tests, which were mostly done by the US in the Pacific Ocean. These tests are different from the others because a high percentage (around 44%; Figure 4) of their bomb-derived radionuclides were injected in the local, regional, and tropospheric layers and presumably transported to the Philippines by trade winds and the North Equatorial Current (Figure 20a). Interestingly, ^{129}I signals from pre-1962 tests were observed in Parola (1953.5 and 1959), but not in Baler. Given that the North Equatorial Current always passes through Baler before it reaches Parola (Figure 20b), these results suggest that ^{129}I bomb signals from these tests are transported mainly through the atmosphere than through the ocean. These localized signals may have been sufficiently detectable in the smaller, semi-enclosed, and shallower SCS but diluted in the larger and deeper Pacific Ocean. Furthermore, additional ^{129}I input may come from atmospheric ^{129}I deposition over land catchments that drain directly to the SCS via rivers and surface runoff, and this should elevate ^{129}I in Parola further.

Chinese and French tests during 1964-1976 also appear to be recorded concurrently in both Baler and Parola, particularly in years 1967.5 and 1976. Parola also shows peaks in 1970 and 1973, although error levels are not sufficient to conclude this.

4.2.3. Nuclear Fuel Reprocessing (NFR) and the Chernobyl Accident (1977-1996)

^{129}I signals in Parola in 1977, 1980, and 1986 coincide with emission peaks during the height of NFR ^{129}I airborne emission as well as with the Chernobyl Accident (Figure 32b and c). The Chernobyl Accident happened in April 26, 1986 and released approximately 39 GBq (Aldahan et al. 2007) of airborne ^{129}I . This event

recorded the highest total airborne ^{129}I emission throughout history when considered together with NFR emissions during that year (Figure 32b).

Baler coral shows peaks in 1987, 1991, and 1995, which are possibly the same NFR and Chernobyl signals but with a 9 to 11-year lag. I propose that this time lag reflect the different pathways taken by ^{129}I to reach the Parola (SCS) and Baler (Pacific Ocean) sites. Atmospheric transport modeling (Figure 11; Reithmeier et al. 2010) shows that ^{129}I enters the SCS through direct deposition from the atmosphere and through deposition on catchment areas that drain to the SCS via surface runoff and rivers. For the Pacific Ocean, on the other hand, ^{129}I is carried by the westerlies and mainly deposited around 50 to 60°N, then subsequently transported by the North Pacific Gyre and North Equatorial Currents to the Baler site (Figure 20a). Based from known ocean current velocities (Maximenko et al. 2009) of the North Pacific Gyre (0.05 m/s) and the North Equatorial Current (0.21 m/s), and the approximate distance around the Pacific Ocean (27,000 km), ^{129}I deposited at 50 to 60°N of the Pacific should take around 10-11 years to reach the Baler site, and this agrees with our observed results. If this explanation is accurate, the Philippines should observe the Fukushima accident ocean signal on its Pacific Ocean side in the year 2021 or 2022.

4.2.4. Post-1996

I found the post-1996 ^{129}I profiles of our coral records surprising. ^{129}I airborne emissions have greatly decreased after 1996 because of improved reprocessing technologies (Figure 32b), which capture airborne ^{129}I and release it as liquid discharges. This decrease is observed in Baler and presumably in the Pacific Ocean but surprisingly, $^{129}\text{I}/^{127}\text{I}$ in Parola in the SCS remained constantly high at ratios of about 22.8 to 38.9 x 10⁻¹² (Figure 32c).

This was also observed by Fan et al. (2016) in a sediment core from Jiaozhou Bay, China (Figure 16c). They associated this trend with the increasing ^{129}I re-emission from the Atlantic and Arctic Oceans, which is caused by the increasing liquid discharges from Sellafield and La Hague NFRs. However, I think the amount of re-emitted ^{129}I is not enough to keep levels as high as those observed in Parola. Re-emitted ^{129}I is estimated to be about 10 GBq/yr from 1996-2004 (Reithmeier et al. 2006), which still results to a decreasing trend in total airborne ^{129}I emission (Figure 32b). Moreover, re-emitted ^{129}I should take atmospheric and oceanic pathways similar to those of the NFR and Chernobyl signals. Consequently, if re-emitted ^{129}I caused the high post-1996 levels in Parola, a time lag rather than opposite signal trends is to be more expected between Parola and Baler. Thus, I suspect some other unknown ^{129}I source is present in the region.

Therefore, I think that it is important to conduct further investigations to ascertain the source of the high ^{129}I levels in post-1996 SCS, especially because of its nuclear security implications. This also demonstrates the possibility of using ^{129}I in corals as evidence for unknown or suspected nuclear activities that may have happened in the past. In addition to this application, if this observed trend continues at present, there is contrastingly high ^{129}I ratio in the SCS and low ^{129}I ratio in the Pacific Ocean. ^{129}I can thus be used as an oceanographic tracer for the complicated SCS circulation and for mass exchanges between the SCS, the Pacific Ocean, the Indonesian throughflow and other bodies of water. I believe that this possible application will be useful for researchers studying these oceanographic processes in the region.

4.3. ^{14}C in corals from the Philippines

$\Delta^{14}\text{C}$ records and locations of corals from Parola and Baler are shown in Figure 33 ($\Delta^{14}\text{C}$ values and errors of Parola and Baler are shown in Appendix B) including published coral records representative of various locations within the Pacific Ocean, namely: within the gyres (North – French Frigate Shoals; South – Rarotonga); in gyre-fed areas (South – Abraham Reef); and in west (Nauru, Tamea) and east (Galapagos) equatorial locations (see Table 3 for coral descriptions). In addition, the Langkai coral record is also shown. Langkai Island is located along the Makassar Strait, Western Indonesia, which is an area influenced by waters from the South China Sea (SCS) during the Boreal Winter or Northwest Monsoon (referred to as only “winter”, from hereon); and by a mixture of waters from the North Equatorial Current (NEC), South Equatorial Current (SEC), and west equatorial upwelling regions (e.g., Banda Sea) during the Boreal Summer or Southeast Monsoon (referred to as only “summer” from hereon). These published $\Delta^{14}\text{C}$ coral records offer interesting comparison to the Parola and Baler corals, which represent ^{14}C variations in the SCS and in southwestern North Pacific gyre-fed location (strongly influenced by NEC waters), respectively.

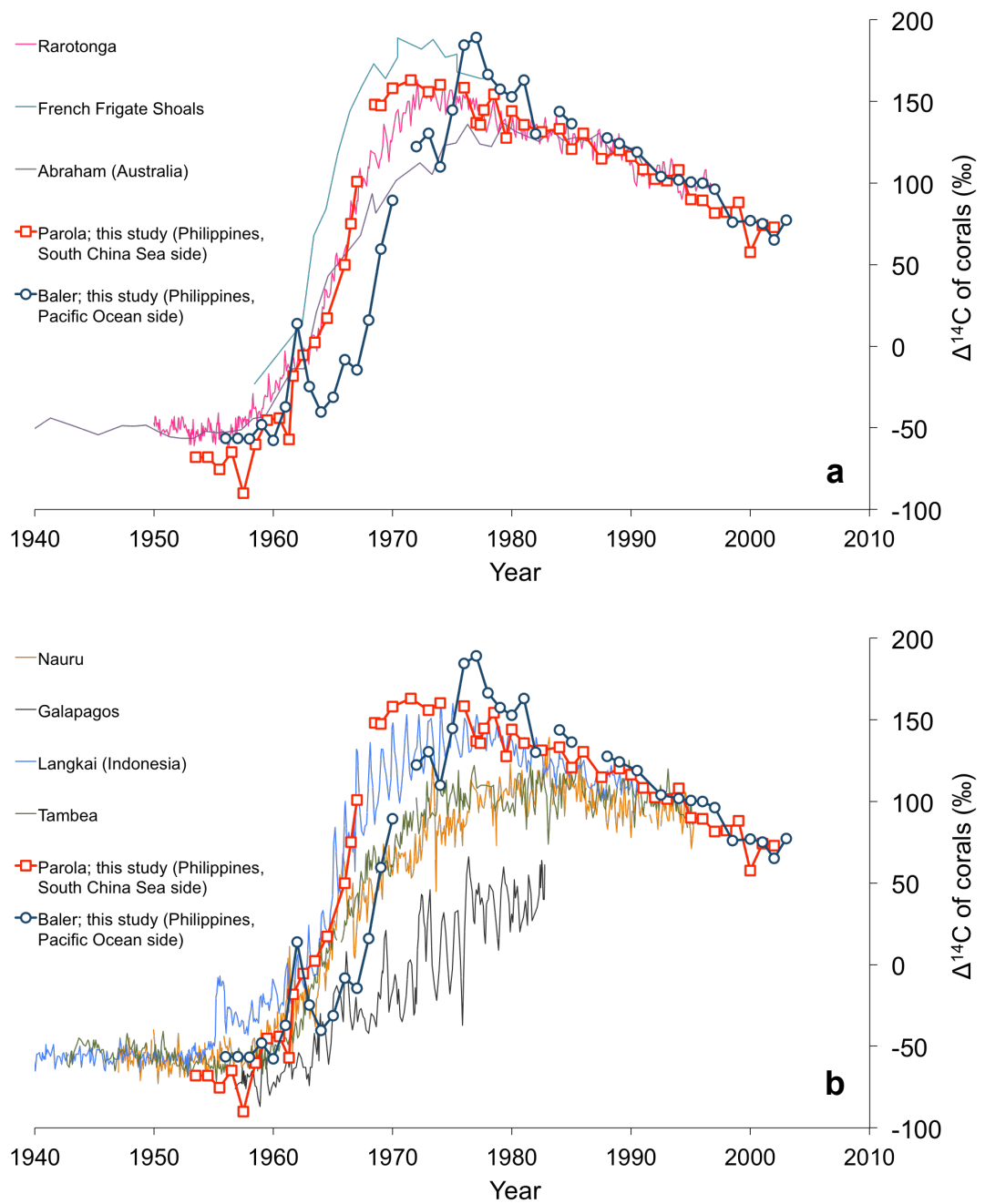


Figure 33. $\Delta^{14}\text{C}$ of the Parola and Baler corals compared with other published coral $\Delta^{14}\text{C}$ records from (a) locations inside and along the gyres and (b) in equatorial regions.

Locations of the corals are shown in Figure 34; Coral record details are shown in Table 3.

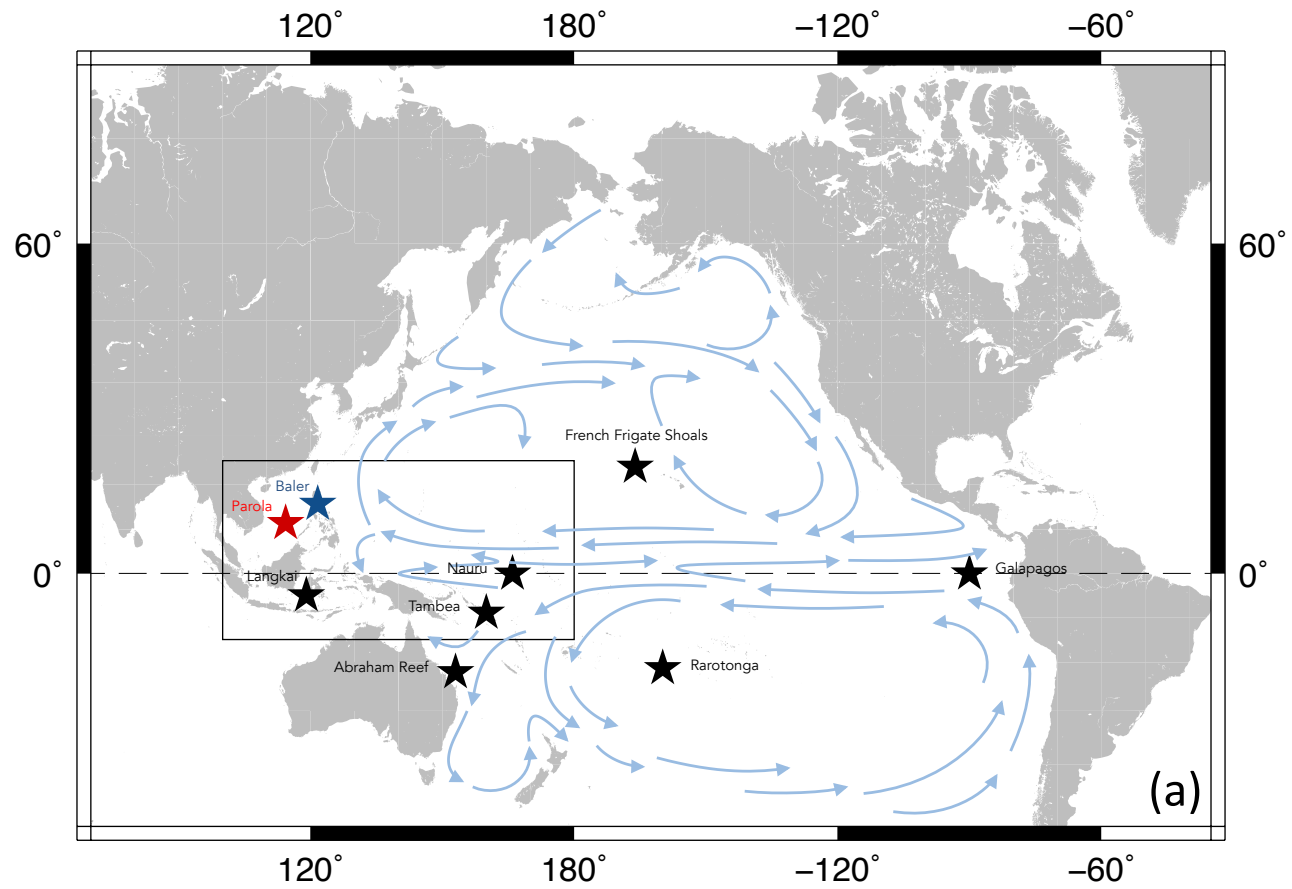


Figure 34a. Locations of ^{14}C coral records and prevailing ocean currents.

(a) Locations of ^{14}C coral records (stars) and ocean currents (blue arrows). Area bounded by the box is shown in (b) and (c), which show the prevailing ocean currents during Boreal winter and summer, respectively.

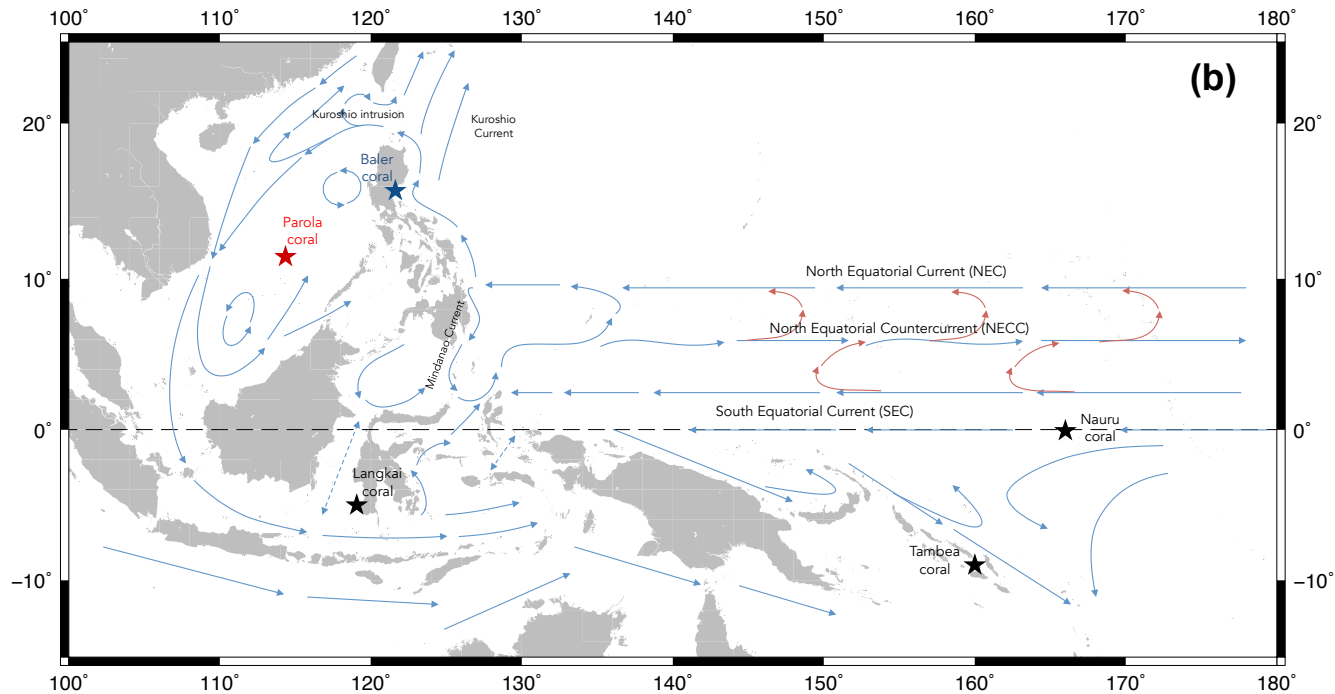


Figure 34b (continued). Locations of ^{14}C coral records and prevailing ocean currents.

(b) During winter, the South China Sea (SCS) has a general counterclockwise circulation, with the Kuroshio Current entering the SCS through the Luzon Strait (northernmost part of the Philippines), and going down to the Indonesian Throughflow (ITF). The North and South Equatorial Currents (NEC and SEC) also appear stronger while the North Equatorial Countercurrent (NECC) appear weaker. As a result, SP intrusion (red arrows) occur far west of the Pacific Ocean. Double headed, dashed arrows mean ocean currents shift quickly back and forth; Ocean currents were based on ESR (2009) and Hu et al. (2000); This map was produced using the Generic Mapping Tools (Wessel & Smith 2013).

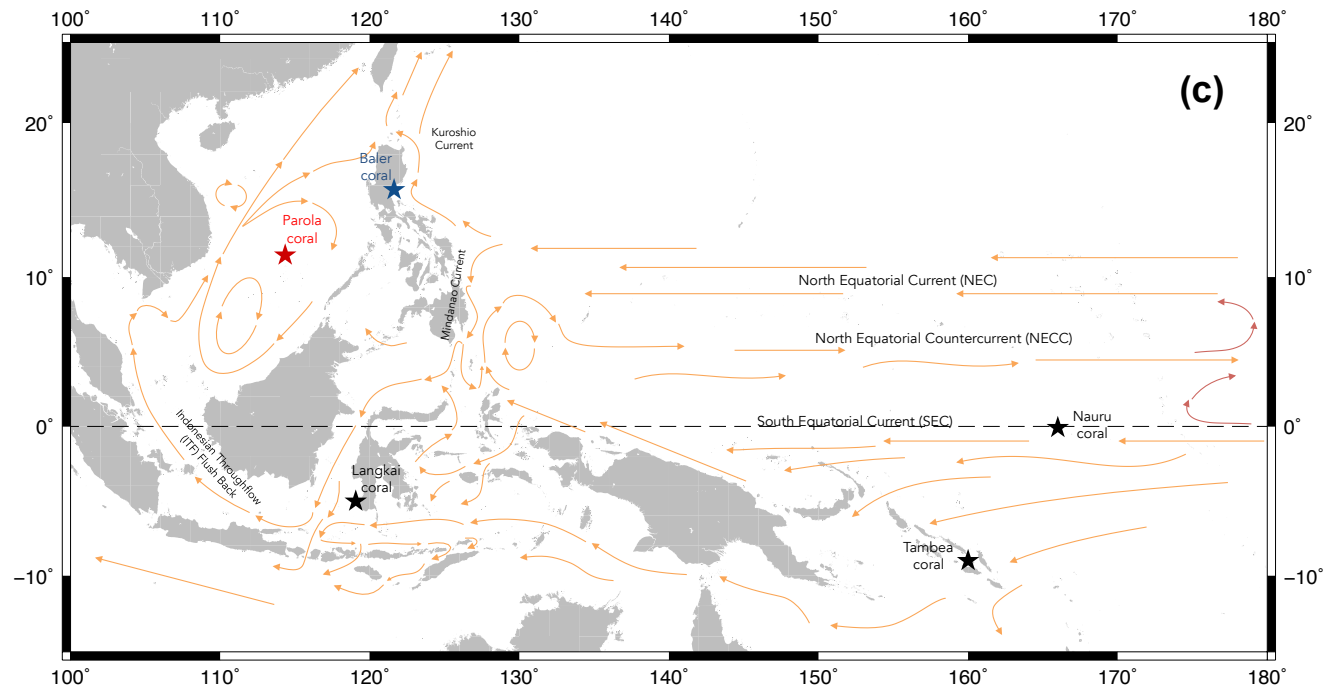


Figure 34c (continued). Locations of ^{14}C coral records and prevailing ocean currents.

(c) During summer, the South China Sea (SCS) has a general clockwise circulation, with the Kuroshio Current is closed off from the SCS in the Luzon Strait (northernmost part of the Philippines), and instead enters the SCS through ITF flush back. The North and South Equatorial Currents (NEC and SEC) appear weaker while the North Equatorial Countercurrent (NECC) appears stronger. As a result, SP intrusion (red arrows) occur far more east of the Pacific Ocean.; Double headed, dashed arrows mean ocean currents shift quickly back and forth; Ocean currents were based on ESR (2009) and Hu et al. (2000); These maps were produced using the Generic Mapping Tools (Wessel & Smith 2013).

Table 3. Details of $\Delta^{14}\text{C}$ coral records from this study and previously published.

Record Name	Country	Latitude, Longitude	Collection Depth (m)	Dates	# of samples / year	References
<i>Parola</i>	Philippines	11°27'N, 114°21'E	3.8	1953-2002	1	This Study
<i>Baler</i>	Philippines	15°46'N, 121°38'E	10	1956-2003	1	This Study
<i>Abraham Reef</i>	Australia	22°06'S, 153°00'E	10 - 12	1635-1991	1 - 2	(Druffel, 1987)
<i>French Frigate Shoals</i>	Line Islands	23°43'N 166°06'W	< 10	1957-1978	1 - 2	(Guilderson et al., 2000)
<i>Galapagos</i>	Ecuador	0°30'S, 90°00'W	1	1957-1983	6 - 11	(Fallon and Guilderson, 2008)
<i>Langkai</i>	Indonesia	5°02'S, 119°04'E	4	1870-1990	6 - 8	(Druffel and Griffin, 2004)
<i>Nauru</i>	Nauru	0°05'S, 166°00'E	14	1947-1995	12	(Guilderson et al., 1998)
<i>Rarotonga</i>	Cook Islands	21°14'S, 159°49'W	18	1950-1997	8 - 11	(Guilderson and Schrag, 1998)
<i>Tambea</i>	Solomon Islands	9°S, 160°E	14	1942-1995	3-9	(Guilderson et al., 2004)

All records (aside from this study) are available at the World Data Center for Paleoclimatology website:
(<http://www.ncdc.noaa.gov/paleo/corals.html>)

4.3.1. Parola

$\Delta^{14}\text{C}$ bomb peak of the Parola coral is characterized by an increase at around 1956-1958 from about -65‰ to a peak value of 163‰ in 1972. After 1972, we observe a steady decrease with a rate of about 3‰ per year. This trend is largely similar to that observed in Rarotonga and French Frigate Shoals (FFS), which both peak at around 1972 albeit FFS having higher $\Delta^{14}\text{C}$ levels (which demonstrates that ^{14}C deposition is stronger in higher latitudes). A possible explanation for the observed similarities is that like Rarotonga and FFS, Parola is situated in the middle of the SCS circulation pattern (Figure 34). Furthermore, SCS is a semi-enclosed body of water and its mixed layer depth is shallow yearlong, only varying between 10-50 m (de Boyer Montégut et al. 2004). All these factors enhance the surface water residence time in the vicinity of Parola, enhancing atmosphere-to-surface ocean concentration of ^{14}C , and thus, possibly resulting to the rapid rise and peaking of $\Delta^{14}\text{C}$ in Parola.

It also interesting to compare the Parola and Langkai records because source waters of these two locations are possibly similar. As illustrated in Figure 34, ^{14}C of the Parola record, aside from the native signal from the atmosphere, may come from oceanic transport by the Kuroshio Current intrusion passing through the Luzon Strait in winter and from the “flush back” of the Indonesian Throughflow during summer (referred to as ITF flush back from hereon; composed of a mixture of NEC, upper part of SEC, and possibly west equatorial upwelling waters). The Langkai record receives a large portion waters coming from the SCS in the winter and similarly, the ITF flush back in the summer plus some waters from the lower part of the SEC and upwelling from the Banda Sea (Fallon & Guilderson 2008). These may explain why Parola and Langkai show similar trends. Higher contributions from the ITF flush back, lower SEC, and upwelled Banda Sea waters in Langkai may also explain why its ^{14}C bomb

curve peaks later at around 1977. Interestingly, Langkai $\Delta^{14}\text{C}$ values are constantly in between the Parola and Nauru records, which represent waters from the SCS and ITF flush back waters, respectively. Moreover, the amplitude of the $\Delta^{14}\text{C}$ oscillation of the Langkai coral appears to be proportional to the difference of $\Delta^{14}\text{C}$ in Parola and Nauru, which is most pronounced in the region between 1966-1980. This agrees with the explanation of Fallon & Guilderson (2008), which attributes this oscillation in Langkai to the “see-saw” of water contributions from the SCS and the ITF flush back to the Makassar Strait, associated with seasonal/monsoonal cycles.

4.3.2. Small pre-bomb peak

One interesting discrepancy between the Parola and Langkai corals, is a small peak observed in Langkai at around 1955, which is not observed in the Parola coral. Fallon & Guilderson (2008) associates this peak to the 1954 bomb signal, transported westward from the US bomb test site by ocean currents particularly the NEC, which eventually enters the Makassar Strait (Figure 34). As discussed in the previous paragraph, the same NEC waters that goes through Makassar Strait and the Indonesian Throughflow during summer, also enters into the SCS through the ITF flush back. Furthermore, the NEC also enters the SCS by Kuroshio Current intrusion through the Luzon Strait during winter (Hu et al. 2000; Fallon & Guilderson 2008). Although the effects of the ITF flush back and Kuroshio intrusion may be minimal in the Parola coral since it is located in the middle of the SCS circulation pattern, it may be reasonable to expect that this 1955 signal in Langkai would also be recorded in Parola, even weakly. However, ^{14}C in Parola consistently show natural $\Delta^{14}\text{C}$ levels ($\sim -70\text{‰}$) in years 1955-56 and only a slight peak (-45‰) in 1959. Also interesting is the fact that ^{129}I levels in Parola show strong signals associated with the 1954 as well as

1958 US bomb tests (Figure 35) albeit we attribute this to a localized atmospheric signal (instead of ocean-transported signal), as discussed in Section 4.2.2. Given these, unless ^{129}I exclusively took the atmospheric route and ^{14}C exclusively took the oceanic route to reach Makassar Strait but did not affect the SCS, these results indicate that the 1954 and 1959 bomb tests had minimal effect on coral $\Delta^{14}\text{C}$ in the region around the Philippines during these years. Thus, the small pre-bomb peak discrepancy between Parola and Langkai is currently puzzling and difficult to explain.

A peak similar to the small pre-bomb signal is also present in Baler. However, while the Langkai and Japan corals record it in 1955 or 1956 (Fallon & Guilderson 2008; Konishi et al. 1981), the Baler coral records this pre-bomb peak in 1962. Interestingly, this peak coincides with the highest ^{129}I bomb signal observed in the Baler record, which also coincides to an almost identical ^{129}I peak in Parola (Figure 35). It is also notable that, the Baler ^{14}C pre-bomb peak (1962, 13.8‰) coincides with the sudden increase in $\Delta^{14}\text{C}$ in Parola (from -57.1‰ in 1961 to -5.5‰ in 1962.5) as well as with a peak found around the onset of $\Delta^{14}\text{C}$ increase in Nauru (1961.4, 11‰). As an alternative explanation, I propose two possible mechanisms that may result to this observed trend: (1) a small portion of the bomb-produced ^{14}C may have been formed in a form other than CO_2 that has a significantly quicker atmospheric lifetime (referred to as “quick input” from hereon). For example, other species of carbon in the atmosphere such as methane and the carbonaceous aerosol “black carbon” have much shorter atmospheric lifetimes of 12 years and about 1 week, respectively (Solomon et al. 2007; Bauer et al. 2013). This possibly caused the quick increase in $\Delta^{14}\text{C}$ Parola and the small pre-bomb peak in Baler. The difference, however, is that $\Delta^{14}\text{C}$ went back down after the “quick input” in Baler (thus forming the peak) and I propose that

this is because of (2) the intrusion of South Pacific waters to the North Equatorial Current (referred to as “SP intrusion” from hereon).

Ocean circulation data based from satellite altimeter and scatterometer data (Ocean Surface Current Analyses – Real time or OSCAR; ESR 2009), show that some South Pacific waters from the South Equatorial Current, can intrude into the North Equatorial Countercurrent (NECC) and eventually into the North Equatorial Current (NEC), which is the source water for the Baler site (Figure 34). Given that there is about 2-year delay in atmospheric ^{14}C peak between northern and southern hemisphere (Figure 17; Peng et al. 1998), it is reasonable to expect that $\Delta^{14}\text{C}$ of South Pacific waters are considerably lower than that of the North Pacific during the onset of the bomb curve. Therefore, while the “quick input” suddenly increased $\Delta^{14}\text{C}$ in Baler, “SP intrusion” may have pushed $\Delta^{14}\text{C}$ back down. However, as with the discrepancy of small pre-bomb peak between Langkai and Parola, it appears that the effect of SP intrusion is barely visible in Parola $\Delta^{14}\text{C}$ (as shown by the absence of a peak). The effect of SP intrusion may have been masked by the increase in $\Delta^{14}\text{C}$, and may be revealed with higher time resolution measurements. Nevertheless, this demonstrates that the Parola coral may indeed be isolated to a certain degree from the effect of Pacific waters, which enter the SCS through ITF flush and Kuroshio intrusion.

We would like to emphasize that the age model of the Baler record, which was based on annual band counting, may be interpreted to have relatively higher uncertainties and that this maybe the cause of the observed discrepancies. However, we believe that the ^{129}I records of both Baler and Parola add considerable basis to support the age model of Baler and its resulting interpretations (Figure 35): as discussed in Section 4.2.2, there is considerable evidence that suggests that ^{129}I

signals mainly come from the atmosphere. Moreover, comparison of nuclear bomb test records and the magnitudes of the ^{129}I peaks, as supported by the corrected age model of Parola (based on annual band counting and agreement between coral Sr/Ca and SST; see Section 3.1.2), strongly indicate that the highest peak in the coral ^{129}I records happen in year 1962. This peak is expected to be ubiquitous in the northern hemisphere, only differing in magnitude between different latitudes (UNSCEAR 2000; Reithmeier et al. 2006). It is thus reasonable to expect that the 1962 ^{129}I signal will be concurrent in the Parola and Baler records. Given that ^{129}I and ^{14}C were measured in the same samples, ^{14}C records may also be treated with the same degree of chronological certainty. In addition, the timing difference of the small peak between Baler and Langkai is around 7 to 8 years, which is arguably too large to be attributed to errors in annual counting. Adjusting the Baler age model earlier by 7 years will make $\Delta^{14}\text{C}$ bomb peak of Baler equivalent or even earlier than FFS, which is unlikely since atmospheric ^{14}C concentration and deposition is higher in mid-latitudes. Adjusting by 7 years will also break the agreement of the observed ^{129}I signals between Parola and Baler, which will make interpretations even more problematic. Given these, we decided to keep the Baler age model as is, but still highlight the need for further analyses (e.g., Sr/Ca or ^{18}O) to increase the certainty coral age models and the discussion of their results.

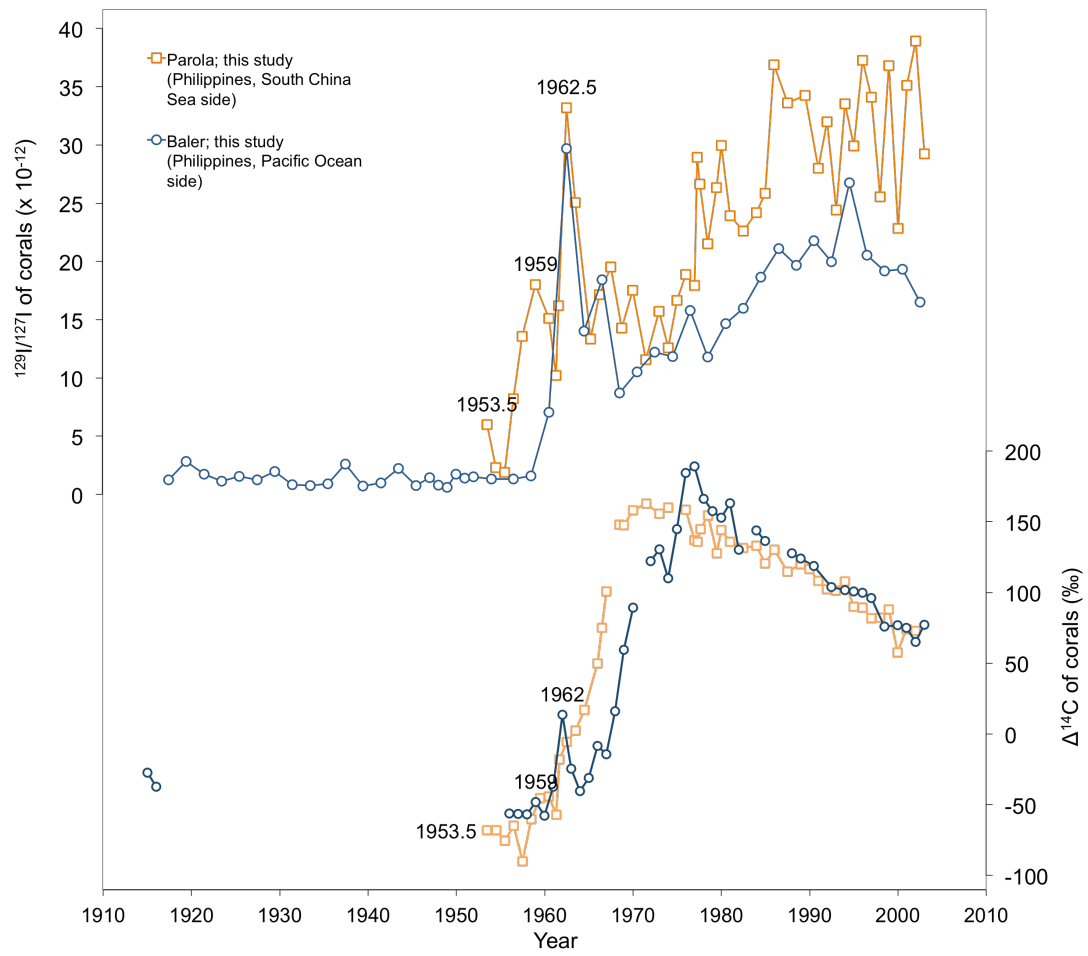


Figure 35. $^{129}\text{I}/^{127}\text{I}$ ($\times 10^{-12}$) and $\Delta^{14}\text{C}$ (‰) of corals from Parola and Baler.

4.3.3. Baler

After the small pre-bomb peak, $\Delta^{14}\text{C}$ of the Baler coral starts to increase from -40.3‰ in 1964 to a peak value of 189.3‰ in 1977. Subsequently, we observe a steady decrease after 1977 with a slightly faster rate of about 4‰ per year. Although both Parola and Baler $\Delta^{14}\text{C}$ appear to start their increase at the same time as well as have almost equal rates of increase, Baler $\Delta^{14}\text{C}$ considerably went back down after the pre-bomb peak, causing it to have consistently lower $\Delta^{14}\text{C}$ (by about 50-100‰) during the whole period of increase until 1976. It is also interesting to note that this is also the case for ^{129}I where Parola consistently displayed higher ratios than Baler (see Section 4.2). This trend demonstrates how different the oceanic regimes in the east and west sides of the Philippines. As discussed in the previous section, the delayed increase of the Baler record may be the result of SP intrusion. In addition, the mixture of the native ^{14}C from the atmosphere (as seen in Parola), high ^{14}C North Pacific subtropical waters (as seen in FFS), and the upwelled, low ^{14}C east equatorial waters that feeds the NEC (specifically the Central American upwelling region; Figure 36), which in turn is the primary source water of the Baler coral, may have contributed to this delay. Being directly inline with the NEC may also explain why $\Delta^{14}\text{C}$ curve maximum of the Baler record in 1977 is roughly concurrent with that of Langkai and Abraham Reef, which are also gyre-fed locations in the western part of the Pacific Ocean.

Another interesting aspect of Baler is how its specific signals coincide (given the age model uncertainty) with episodes of El niño/La niña of the El Niño Southern Oscillation (ENSO; Figure 37), particularly in years 1959, 1966, 1973/74, 1992, and 1998 (Baler had missing data for El niño years 1983 and 1987). $\Delta^{14}\text{C}$ of the Baler coral had spikes of about 6‰ to 10‰ during El niño years 1959 and 1966, and an even stronger difference of about 20‰ for the El niño year 1973, which was followed

by a La niña in 1974. Conversely, the effect of the ENSO on the Baler $\Delta^{14}\text{C}$ then appear to have weakened in years 1992 and 1998.

This trend may be explained by effect of ENSO on the NEC, particularly its bifurcation latitude. The NEC, upon hitting the Philippine archipelago, splits or bifurcates into the Kuroshio Current to the north, and the Mindanao Current to the south (Figure 34). The bifurcation latitude of the NEC normally shifts northward during the winter and southward during the summer (Wang & Hu 2006). As the bifurcation shifts northward, the Kuroshio weakens and the Mindanao strengthens, and vice versa (Yang et al. 2013). This phenomenon, according to high-resolution general circulation models (Kim et al. 2004) and satellite altimetry analyses (Wang & Hu 2006), is even strengthened by ENSO cycles with the bifurcation latitude moving further northward during El niño and southward during La niña. Moreover, the North Equatorial Countercurrent (NECC) also strengthens during El niño (Wang & Wu 2013). This is further supported by surveys conducted by Kashino et al. (2009), showing that the Kuroshio Current weakens during El niño and strengthens during La niña. In addition, Gordon et al. (2014) found that there are larger contributions of northern subtropical waters in the region of Baler when the bifurcation shifts northward (and vice versa), possibly because of increased contribution from the Kuroshio recirculation gyre (Figure 38).

Given these, it is possible that during El niño years, larger contributions from higher ^{14}C (as seen in FFS) northern subtropical waters affect the Baler site and increase the ^{14}C concentration. In addition to this, I propose that SP intrusion also decreases with the northward shift of the NEC and the strengthening of the NECC. Subsequently, conditions go back to normal when the El niño episode ends, resulting to a slight drop in $\Delta^{14}\text{C}$. In the case of the 1973 El niño, it was followed by a La niña

in 1974, which reversed the effect, further increasing contributions of the NEC to the Baler site and decreasing that of the northern subtropical waters, resulting to $\Delta^{14}\text{C}$ that is lower than normal conditions. This may explain the bigger $\Delta^{14}\text{C}$ difference in years 1973/74. Interestingly, peaks that coincide with the ENSO cycles are also observed in the Nauru coral, particularly in 1966, 1973/74, and even in 1983. This is probably because of the SEC latitude also shifts southward during El niño years (Guilderson et al. 2004) and the Nauru site gets more contribution to the higher ^{14}C waters from the North Pacific, either from the SCS or the NEC, through the strengthened NECC (Figure 34).

Another interesting feature of Baler $\Delta^{14}\text{C}$ is the sudden shift observed in 1976. While there were no El niño/La niña episodes, 1976 marks a negative-to-positive phase shift of the Pacific Decadal Oscillation (PDO; Figure 39). Galapagos coral also records an abrupt ^{14}C shift in during this year, which Guilderson & Schrag (1998) attributes to a change in the source of upwelling water in this location. The Baler record also shows a 74.6‰ $\Delta^{14}\text{C}$ jump during this year, from 110‰ in 1974 to 184.6‰ in 1976. In the case of Baler, however, this event may also be explained by migration of the NEC bifurcation latitude.

The positive phase of PDO is often described as a “prolonged El Niño” and is characterized by an abrupt change in sea surface temperature (SST) anomalies to a hotter-than-normal east equatorial Pacific and a colder-than-normal northwestern Pacific (Figure 40; Mantua et al. 1997). In fact, Gordon et al. (2014) proposes that a positive PDO affects the NEC bifurcation latitude similar to El niño and vice versa. Therefore, the 1976 $\Delta^{14}\text{C}$ shift in Baler may have been caused by a combination of higher NEC bifurcation latitude that brings in more subtropical waters to the Baler site as well as decreased SP intrusion to the NEC.

Interestingly, however, while El Niño years are associated to weaker upwelling and a consequent lower fish population in the eastern Pacific, a particular upwelling spot in Central America (Figure 36; also marked in Figure 40) appears to get colder with a more positive PDO, possibly indicating a contrastingly stronger upwelling in this area which will lower $\Delta^{14}\text{C}$ in the region. This same upwelling spot is the starting point of the NEC, which feeds the waters of the Baler site. It would thus be interesting to study the dynamics of these two processes in connection with the 1976 shift in Baler $\Delta^{14}\text{C}$.

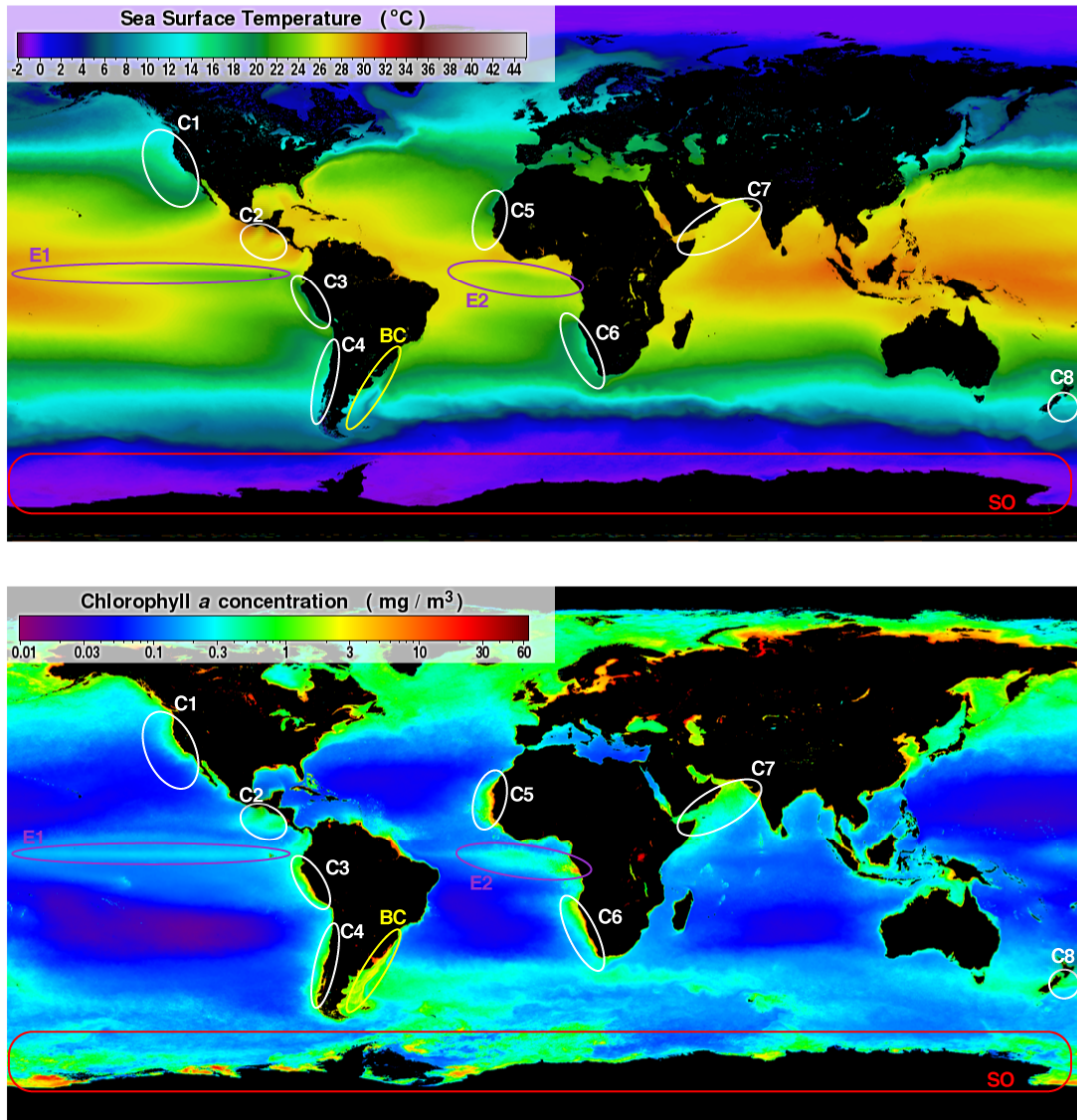


Figure 36. Upwelling regions.

Global map of sea surface temperature (top) and phytoplankton chlorophyll concentration (bottom) from the MODIS sensor on NASA's Aqua satellite. Upwelling regions are marked by colder-than-normal waters and high concentration of Chlorophyll. Pacific Central American upwelling region is marked by C2. From <http://www.seos-project.eu/>.

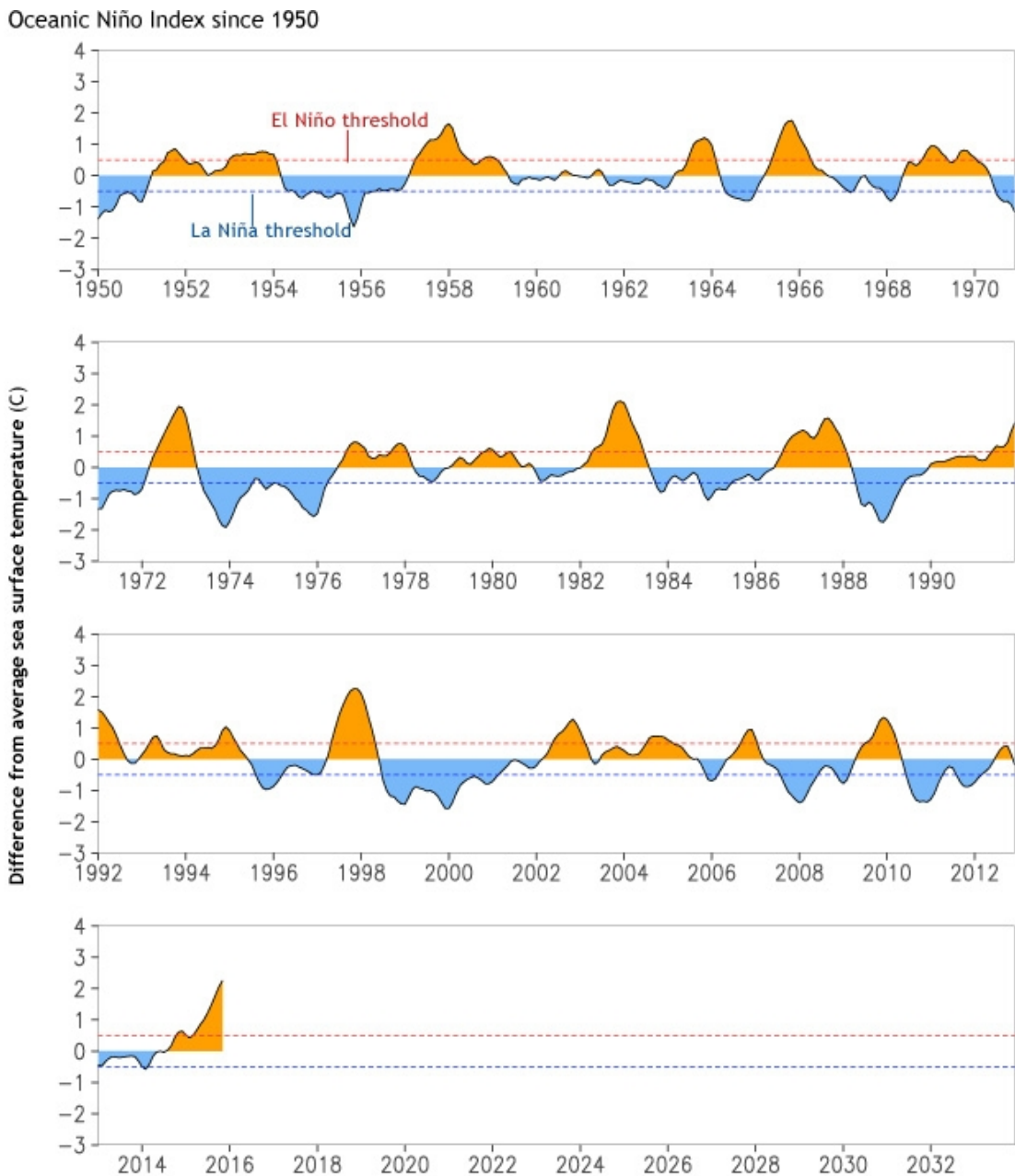


Figure 37. El Niño Southern Oscillation (ENSO) index.

Running 3-month average sea surface temperature anomalies in the Niño 3.4 or ONI region (i.e., a region in the Pacific equator that is most affected by ENSO changes), taken from NOAA's Extended Reconstructed Sea Surface Temperature dataset (ERSST; Smith et al. 2008). El Niño and La Niña occur when the ONI SST exceeds the corresponding thresholds. From <https://www.climate.gov/>.

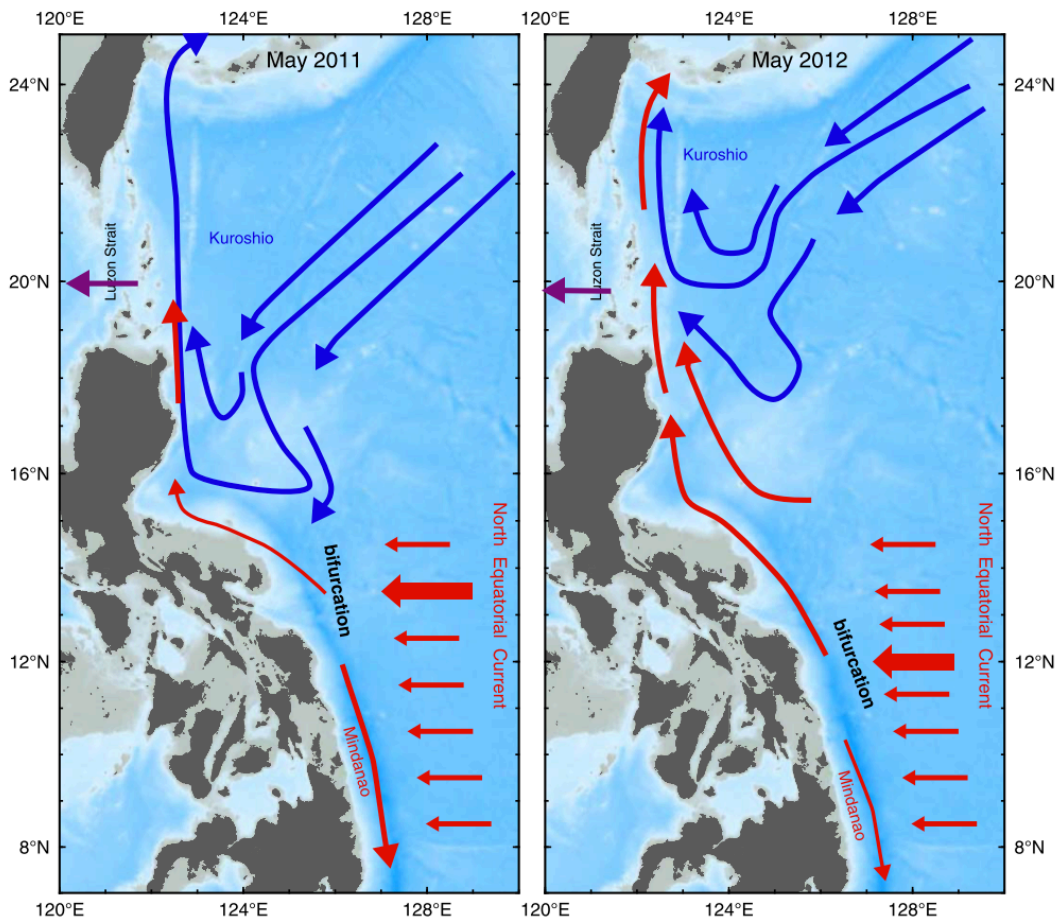


Figure 38. Schematic diagram of the migration of the latitude of bifurcation of the North Equatorial Current (NEC).

(Left) El Niño and the positive phase of the PDO causes the NEC bifurcation latitude to shift northwards, resulting to increased influence of northern subtropical waters to the Baler site through the Kuroshio recirculation gyre as well as strengthening of the Mindanao current and weakening of the Kuroshio current; (Right) during La Niña and the negative phase of the PDO, the opposite trend occurs. From Gordon et al. (2014).

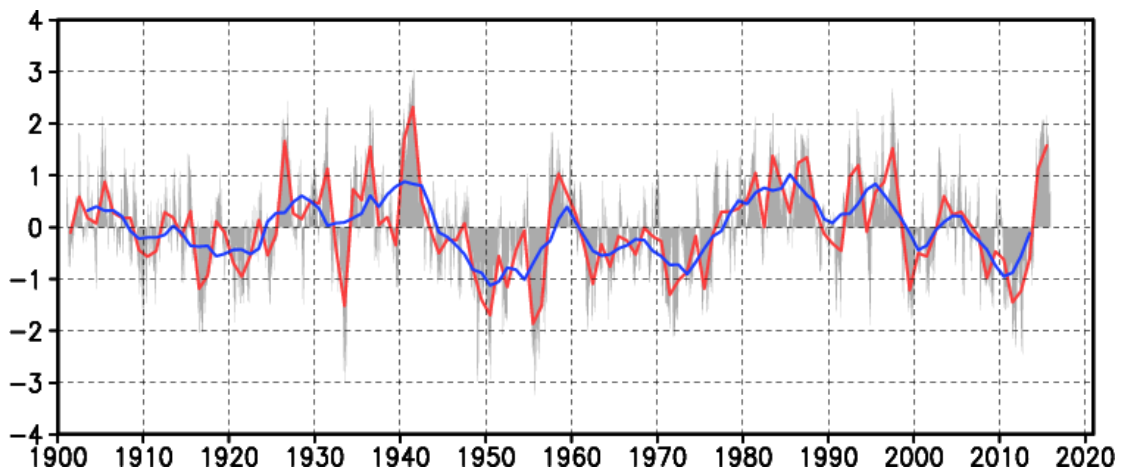


Figure 39. Pacific Decadal Oscillation (PDO) index.

Gray bars represent monthly values, red line represents annual mean values, and the blue line represents five-year running mean values. From <http://ds.data.jma.go.jp/>.

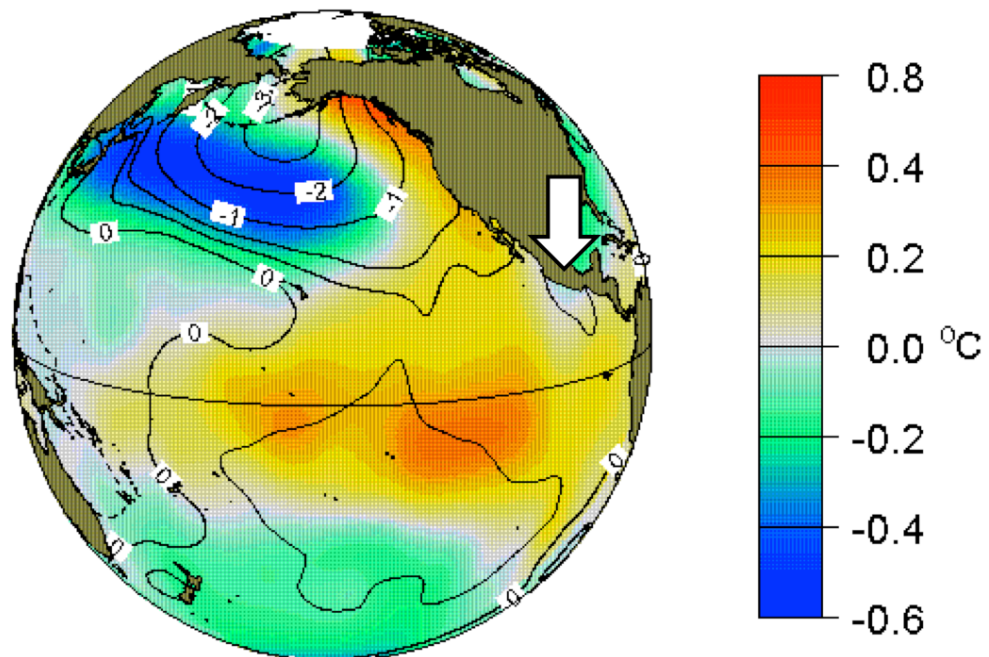


Figure 40. PDO index regressed with sea surface temperature (SST) and sea level pressure (SLP).

A positive PDO index or phase would thus mean hotter-than-normal east equatorial Pacific and a colder-than-normal northwestern Pacific. The upwelling region in Central America is marked with a white arrow. From Mantua et al. (1997).

4.4. Box mixing model

4.4.1. ^{14}C and ^{129}I trends based on atmospheric lifetime

The first factor that I wanted to analyze using the developed box mixing model was the atmospheric lifetime of the radionuclides and its effect on the resulting trend in the ocean box. Ocean boxes Parola and Baler (box 1) is presumed to reflect the trends observed in the coral archives taken from these location. As mentioned in Sections 2.1.2.1, 2.2, and 2.4, Aboveground nuclear bomb tests produced and released massive amounts of radionuclides in the atmosphere including ^{14}C and ^{129}I . For ^{14}C (which exists mostly as CO_2), the Intergovernmental Panel on Climate Change (IPCC) and the Bern Carbon Cycle Model estimate that 50% of a pulse of CO_2 injected to the atmosphere will be removed within 30 years, a further 30% will be removed within a few centuries, and the remaining 20% may remain in the atmosphere for thousands of years (Denman et al. 2007; Joos et al. 2001). ^{129}I , on the other hand, is estimated to stay in the troposphere and stratosphere for about 2-4 weeks and 1-2 years, respectively (Moran et al. 1999; UNSCEAR 2000). I believe that this large difference in atmospheric lifetimes is the main cause of discrepancy between the observed coral ^{14}C and ^{129}I trends.

To analyze this, the value of k_{A-O} was adjusted while keeping other variables constant (I^0 , a_y , k_{out} , k_{adv}) and first removing the effects of South Pacific intrusion, “quick deposit”, Kuroshio recirculation gyre, and upwelling for simplicity ($\chi_{intrusion}$, χ_{quick} , k_{recirc} , and k_{upw} are all set to zero). For ^{14}C , I found that the shape of the coral ^{14}C bomb curve can be reproduced using an atmospheric lifetime of 300 years (Figure 41; $k_{A-O} = 2.557 \times 10^{-4}$). This k_{A-O} value is acceptable given the definition of CO_2 atmospheric lifetime provided in the previous paragraph. The peak in the Parola and Baler ocean boxes happened in $t = 1973.9$ and 1978.0 , respectively. This is consistent

with actual measurements wherein the ^{14}C peak in the Parola and Baler corals occurred at around 1972 and 1976/77, respectively (Figure 35a). Peaks of the curves of both Baler and Parola boxes are also delayed by 10 and 14 years compared to the time of radionuclide input to the atmospheric component, which is $t = 1962.0$. Moreover, these results show that variations in a_y (i.e., deposition variation with latitude) and the advection around boxes 1-25 (i.e., North Pacific Gyre circulation) were enough to delay the peak of the Baler box (box 1) by about 4 years compared to that in Parola, which, in contrast, is supposed to be located in the middle of the circulation of the semi-enclosed South China Sea.

For ^{129}I , an atmospheric lifetime of 2 years ($k_{A-O} = 3.836 \times 10^{-2}$) was used. The peak in the Baler and Parola boxes had roughly the same magnitude and occurred almost simultaneously at $t = 1963.3$ and 1963.1 , respectively, which is delayed by only 1 year from the time of radionuclide input (Figure 41b). This is also consistent with actual measurements wherein the ^{129}I peak in the Parola and Baler corals occurred both around 1962/63. These results quantitatively demonstrate what we proposed in Section 4.2.2. – that ^{129}I would be a better coral time marker than ^{14}C , which as shown in the previous paragraph, had varied peak timing and shape as an effect of ocean processes. This is because of the large difference in atmospheric lifetimes, with ^{129}I being much shorter and this results in a sharper peak that is more uniform in shape and timing and is less affected by oceanic processes.

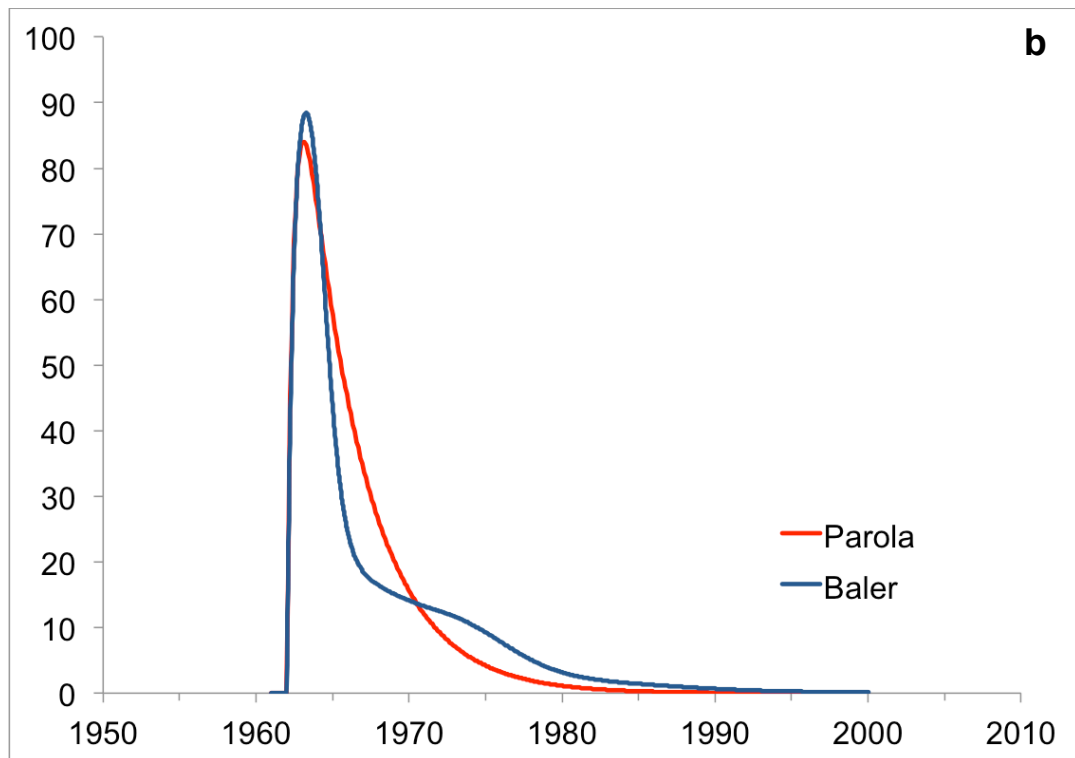
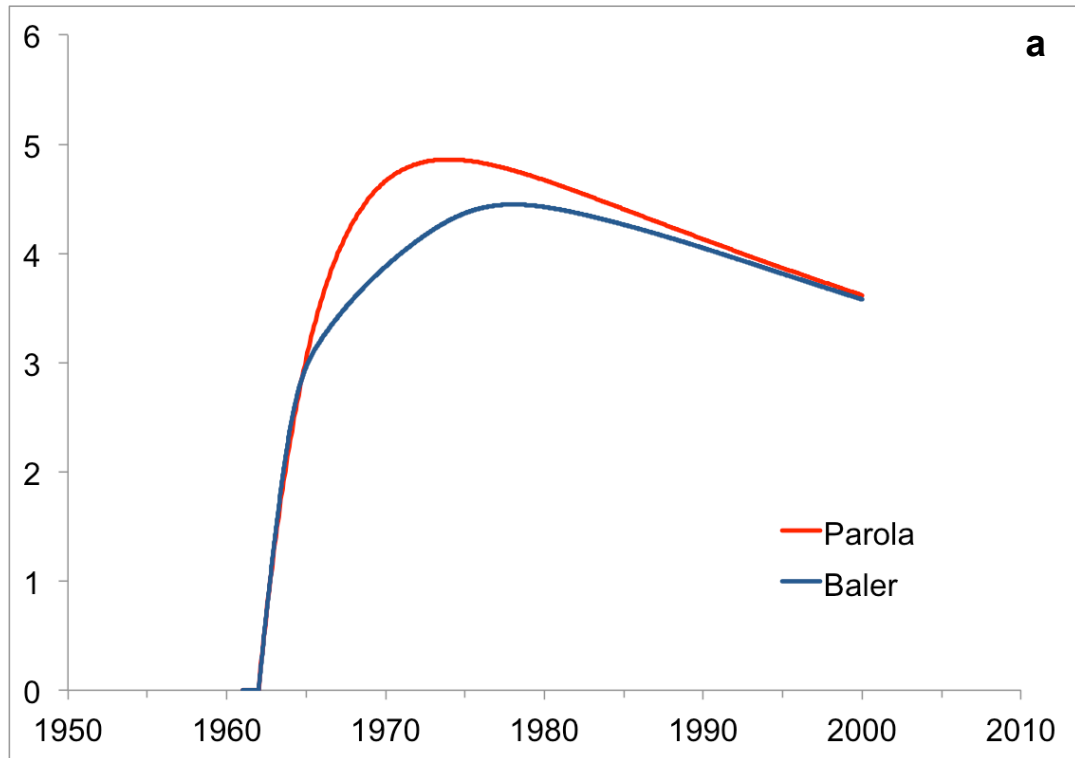


Figure 41. Coral (a) ^{14}C and (b) ^{129}I bomb curve for Parola and Baler reproduced by the box mixing model.

Atmospheric lifetimes for ^{14}C and ^{129}I are 300 ($k_{A-O} = 2.557 \times 10^{-4}$) and 2 years ($k_{A-O} = 3.836 \times 10^{-2}$), respectively; all other processes ($\chi_{\text{intrusion}}$, χ_{quick} , k_{recirc} , and k_{upw}) are zero.

4.4.2. Specific coral ^{14}C trends

4.4.2.1. Intrusion of South Pacific waters

Although variations in a_y and advection around boxes 1-25 were able to explain the delay in of the peak of the coral ^{14}C curve, it was not enough to explain the apparent delay in the onset of increase in Baler (Figure 33). Actual measurements of Baler coral show consistently lower $\Delta^{14}\text{C}$ (by about 50-100‰) during the whole period of increase until 1976 compared to Parola. As described in See Section 4.3.2. and 4.3.3, one possible cause of this delay is the intrusion of South Pacific waters to the North Equatorial Current (referred to as “SP intrusion”). Though only estimated visually (ESR 2009; OSCAR visualization seen in: <https://svs.gsfc.nasa.gov/cgi-bin/details.cgi?aid=3958>), SP intrusion appears to be most apparent in locations corresponding to boxes 23-21, but may extend even to box 15, while mostly the same NEC waters appear to be only recirculated by the NECC in boxes 1, 24, and 25.

To roughly simulate this effect another isolated atmosphere-ocean box pair (box *SP*) was first created for the South Pacific waters. Box *SP* is similar to the Parola box with the only differences being the radionuclide input was 2 years late, its magnitude 75% of the original, and its k_{out} being slightly different such that even with a smaller input magnitude, the O_{sp} will be roughly equal with the northern hemispheric values in the later years (purple line in Figure 42). These are based on atmospheric ^{14}C trends (Figure 17), which show about 2-year delay in the southern hemisphere, likely caused by the restricted atmospheric exchange between the northern and southern hemispheres estimated to be also about 2 years (UNSCEAR 2000; Peng et al. 1998). With continued exchange and no additional input, ^{14}C values eventually equalize between the northern and southern hemisphere in the later years. The South Pacific

ocean box (O_{sp}) then intrudes to ocean boxes 21, 22, and 23 through Equation 10 (See Section 3.1.5), with $\chi_{intrusion}$ values of 0.05, 0.1, and 0.15, respectively.

Figure 42 shows that this effectively delays the onset of the ^{14}C curve albeit the irregular feature around 1963. This is probably because our model only roughly estimates the effect of SP intrusion and is not accurately spread out across the NEC. The resulting effect when SP intrusion is more spread out across the NEC is discussed in Section 4.4.3. Nonetheless, our results demonstrate the possibility of SP intrusion delaying the ^{14}C bomb curve in the Baler site versus the almost purely atmospheric ^{14}C origin of Parola, which is within the semi-enclosed South China Sea.

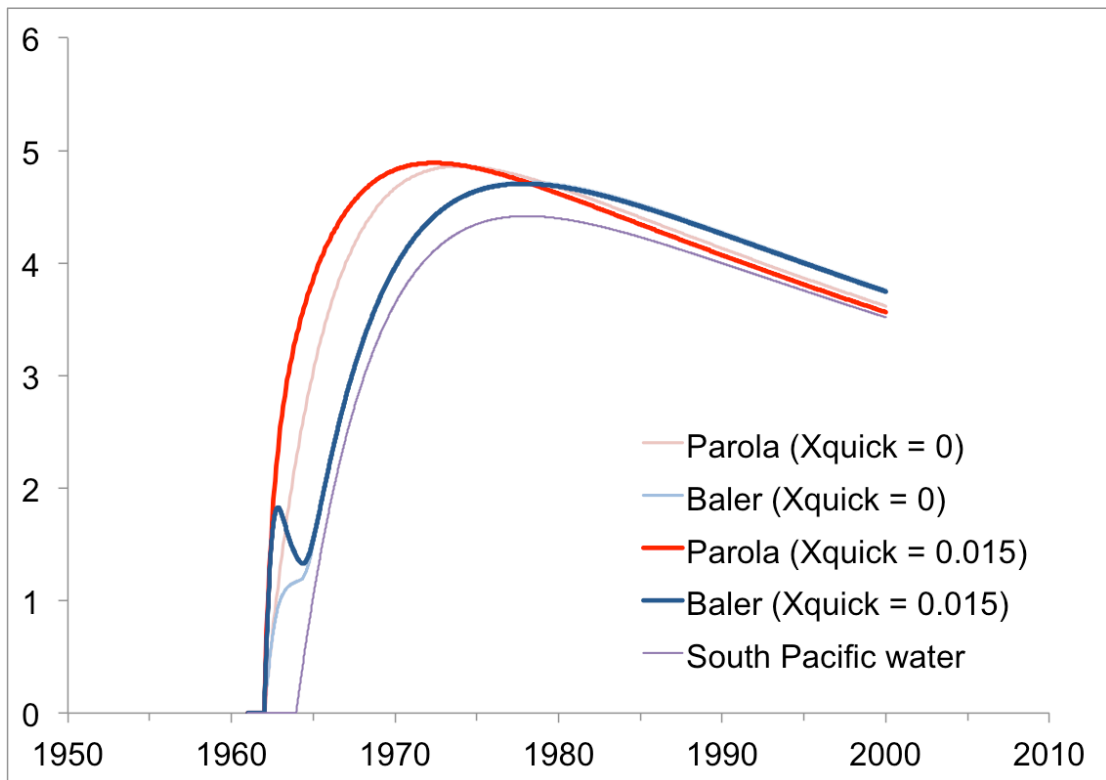


Figure 42. Simulated ^{14}C and bomb curve for Parola and Baler with (dark lines) SP intrusion effect; (light lines) SP intrusion with quick input effect.

Atmospheric lifetime for ^{14}C is 300 years ($k_{A-O} = 2.557 \times 10^{-4}$); $\chi_{intrusion}$ values are 0.05, 0.1, and 0.15 for boxes 21-23, respectively; also shown is the variation of the South Pacific ocean box, O_{sp} (purple line).

4.4.2.2. *Quick input*

Another feature in the measured coral ^{14}C record is the small pre-bomb peak observed in Baler in 1962 (Figure 33). In Section 4.3.2, I proposed that this was caused by a small portion of the bomb-produced ^{14}C , being in a form other than CO_2 that has a significantly quicker atmospheric lifetime. For example, other species of carbon in the atmosphere such as methane and the carbonaceous aerosol “black carbon” have much shorter atmospheric lifetimes of 12 years and about 1 week, respectively (Solomon et al. 2007; Bauer et al. 2013). In the box mixing model, this portion (χ_{quick}) was set to 1.5% and was set to have an atmospheric lifetime similar to ^{129}I (2 years, $k_{A-O} = 3.836 \times 10^{-2}$). The result is showed in Figure 42 and demonstrates that even such a small χ_{quick} is enough to roughly reproduce the small pre-bomb peak in Baler (and not in Parola). This small peak is made apparent in Baler by the negative effect brought by the SP intrusion, which pushes the ^{14}C back down after the introduction of the “quick input”. Using a quicker atmospheric lifetime produces an even sharper small peak. Furthermore, the peak of the bomb curves in the Baler and Parola boxes were pushed back earlier to 1972.4 and 1977.9. This made the modeled curves closer to the measured trends, which peaked at around 1972 and 1976/77, respectively. Again, the modeled small pre-bomb peak looks does not perfectly look similar the actual measured peak probably because our model only roughly estimates the effect of SP intrusion. The effect of a more accurate SP intrusion modeling on the small pre-bomb peak is also discussed in Section 4.4.3.

4.4.2.3. *PDO effect (upwelling and Kuroshio recirculation)*

Another major factor that I wanted to consider in the box mixing model is the effect of the 1976 negative-to-positive phase shift of the Pacific Decadal Oscillation

(PDO). ^{14}C measurements of the Baler coral show a 74.6‰ jump during this year, from 110‰ in 1974 to 184.6‰ in 1976, while no strong effect was observed in Parola (Figure 33). A Galapagos coral, located in eastern equatorial Pacific, also shows a similar jump in ^{14}C (Guilderson & Schrag 1998).

As discussed in detail in Section 4.3.3, three possible mechanisms are considered regarding how the 1976 PDO shift can affect coral ^{14}C in Baler: northward migration of the NEC bifurcation latitude, which results to (1) increased contribution of subtropical waters to the Baler site through the Kuroshio recirculation gyre and (2) decreased SP intrusion; and (3) increased upwelling in Central America. These PDO effects were considered in our model through Equations 9 and 10 (See Section 3.1.5), using k_{recirc} and k_{upw} values of .02 and .01 and $\chi_{intrusion}$ values of 0, 0, and 0.05 for boxes 21-23, respectively, starting from $t = 1976.0$.

Results (Figure 43a) show that just by a 2% increase in subtropical water recirculation in the box mixing model, a distinct increase in radionuclide concentration was observed at around the same time. A 1.5% increase in upwelling in boxes 13-15 and the decrease of SP intrusion, on the other hand, decreased back the radionuclide concentration 2 years after the shift, at around 1978. This resulting feature is similarly observed in actual measurements of the Baler coral, wherein ^{14}C jumped from 110‰ in 1974 to 184.6‰ in 1976 and 189.3‰ in 1977 then shifted back down to 166.4‰ in 1978 (Figure 33). These results show that our proposed mechanisms for the 1976 PDO shift affect the Baler site in the box mixing model similarly to the actual measurements and thus add to the plausibility of these explanations.

4.4.3. Specific coral ^{129}I trends

Remarkably, even while considering the effects of SP intrusion, quick input, subtropical recirculation, and upwelling in Central America, when the atmospheric lifetime of the radionuclide is switched back to two years, the resulting peak still happens at almost the same year and with comparable magnitude in both the Baler and Parola boxes (Figure 43b). This again demonstrates the robustness of the ^{129}I bomb peak, i.e., it is hardly affected by ocean processes and it is because of its short atmospheric lifetime. Nevertheless, a notable difference in shape and magnitude is observed in the simulated ^{129}I Baler peak. This is possibly because the box mixing model only roughly estimates the effect of SP intrusion.

To demonstrate this, Figure 44 shows the resulting ^{14}C and ^{129}I bomb curves in Baler with and without SP intrusion. For ^{14}C , SP intrusion appears to be responsible for making the small pre-bomb peak apparent as well as dampening the effect of upwelling in Central America (post-1976), such that the resulting decrease is not as strong. However, it is also responsible for altering the shape and magnitude of the resulting ^{129}I peak. Given that the intensity of SP intrusion varies per location as well as with time (e.g., seasonally), this experiment demonstrates the need for more accurate modeling of the SP intrusion, particularly its location and intensity as well as better estimates of ^{14}C levels in South Pacific waters, to be able to better simulate the observed coral ^{14}C and ^{129}I coral trends. Nonetheless, the box mixing model was sufficient to demonstrate the possible general effect of SP intrusion on ^{14}C values in the Baler site.

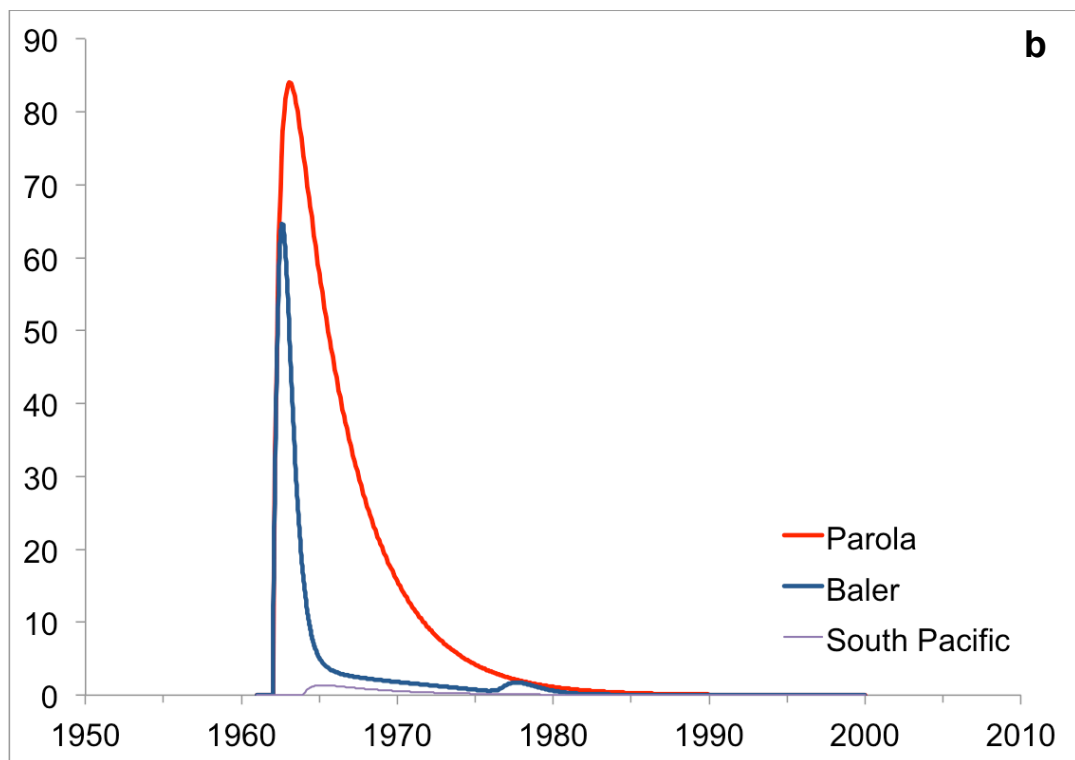
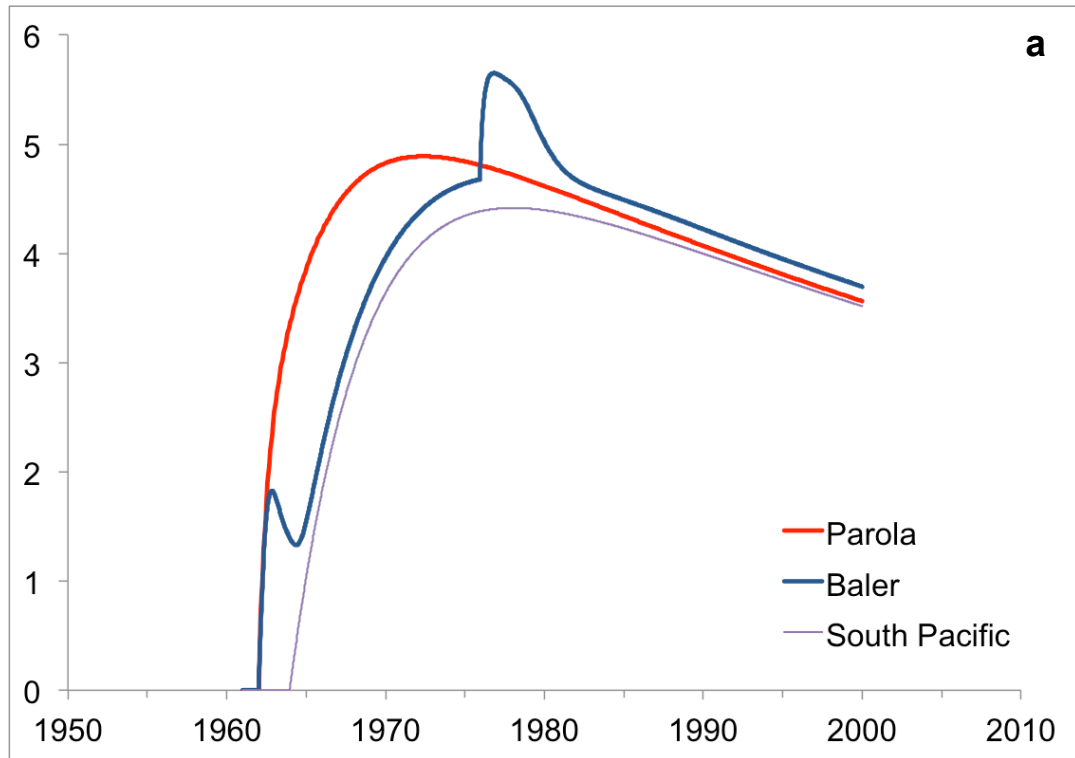


Figure 43. Simulated (a) ^{14}C and (b) ^{129}I bomb curve for Parola and Baler with SP intrusion, quick input, Kuroshio recirculation, and upwelling processes. Atmospheric lifetimes for ^{14}C and ^{129}I are 300 ($k_{A-O} = 2.557 \times 10^{-4}$) and 2 years ($k_{A-O} = 3.836 \times 10^{-2}$), respectively; $\chi_{intrusion}$ values are 0.05, 0.1, and 0.15 for boxes 21-23, respectively; χ_{quick} , k_{recirc} , and k_{upw} equals 0.015, 0.015, and 0.02, respectively. also shown is the variation of the South Pacific ocean box, O_{sp} (purple line).

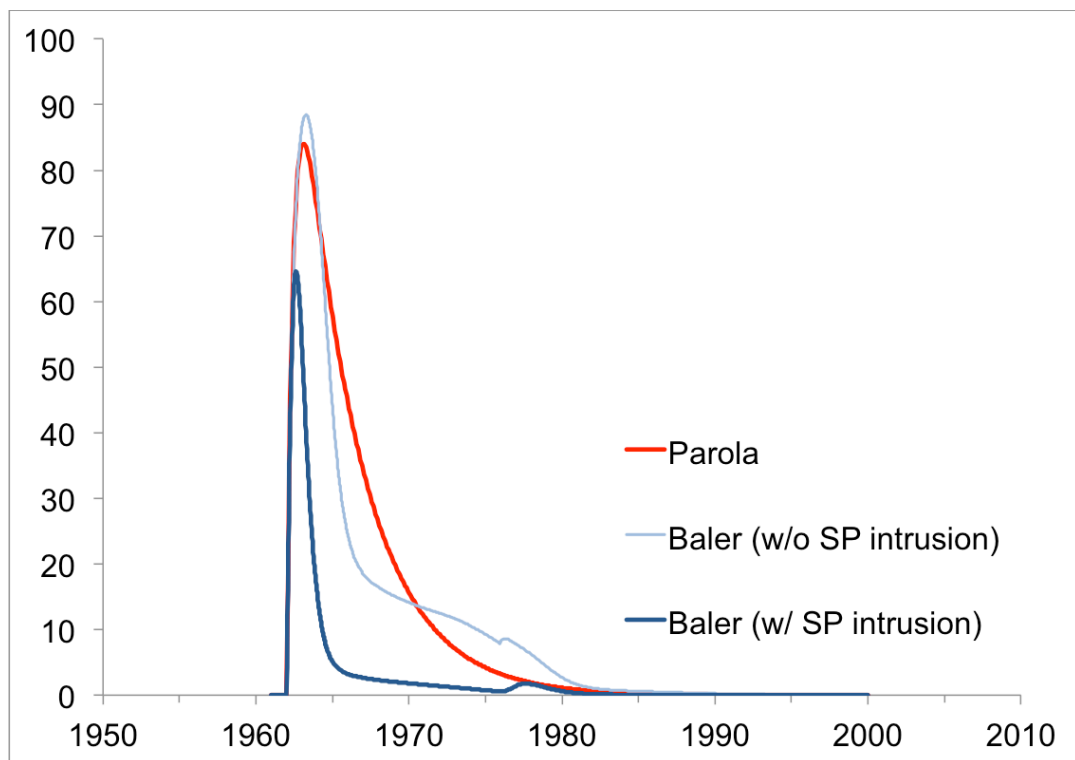
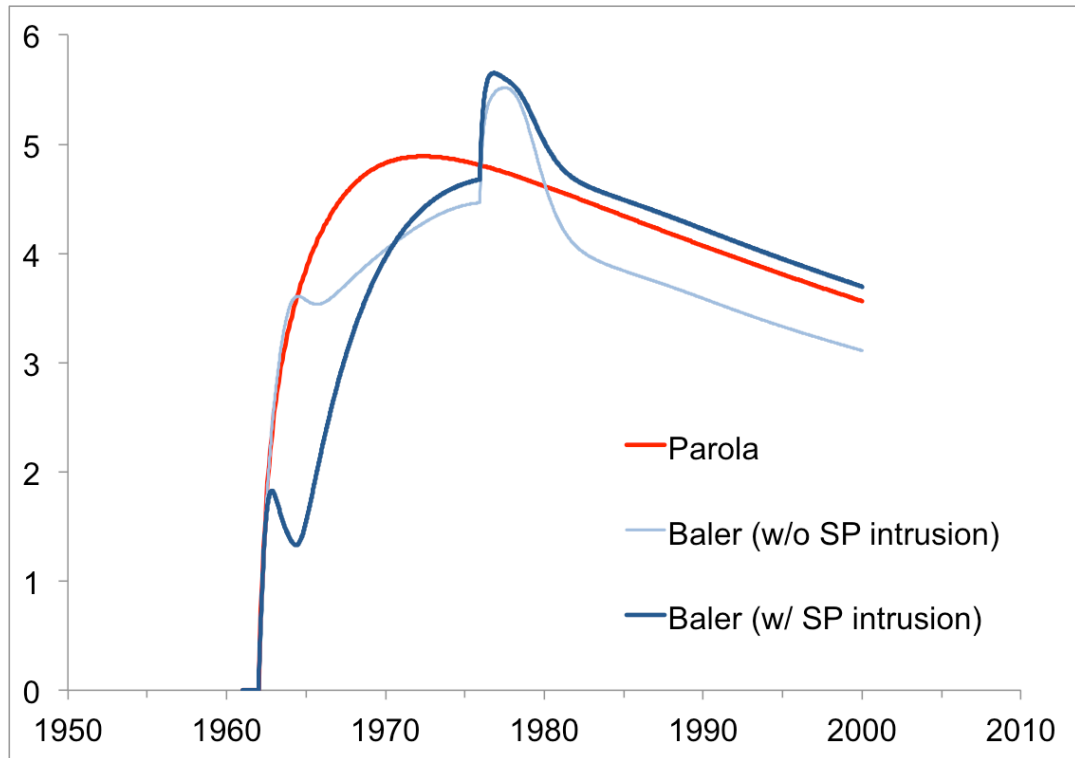


Figure 44. Simulated (a) ^{14}C and (b) ^{129}I bomb curve for Parola (red) and Baler with (dark blue) and without (light blue) SP intrusion. Atmospheric lifetimes for ^{14}C and ^{129}I are 300 ($k_{A-O} = 2.557 \times 10^{-4}$) and 2 years ($k_{A-O} = 3.836 \times 10^{-2}$), respectively; $\chi_{intrusion}$ values are 0.05, 0.1, and 0.15 for boxes 21-23, respectively for the run with SP intrusion, and 0 for all boxes for the run without SP intrusion; χ_{quick} , k_{recirc} , and k_{upw} equals 0.015, 0.015, and 0.02, respectively.

4.4.3.1. Pre-1962 ^{129}I signals

Another feature in the ^{129}I records of the Baler and Parola corals that I wanted to explore with the box mixing model was the signal from the pre-1962 bomb tests (See Section 4.2.2.). These tests were different because unlike other that injected most radionuclides to the stratosphere, a high percentage (around 44%) of the bomb-derived radionuclides of the pre-1962 tests were injected in the local, regional, and tropospheric layers (Figure 4; UNSCEAR 2000) and presumably transported to the Philippines by trade winds and the North Equatorial Current (Figure 20). Interestingly, ^{129}I signals from pre-1962 tests were observed in Parola (1953.5 and 1959), but not in Baler (Figure 32).

Using the box mixing model, radionuclide inputs were put only in the Parola system, as well as boxes 1, 22-25 of the Baler system because the bomb test site was located in box 22. However, we found that the pre-1962 signals did not decrease in the Baler ocean box, even with all the ocean processes we considered in the model. Nonetheless, given that (1) pre-1962 bomb-derived radionuclides were injected in the local, regional, and tropospheric layers, (2) average trade winds speed is about 28 km/hr, and that (3) each box from our model is $10^\circ \times 10^\circ$ or 1111.32 km across, it would take about 39.7 hours or roughly 1.65 days for the pre-1962 signal to cross 1 box. Given this, it would take about 6-8 days for the pre-1962 signal to reach the Baler and Parola site through atmospheric transport. Given such a short time, the observed pre-1962 signals in Parola and Baler would heavily depend on weather conditions (i.e., precipitation rate), during the week of the bomb tests because the primary pathway for atmosphere-to-ocean deposition of ^{129}I is through precipitation (Reithmeier et al. 2010). As demonstrated by the box mixing model (Figure 45) decreasing the input in boxes 1 and 22-25 by half results in a drastic decrease in the

observed signal. It is thus, not difficult to imagine how the pre-1962 bomb test ^{129}I signals were recorded in Parola but not in Baler.

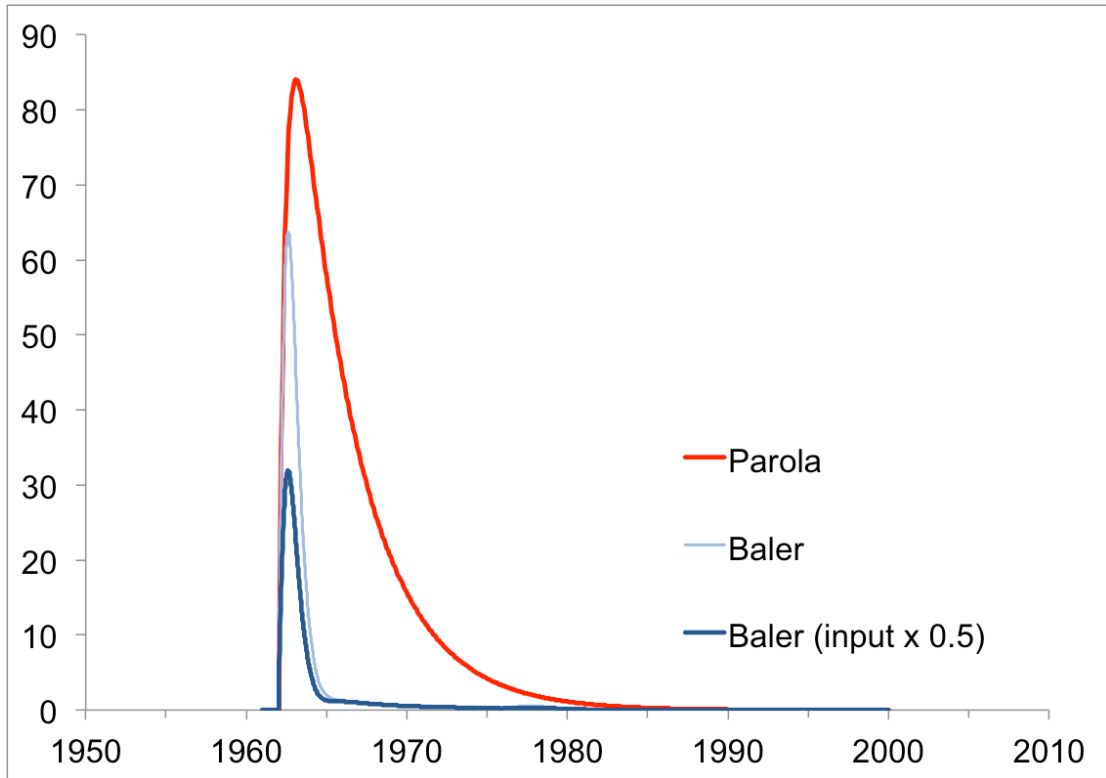


Figure 45. Pre-1962 ^{129}I signals simulated by the box mixing model for Parola and Baler.

Radionuclide inputs only over boxes Parola, 1, and 22-25. For Baler full (light line) and half (dark line) input magnitudes are shown.

4.4.3.2. Nuclear fuel reprocessing and Chernobyl accident signals

^{129}I in corals reflect not only nuclear bomb test signals but also those from nuclear fuel reprocessing (NFR) and nuclear accidents such as the Chernobyl accident. ^{129}I signals in Parola in 1977, 1980, and 1986 coincide with emission peaks during the height of NFR ^{129}I airborne emission as well as with the Chernobyl Accident. Baler coral, on the other hand, shows peaks in 1987, 1991, and 1995, which are possibly the same NFR and Chernobyl signals but with a 9 to 11-year lag (Figure 32). As proposed in Section 4.2.3, this time lag may reflect the different pathways

taken by ^{129}I to reach the Parola (SCS) and Baler (Pacific Ocean) sites. Atmospheric transport modeling (Reithmeier et al. 2010) shows that ^{129}I enters the SCS through direct deposition from the atmosphere and through deposition on catchment areas that drain to the SCS via surface runoff and rivers. For the Pacific Ocean, on the other hand, ^{129}I is carried by the westerlies and mainly deposited around 50 to 60°N, then subsequently transported by the North Pacific Gyre and North Equatorial Currents to the Baler site (Figure 20a).

This was simulated in the box mixing model by putting atmospheric radionuclide inputs in the Parola system, as well as boxes 2-6 of the Baler system at time $t = 1962.0$. Results show that while the signal peak occurred in 1963.1 in Parola, it was observed in 1973.1 for Baler (Figure 46). However, it is notable that the input in the Baler system had to be multiplied 30 times than that in Parola so that the magnitude of the resulting Baler peak would be about half of that in Parola. This may be attributed to the fact that (1) according to atmospheric transport modeling, the SCS already lies in the boundary of the area affected by the NFR and Chernobyl signal deposition (Reithmeier et al. 2010); and that the area covered by boxes 2-6 only represent a fraction of the actual area of the Pacific Ocean exposed to the NFR and Chernobyl signal deposition, and thus the signal received by the Baler system is also only a fraction of the actual deposition. Nonetheless, given that k_{adv} of boxes 1-25 were based on actual current velocities around the North Pacific Gyre, as determined by Maximenko et al. (2009), our simulation demonstrates the plausibility of our proposed mechanism for the observed NFR and Chernobyl signal trend between Parola and Baler.

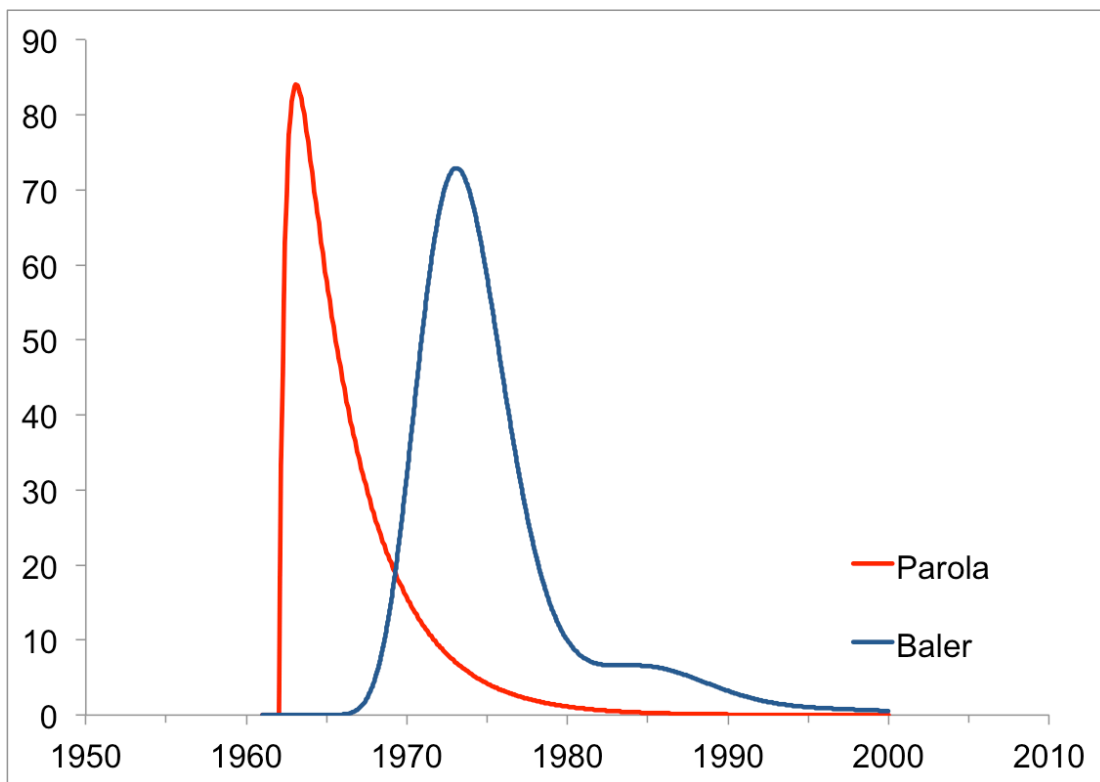


Figure 46. NFR and Chernobyl ^{129}I signal delay between Parola (red) and Baler (blue) simulated by box mixing model.

Radionuclide inputs only over boxes Parola, and 1-6; Inputs for boxes 1-6 were multiplied by 30.

4.5. ^{129}I in the Greenland Southeast Dome ice core

Values of ^{129}I in the Greenland SE-Dome ice core (in atoms $^{129}\text{I}/\text{mL H}_2\text{O}$) are listed in Appendix C. Measurement of the blank (ultrapure water that was stored, processed, and analyzed similar to actual samples) resulted to a $^{129}\text{I}/^{127}\text{I}$ of the AgI precipitate (sample + carrier) of $(3.5 \pm 0.7) \times 10^{-14}$. This value was used as blank correction for the sample measurements, which typically had AgI precipitate $^{129}\text{I}/^{127}\text{I}$ ratios around 41.1 to 88.2×10^{-14} . Average errors of the analysis (shown as error bars in Figure 47) are 11.8% and 7.8% for samples aged before and after the year 1960.

Figure 47 shows ^{129}I in the Greenland SE-Dome ice core as atoms $^{129}\text{I}/\text{mL H}_2\text{O}$. The entire ice core is divided into 189 samples. However, only sample numbers 139-187 are reported in this dissertation, having estimated ages of 1954 to 1973. Analysis and discussion of the results is in terms of the application of ^{129}I in the Greenland SE-Dome ice core as proxy of human nuclear activities (HNA), as time marker, and as an environmental tracer.

Similar to ^{129}I in corals from the Philippines (Section 4.2.), ^{129}I in the Greenland SE-Dome ice core record likewise functions as an excellent proxy of HNA. Nuclear bomb testing in 1958, 1961, and 1962 (Figure 2) appear to be well recorded in the ^{129}I ice core record, showing peaks in years 1957.2, 1960.4, 1961.3, and 1962.4. Peaks in 1961.3 and 1962.4 may possibly a single peak, with the trough in 1961.6 reflecting the seasonal reversal of stratospheric circulation (Figure 6). These prominent peaks are presumably signals from bomb tests performed by the Soviet Union, the test site of which is located close to the SE-Dome site (Figure 48). Nuclear bomb tests performed by the United States over the Pacific Ocean in years 1954 and 1958 may also be weakly recorded in the ^{129}I ice core record in peaks 1955.1 and 1958.4. Moreover, nuclear fuel reprocessing (NFR) signals from European NFR

facilities (Figure 10) are also well recorded by ^{129}I in the Greenland SE-Dome ice core, particularly in years 1965, 1969, and 1972. These results demonstrate that ^{129}I in ice core can be used to reconstruct the degree of HNA influence over land where this archive is taken.

One would also notice that ^{129}I signals in the Greenland SE-Dome ice core appear concurrently or only with a slight timing discrepancy to the identified possible sources. The timing discrepancy may have arisen from the preliminary ice core age model, which was constructed using the ice core's average accumulation rate of 1 m/y. In this regard, ^{129}I signals in the ice core can be used as time markers that can confirm and/or refine the preliminary age model of the ice core. Moreover, ^{129}I signals (i.e., 1962 bomb signal) that are observed in both the Greenland SE-dome ice core and in the corals from the Philippines can be used as “anchor points” to directly relate and compare ^{129}I (and other analytes or parameters, by extension) in these entirely different archive types. Therefore, ^{129}I do not only function as time markers for coral-to-coral and ice-to-ice core comparisons, but also for coral-to-ice core comparisons, effectively providing a direct link for coral/ice archives that are located in low/high latitudes and in marine/land environments. I expect to find more similarities between the ice and coral records once the younger parts of the core are analyzed.

I have only begun to analyze the possible applications of ^{129}I in the Greenland SE-Dome ice core as an environmental tracer. Some ideas that are possibly worth exploring include: (1) Analysis of the differences between signals that are possibly from the Soviet Union and the United States bomb tests – these signals may reveal the degree and speed of radionuclide transport from these two different bomb test sites; (2) Once the whole ice core has been analyzed, comparison between the existing Alpine ice core ^{129}I record (Reithmeier et al. 2006; Wagner et al. 1996) – Given that

the Greenland SE-Dome ice core and the existing Alpine ice core records are located in the west and east sides of the European NFR facilities (Figure 48), comparison between ^{129}I signals observed in these two ice cores may reveal interesting atmospheric circulation patterns.

Given these, there are many possibilities and large potential for future work and discussions regarding ^{129}I in the Greenland SE-Dome ice core. Nonetheless, the results presented in this dissertation have preliminarily shown the important applications and capabilities of ^{129}I in ice core archives as a HNA proxy, time marker, and environmental tracer and are thus sufficient for my intended objectives.

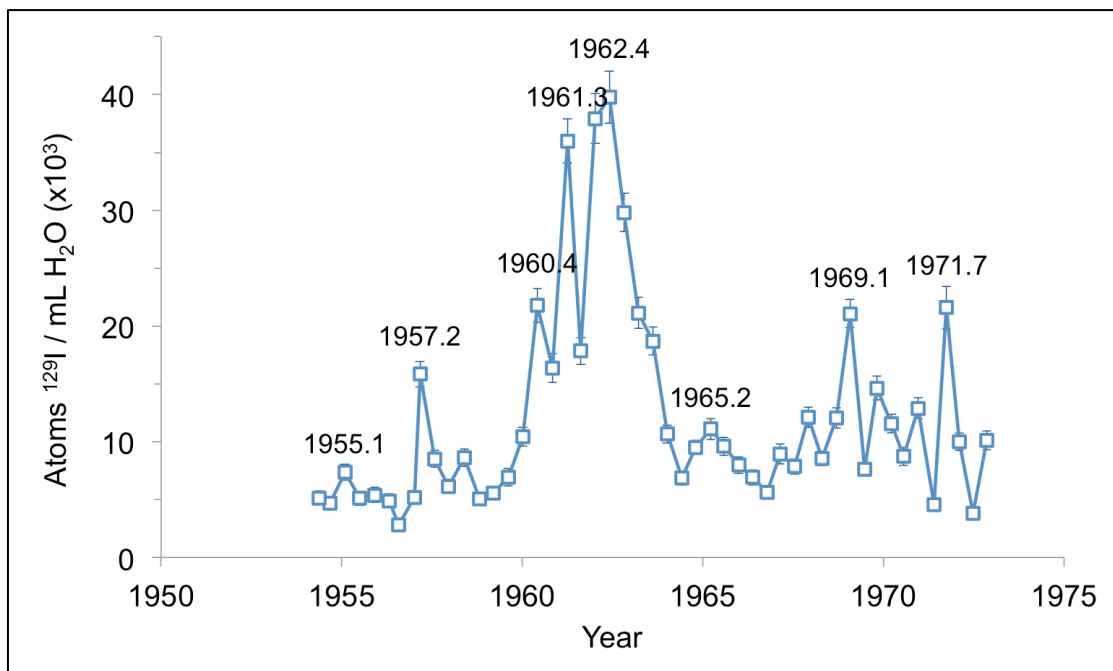


Figure 47. ^{129}I in the Greenland SE-Dome ice core (in 10^3 atoms/mL H_2O) and its corresponding errors (1σ).



Figure 48. Ice core records and HNA sources.

Shown are the existing ^{129}I ice core records in SE-Dome Greenland (yellow pin; this study) and Fiescherhorn, Alpine Region (blue pin; Reithmeier et al. 2006; Wagner et al. 1996); Nuclear bomb test sites (blasts) of the Soviet Union (red), United States (blue), and China (green); NFR Facilities in Europe (blue pins) and the former Soviet (purple pins); and the Chernobyl Accident (Star).

5. Summary and Conclusions

In summary, I first developed a new method capable of measuring $^{129}\text{I}/^{127}\text{I}$ in coral samples with as little as 1-4g of corals. Along with the smaller sample amount requirement, this method offers accuracy and precision comparable to the work of Biddulph et al. (2006), which used 10-30g of corals. This was accomplished by modifying the method of Biddulph et al. (2006) in two aspects: (1) the use of inductively coupled plasma mass spectrometry (ICP-MS) instead of ISE for the analysis of stable ^{127}I . ICP-MS matrix effect was minimized by using ^{133}Cs internal standard and finding an optimal dilution factor for sample solutions. A 286x dilution was eventually used, which was the largest dilution that resulted to a concentration higher than the method's limit of quantification of 0.27 ppb; and (2) the addition of 0.66 mg of low-ratio iodine carrier in the preparation of target for AMS analysis, instead of using carrier-free method. 0.66 mg of carrier was the smallest amount that forms sufficient amount of AgI for AMS measurement. This method can achieve a target error level of about 10% with as little as 1.5 g and 22.5 g for anthropogenic- and natural-age coral samples. Measurement using smaller sample sizes is also possible, but error levels will increase exponentially with decreasing sample size, as estimated the equation of the fitted line ($y = 3.6338\ln x + 15.609$) of 1/RSD vs. resulting ratio of the AgI precipitate (sample + carrier).

The development of this new method enabled the measurement of ^{129}I in corals from the Philippines, which was found to record human nuclear activities in good detail. This dissertation demonstrates how ^{129}I in coral samples the Pacific Ocean (Baler) and South China Sea (Parola) sides of the Philippines provide information about how the different nuclear activities affected the country, given the different atmospheric and oceanic regimes around the country and the region. Of particular

note are: the 1962 ^{129}I nuclear bomb peak observed in both Baler and Parola, which was also a potential new time marker comparable to the ^{14}C bomb peak; Nuclear fuel reprocessing and Chernobyl accident signals and how their 9 to 11-year timing difference in the Parola and Baler records suggests that ^{129}I entered the South China Sea directly from the atmosphere, while it traveled from the North Pacific to the Baler site through the prevailing ocean currents; and the anomalously high post-1996 ^{129}I concentration in Parola and how it may potentially reveal unknown sources of ^{129}I around the South China Sea region.

To provide comparison and additional insight to the coral ^{129}I results, the better-studied coral ^{14}C analysis was also performed on the same coral samples. Unlike ^{129}I , which has a variety of sources, ^{14}C only majorly comes from nuclear bomb testing. Expectedly, ^{14}C bomb curves were observed for both Parola and Baler. The onset of the ^{14}C bomb curve in Parola starts at around 1956-1958 and peaks in 1972. This timing is similar to ^{14}C of corals located inside the North and South Pacific Gyres (i.e., French Frigate Shoals and Rarotonga, respectively). This may be because Parola is likewise situated in the middle of the SCS circulation pattern and also because SCS is a semi-enclosed body of water with a shallow mixed layer depth, yearlong. These factors should enhance the surface water residence time and the atmosphere-to-surface ocean concentration of ^{14}C , and thus, possibly resulting to the rapid rise and peaking of $\Delta^{14}\text{C}$ in Parola. The onset of the ^{14}C bomb curve in Baler, meanwhile, also starts at around 1956-1958 but decreases again after 1962. Consequently, a small pre-bomb curve peak is formed in 1962 and the bomb curve of Baler appears to lag that of Parola. We propose two possible mechanisms to explain this: (1) “quick input” – i.e., a small portion of the bomb-produced ^{14}C having a form other than CO_2 that has a significantly quicker atmospheric lifetime; (2) “SP intrusion” – i.e., the intrusion of

South Pacific waters to the North Equatorial Current (NEC), which supplies the source water in Baler. “Quick input” may have suddenly increased $\Delta^{14}\text{C}$ in Baler (as well as Parola), but intrusion of the lower- ^{14}C SP waters to the NEC would have pushed $\Delta^{14}\text{C}$ in Baler back down. Also interesting is the fact that features of the Baler ^{14}C record coincide with phases of both El Niño Southern Oscillation (ENSO; particularly in years 1959, 1966, and 1973/74) and the Pacific Decadal Oscillation (PDO; 1976). Variations of coral ^{14}C , in relation to ENSO and PDO, can be explained by the northward shift of the NEC bifurcation latitude during El Niño years and the positive phase of the PDO, which causes increased contribution of northern subtropical waters through the Kuroshio recirculation gyre. Additionally, strengthened upwelling in the Central American region is also considered in the case of the 1976 PDO shift. These results show that unlike ^{129}I , the coral ^{14}C is only majorly affected by nuclear bomb testing and the resulting ^{14}C bomb curve is broad and varies in timing and shape depending on coral location. Given these, it can be said that ^{14}C is a poorer tracer of HNA activity and a poorer time marker than ^{129}I . Coral ^{14}C , however, is capable of reflecting ocean processes, such as the variations of the ENSO and PDO, which coral ^{129}I is unable to do so.

To investigate and demonstrate the comparison between ^{129}I and ^{14}C in more detail, a box mixing model capable of simulating the two radionuclides for Parola and Baler was developed and used. Through this box model, it was demonstrated that the difference between the atmosphere-to-ocean lifetimes of ^{129}I and ^{14}C might be the largest factor for the observed trends in the two nuclides. In particular, the quicker (i.e., 2 years) atmospheric lifetime of ^{129}I causes a sharper, more robust peak that is uniform in timing and shape, regardless of the oceanic processes in the location of the coral. The longer atmospheric lifetime (i.e., 300 years, for this model) of ^{14}C causes

the broad peak, which is sensitive to ocean processes, causing variations in the ^{14}C bomb curve's timing and shape. The simulated ^{14}C bomb curve has a more delayed peak for Baler than Parola, because of the effect of the north pacific gyre circulation for the former, and the semi-enclosed nature of the SCS for the latter. The box mixing model was also able to demonstrate the plausibility of specific mechanisms for both ^{129}I and ^{14}C , that I proposed to explain the observed trends in these radionuclides in the previous sections. Specifically, these are: (1) "SP intrusion" and "quick input", which causes the small pre-bomb curve peak and the delay of the simulated Baler ^{14}C bomb curve; (2) the 1976 PDO shift, particularly the increased contribution of northern subtropical waters and the increased upwelling in the Central American region, which are both due to the northward shift of the NEC bifurcation latitude. The simulated PDO shift resulted to a specific peak structure in 1976-1978 also observed in the actual measurements of Baler ^{14}C bomb curve; and (3) pre-1962 ^{129}I signal discrepancy and the delay of the NFR and Chernobyl ^{129}I signals between Parola and Baler, as a result of different pathways wherein ^{129}I entered the South China Sea directly from the atmosphere, while it traveled from the North Pacific to the Baler site through the prevailing ocean currents.

These results demonstrate that coral ^{129}I records human nuclear activities, namely, nuclear bomb tests, nuclear fuel reprocessing, and nuclear accidents better than the better-studied ^{14}C . As a time marker, the coral ^{129}I bomb peak is also clearly better than the coral ^{14}C bomb curve because, as shown in the measurements and validated with the box mixing model, ^{129}I bomb peak appears almost in the same year as the time of atmospheric release and it is hardly affected by ocean processes primarily because of its short atmospheric lifetime. Coral ^{14}C bomb curves, in contrast, vary in timing, shape, and magnitude depending on the oceanic processes in

the location of the coral, as a consequence of the long atmospheric lifetime of ^{14}C . Nonetheless, the large difference in atmospheric lifetimes of ^{129}I and ^{14}C has caused these radionuclides to have distinct applications as oceanic tracers: coral ^{129}I signals are able to trace the speed of ocean circulation, as demonstrated by the timing discrepancy in NFR and Chernobyl signals between Parola and Baler; coral ^{14}C , on the other hand, are able to reflect large and long-term scale changes in circulation such as SP intrusion and the effects of the ENSO phases and the 1976 PDO shift.

In addition, although the specific mechanism of iodine uptake by corals have not been elucidated, good agreement between the observed ^{129}I signals and their supposed sources suggest that coral skeletons preserve and record ^{129}I in the surface seawater during the time of their formation, with minimal cross-contamination between annual growth bands.

Lastly, I measured ^{129}I in an ice core from the Southeast (SE) dome of Greenland where I similarly found that ^{129}I signals from nuclear bomb testing and NFR are recorded concurrently in the ice core, specifically in years 1958, 1961, 1962 and 1965, 1969, 1972, respectively. This demonstrates that ^{129}I can also be used as a HNA proxy and a time marker not only for corals, but also for ice cores. ^{129}I thus effectively provides a direct link between two entirely different archives: coral/ice core, low/high latitude locations, and marine/land environments. The “anchor points” that these ^{129}I signals provide will enable researchers to establish/confirm their age models, and directly compare ^{129}I (and other analytes or parameters, by extension) records between different ice and coral cores, with increased confidence. Some possible environmental tracer applications that may be explored in the future, once the whole Greenland SE dome ^{129}I ice core record has been constructed, include analysis of bomb signals between Soviet and US tests, which may reveal information about the

stratospheric transport of bomb test radionuclides from the Soviet and US test sites to the ice core location; and comparison from the existing Alpine ice core ^{129}I record, which may reveal interesting atmospheric circulation patterns since Greenland and the Alpine region are located in opposite sides of the European NFR facilities.

Integrating all these results, the main contributions of this dissertation are: (1) it has demonstrated that ^{129}I in coral and ice cores are excellent proxies of HNAs, particularly nuclear bomb testing, nuclear fuel reprocessing, and nuclear accidents, recording these activities in these natural archives with unprecedented detail. Thus, ^{129}I in these archives can be used to assess the effect of HNAs in the locations where the archives were taken (i.e., The Philippines and Greenland); (2) that ^{129}I in these archives also provide pertinent information about the atmospheric and oceanic pathways that HNA-derived radionuclides take from the point of release to the locations where natural archives were taken. This information can be used for nuclear safety and security in the event of future nuclear incidents and/or for studying these associated earth processes; and (3) it has demonstrated that ^{129}I in coral and ice cores provide an excellent time marker that can establish and confirm the age models of the archives as well as provide an “anchor point” that will enable us to directly relate and compare different coral and ice records. In the case of the coral archives, these applications were demonstrated in comparison to the better-known ^{14}C , which provided context and made these important applications of ^{129}I more apparent.

I believe that the results presented in this dissertation will interest studies of ^{129}I in coral and ice cores in different locations to confirm the ubiquity of the observed ^{129}I signals and their possible applications. I also believe that this dissertation will encourage investigations to ascertain the source and the possible oceanographic tracer application of the high ^{129}I levels in the South China Sea. Moreover, it may start a

review of the available coral ^{14}C records, in light of the new mechanisms proposed here, particularly the SP intrusion and the quick input. These findings merit that both ^{129}I and ^{14}C be studied side-by-side in more corals from other locations to fully explore the potential of their applications. We also recommend that higher resolution and more sophisticated modeling studies be conducted for these radionuclides, given that some aspects (e.g., SP intrusion) were not modeled sufficiently in this work. More in-depth studies and representation of the mechanisms proposed in this dissertation would largely contribute to the better understanding of the dynamics and possible applications of these radionuclides in the management of nuclear energy and technology and in the study of earth processes and the environment.

References

- Aldahan, A., Alfimov, V. & Possnert, G., 2007. 129I anthropogenic budget: Major sources and sinks. *Applied Geochemistry*, 22(3), pp.606–618. Available at: <http://linkinghub.elsevier.com/retrieve/pii/S0883292706003064> [Accessed August 21, 2014].
- Bauer, S.E. et al., 2013. Historical and future black carbon deposition on the three ice caps: Ice core measurements and model simulations from 1850 to 2100. *Journal of Geophysical Research: Atmospheres*, 118(14), pp.7948–7961. Available at: <http://doi.wiley.com/10.1002/jgrd.50612>.
- Biddulph, D.L. et al., 2006. Two 60-year records of 129 I from coral skeletons in the South Pacific Ocean. *Radioactivity in the Environment*, 8(05), pp.592–598.
- de Boyer Montégut, C. et al., 2004. Mixed layer depth over the global ocean: An examination of profile data and a profile-based climatology. *Journal of Geophysical Research C: Oceans*, 109(12), pp.1–20.
- Casacuberta, N. et al., 2014. A first transect of 236U in the North Atlantic Ocean. *Geochimica et Cosmochimica Acta*, 133, pp.34–46.
- Christl, M. et al., 2015. Reconstruction of the 236 U input function for the northeast Atlantic Ocean-Implications for 129 I/ 236 U and 236 U/ 238 U-based tracer ages. *Journal of Geophysical Research: Oceans*. Available at: <http://doi.wiley.com/10.1002/2015JC011116>.
- Cooper, L.W. et al., 1998. Iodine-129 and plutonium isotopes in Arctic kelp as historical indicators of transport of nuclear fuel-reprocessing wastes from mid-to-high latitudes in the Atlantic Ocean. *Marine Biology*, 131(3), pp.391–399.
- CTBTO, 2001. Philippines Ratifies Nuclear-Test-Ban Treaty. Available at: <https://www.ctbto.org/press-centre/press-releases/2001/philippines-ratifies->

comprehensive-nuclear-test-ban-treaty/.

- Denman, K.L. et al., 2007. *Couplings Between Changes in the Climate System and Biogeochemistry* S. Solomon et al., eds., Cambridge, United Kingdom and New York, NY, USA., United Kingdom and New York, NY, USA.: Cambridge University Press. Available at:
<http://scholar.google.com/scholar?hl=en&btnG=Search&q=intitle:Couplings+Between+Changes+in+the+Climate+System+and+Biogeochemistry#0>.
- Druffel, E.R.M., 1987. Bomb radiocarbon in the Pacific: Annual and seasonal timescale variations. *Journal of Marine Research*, 45(3), pp.667–698. Available at: <http://openurl.ingenta.com/content/xref?genre=article&issn=0022-2402&volume=45&issue=3&spage=667>.
- Druffel, E.R.M. & Griffin, S., 2004. Southern Great Barrier Reef Coral Radiocarbon Data. In *IGBP PAGES/World Data Center for Paleoclimatology*. Boulder CO, USA: NOAA/NDCC Paleoclimatology Program.
- Duran, E.B. et al., 2004. ^{137}Cs and $^{239+240}\text{Pu}$ levels in the Asia-Pacific regional seas. *Journal of Environmental Radioactivity*, 76(1-2), pp.139–160.
- ESR, 2009. OSCAR third degree resolution ocean surface currents Ver. 1.
- Fabryka-Martin, J. et al., 1985. Natural iodine-129 as an environmental tracer. *Geochimica et Cosmochimica Acta*, 49, pp.337–347. Available at:
<http://www.sciencedirect.com/science/article/pii/0016703785900274> [Accessed August 21, 2014].
- Fallon, S.J. & Guilderson, T.P., 2008. Surface water processes in the Indonesian throughflow as documented by a high-resolution coral $\Delta 14\text{C}$ record. *Journal of Geophysical Research*, 113(C9), p.C09001. Available at:
<http://doi.wiley.com/10.1029/2008JC004722>.

- Fan, Y. et al., 2016. 129I record of nuclear activities in marine sediment core from Jiaozhou Bay in China. *Journal of Environmental Radioactivity*, 154(March 2011), pp.15–24. Available at:
<http://linkinghub.elsevier.com/retrieve/pii/S0265931X1630008X>.
- Gordon, A.L. et al., 2014. The nascent Kuroshio of Lamon Bay. *Journal of Geophysical Research: Oceans*, 119(7), pp.4251–4263. Available at:
<http://doi.wiley.com/10.1002/2014JC009882>.
- Grottoli, A.G. et al., 2003. Decadal timescale shift in the 14C record of a central equatorial Pacific coral. *Radiocarbon*, 45(1), pp.91–99. Available at: <Go to ISI>://000186131000010.
- Grottoli, A.G. & Eakin, C.M., 2007. A review of modern coral $\delta^{18}\text{O}$ and $\Delta^{14}\text{C}$ proxy records. *Earth-Science Reviews*, 81(1-2), pp.67–91.
- Guilderson, T.P. et al., 1998. Radiocarbon variability in the western equatorial Pacific inferred from a high-resolution coral record from Nauru Island. *Journal of Geophysical Research*, 103(C11), p.24641. Available at:
<http://doi.wiley.com/10.1029/98JC02271>.
- Guilderson, T.P. et al., 2000. Southwest subtropical Pacific surface water radiocarbon in a high-resolution coral record. *Radiocarbon*, 42(2), pp.249–256. Available at:
http://radiocarbon.library.arizona.edu/Volume42/Number2/azu_radiocarbon_v42_n2_249_256_v.pdf.
- Guilderson, T.P. & Schrag, D.P., 1998. Abrupt Shift in Subsurface Temperatures in the Tropical Pacific Associated with Changes in El Niño. *Science*, 281(5374), pp.240–243. Available at:
<http://www.sciencemag.org/cgi/doi/10.1126/science.281.5374.240>.
- Guilderson, T.P., Schrag, D.P. & Cane, M.A., 2004. Surface Water Mixing in the

- Solomon Sea as Documented by a High-Resolution Coral ^{14}C Record. *Journal of Climate*, 17(5), pp.1147–1156. Available at:
[http://journals.ametsoc.org/doi/abs/10.1175/1520-0442\(2004\)017<1147:SWMITS>2.0.CO;2](http://journals.ametsoc.org/doi/abs/10.1175/1520-0442(2004)017<1147:SWMITS>2.0.CO;2) [Accessed August 12, 2014].
- He, P. et al., 2013. A summary of global ^{129}I in marine waters. *Nuclear Instruments and Methods in Physics Research Section B: Beam Interactions with Materials and Atoms*, 294, pp.537–541. Available at:
<http://linkinghub.elsevier.com/retrieve/pii/S0168583X12005629>.
- Honda, M. et al., 2015. Depth profile and mobility of ^{129}I and ^{137}Cs in soil originating from the Fukushima Dai-ichi Nuclear Power Plant accident. *Journal of Environmental Radioactivity*, 146, pp.35–43. Available at:
<http://www.sciencedirect.com/science/article/pii/S0265931X15001009>.
- Hou, X. et al., 2013. Iodine-129 in seawater offshore Fukushima: distribution, inorganic speciation, sources, and budget. *Environmental science & technology*, 47(7), pp.3091–8. Available at: <http://www.ncbi.nlm.nih.gov/pubmed/23461388>.
- Hou, X. et al., 2009. Time series of ^{129}I and ^{127}I speciation in precipitation from Denmark. *Environmental science & technology*, 43(17), pp.6522–8. Available at: <http://www.ncbi.nlm.nih.gov/pubmed/19764211>.
- Hou, X. & Hou, Y., 2012. Analysis of ^{129}I and its Application as Environmental Tracer. *Journal of Analytical Science & Technology*, 3, pp.135–153.
- Hu, J. et al., 2000. A Review on the currents in the South China Sea: Seasonal circulation, South China Sea warm current and Kuroshio intrusion. *Journal of Oceanography*, 56(6), pp.607–624.
- ICH, 2005. ICH Topic Q2 (R1) Validation of Analytical Procedures : Text and Methodology. *International Conference on Harmonization (ICH) Harmonised*

- Tripartite Guideline*, 1994(November 1996), p.17.
- Iizuka, Y. et al., 2016. Glaciological and meteorological observations at the SE-Dome site, southeastern Greenland Ice Sheet. *Bulletin of Glaciological Research*, 34, pp.1–10. Available at: https://www.jstage.jst.go.jp/article/bgr/34/0/34_1/_article.
- Joos, F. et al., 2001. Global warming feedbacks on terrestrial carbon uptake under the Intergovernmental Panel on Climate Change (IPCC) Emission Scenarios. *Global Biogeochemical Cycles*, 15(4), pp.891–907.
- Kashino, Y. et al., 2009. Observations of the North Equatorial Current, Mindanao Current, and Kuroshio current system during the 2006/07 El Niño and 2007/08 La Niña. *Journal of Oceanography*, 65(3), pp.325–333. Available at: <http://link.springer.com/10.1007/s10872-009-0030-z>.
- Kim, Y.Y. et al., 2004. Seasonal and interannual variations of the North Equatorial Current bifurcation in a high-resolution OGCM. *Journal of Geophysical Research-Oceans*, 109(C3), p.19. Available at: <Go to ISI>://WOS:000220623000002\http://onlinelibrary.wiley.com/doi/10.1029/2003JC002013/abstract\http://onlinelibrary.wiley.com/store/10.1029/2003JC002013/asset/jgrc9452.pdf?v=1&t=htk5h6ze&s=7ed95365418700f10d2914dc6dcddf43599d00f5.
- Konishi, K., Tanaka, T. & Sakanoue, M., 1981. Secular variation of radiocarbon concentrations in seawater: sclerochronological approach. In E. D. Gomez, ed. *Proceedings of the Fourth International Coral Reef Symposium*. Manila, pp. 181–185.
- Long, N.Q. et al., 2012. Atmospheric radionuclides from the Fukushima Dai-ichi nuclear reactor accident observed in Vietnam. *Journal of Environmental Radioactivity*, 111, pp.53–58. Available at:

- <http://dx.doi.org/10.1016/j.jenvrad.2011.11.018>.
- Mahadevan, A., 2001. An analysis of bomb radiocarbon trends in the Pacific. *Marine Chemistry*, 73(3-4), pp.273–290.
- Mantua, N.J. et al., 1997. A Pacific Interdecadal Climate Oscillation with Impacts on Salmon Production. *Bulletin of the American Meteorological Society*, 78(6), pp.1069–1079. Available at: [http://journals.ametsoc.org/doi/abs/10.1175/1520-0477\(1997\)078<1069:APICOW>2.0.CO;2](http://journals.ametsoc.org/doi/abs/10.1175/1520-0477(1997)078<1069:APICOW>2.0.CO;2).
- Matsuzaki, H. et al., 2015. The status of the AMS system at MALT in its 20th year. *Nuclear Instruments and Methods in Physics Research Section B: Beam Interactions with Materials and Atoms*, 361(March 2014), pp.63–68. Available at: <http://linkinghub.elsevier.com/retrieve/pii/S0168583X15005273>.
- Maximenko, N. et al., 2009. Mean dynamic topography of the ocean derived from satellite and drifting buoy data using three different techniques. *Journal of Atmospheric and Oceanic Technology*, 26(9), pp.1910–1919.
- Miyake, Y. et al., 2012. Isotopic ratio of radioactive iodine ($^{129}\text{I}/^{131}\text{I}$) released from Fukushima Daiichi NPP accident. *Geochemical Journal*, 46, pp.327–333.
- Moran, J.E. et al., 1999. Atmospheric Dispersal of ^{129}I from Nuclear Fuel Reprocessing Facilities. *Environmental Science & Technology*, 33(15), pp.2536–2542. Available at: <http://pubs.acs.org/doi/abs/10.1021/es9900050>.
- Moran, J.E., Fehn, U. & Teng, R.T.D., 1998. Variations in $\text{I-}^{129}/\text{I-}^{127}$ ratios in recent marine sediments: evidence for a fossil organic component. *Chemical Geology*, 152(1-2), pp.193–203. Available at: ISI:000076849100017.
- Muramatsu, Y. et al., 2008. AMS analysis of ^{129}I in Japanese soil samples collected from background areas far from nuclear facilities. *Quaternary Geochronology*, 3(3), pp.291–297. Available at:

<http://linkinghub.elsevier.com/retrieve/pii/S187110140700057X>.

- Muramatsu, Y. et al., 2004. Studies with natural and anthropogenic iodine isotopes: iodine distribution and cycling in the global environment. *Journal of environmental radioactivity*, 74(1-3), pp.221–32. Available at: <http://www.ncbi.nlm.nih.gov/pubmed/15063550> [Accessed August 21, 2014].
- Peng, T.H., Key, R.M. & Östlund, H.G., 1998. Temporal variations of bomb radiocarbon inventory in the Pacific Ocean. *Marine Chemistry*, 60(1-2), pp.3–13.
- Ramos, R., 2016. Sr/Ca Measurements of the Parola Coral Core (unpublished raw data).
- Reithmeier, H. et al., 2010. Anthropogenic ¹²⁹I in the atmosphere: overview over major sources, transport processes and deposition pattern. *The Science of the total environment*, 408(21), pp.5052–64. Available at: <http://www.ncbi.nlm.nih.gov/pubmed/20692686> [Accessed August 21, 2014].
- Reithmeier, H. et al., 2006. Estimate of European ¹²⁹I releases supported by ¹²⁹I analysis in an Alpine ice core. *Environmental science & technology*, 40, pp.5891–5896.
- Shen, C.C. et al., 1996. The calibration of D[Sr/Ca] versus sea surface temperature relationship for Porites corals. *Geochimica et Cosmochimica Acta*, 60(20), pp.3849–3858.
- Smith, T.M. et al., 2008. Improvements to NOAA’s historical merged land-ocean surface temperature analysis (1880-2006). *Journal of Climate*, 21(10), pp.2283–2296.
- Solomon, S. et al., 2007. *Technical Summary*, Cambridge, United Kingdom and New York, NY, USA.: Cambridge University Press.
- Stan-Sion, C., Enachescu, M. & Petre, A.R., 2015. AMS analyses of I-129 from the

- Fukushima Daiichi nuclear accident in the Pacific Ocean waters of the Coast La Jolla – San Diego, USA. *Environ. Sci.: Processes Impacts*, 17(5), pp.932–938. Available at: <http://dx.doi.org/10.1039/C5EM00124B>.
- Stuvier, M. & Polach, H.A., 1977. Reporting of ¹⁴C Data. *Radiocarbon*, 19(3), pp.355–363.
- Thomas, R., 2013. *Practical Guide to ICP-MS* 3rd ed., Boca Raton, FL: CRC Press, Taylor and Francis Group.
- UNSCEAR, 2000. *Sources and effects of ionizing radiation. UNSCEAR 2000 Report to the General Assembly, Annex C: exposures from man-made sources of radiation*, New York.
- Wagner, M.J.M. et al., 1996. Increase of ¹²⁹I in the environment. *Nuclear Instruments and Methods in Physics Research Section B: Beam Interactions with Materials and Atoms*, 113(1-4), pp.490–494. Available at: <http://linkinghub.elsevier.com/retrieve/pii/0168583X95013482>.
- Wang, L.C. & Wu, C.R., 2013. Contrasting the flow patterns in the equatorial Pacific between two types of El Niño. *Atmosphere - Ocean*, 51(1), pp.60–74. Available at: <http://www.scopus.com/inward/record.url?scp=84879364479&partnerID=8YFLogxK>
<http://www.scopus.com/inward/citedby.url?scp=84879364479&partnerID=8YFLogxK>.
- Wang, Q. & Hu, D., 2006. Bifurcation of the North Equatorial Current derived from altimetry in the Pacific Ocean. *Journal of Hydrodynamics, Ser. B*, 18(5), pp.620–626. Available at: <http://linkinghub.elsevier.com/retrieve/pii/S1001605806601443>.
- Wessel, P. & Smith, W.H.F., 2013. *Generic Mapping Tools: Improved version*

released. *EOS Trans. AGU*, 94(45), pp.409–10.

Winkler, S.R., Steier, P. & Carilli, J., 2012. Bomb fall-out ^{236}U as a global oceanic tracer using an annually resolved coral core. *Earth and Planetary Science Letters*, 359-360(1), pp.124–130. Available at:
<http://dx.doi.org/10.1016/j.epsl.2012.10.004>.

Yang, J., Lin, X. & Wu, D., 2013. On the dynamics of the seasonal variation in the South China Sea throughflow transport. *Journal of Geophysical Research: Oceans*, 118(12), pp.6854–6866. Available at:
<http://doi.wiley.com/10.1002/2013JC009367>.

Yii, M.W., Zaharudin, A. & Norfaizal, M., 2007. Concentration of radiocaesium ^{137}Cs and ^{134}Cs in sediments of the Malaysian marine environment. *Applied Radiation and Isotopes*, 65(12), pp.1389–1395.

Appendix

Appendix A. Coral ^{127}I , $^{129}\text{I}/^{127}\text{I}$, and corresponding errors (1σ).

Sample Name	Year	^{127}I (ppm)	^{127}I error	$^{127}\text{I}/^{129}\text{I}$ ($\times 10^{-12}$)	$^{127}\text{I}/^{129}\text{I}$ error ($\times 10^{-12}$)
Baler					
bal2b3738	1917.5	4.438	0.142	1.234	0.439
bal2b3536	1919.5	4.442	0.096	2.834	0.763
bal2b3334	1921.5	4.504	0.028	1.740	0.358
bal2b3132	1923.5	4.173	0.102	1.129	0.315
bal2b2930	1925.5	4.125	0.142	1.569	0.366
bal2b2728	1927.5	3.876	0.044	1.241	0.286
bal2b2326	1929.5	3.922	0.132	1.967	0.498
bal2b2123	1931.5	4.117	0.025	0.845	0.185
bal2b1920	1933.5	4.385	0.016	0.751	0.178
bal2b1718	1935.5	4.224	0.035	0.920	0.189
bal2b1516	1937.5	4.281	0.084	2.625	0.541
bal2b1314	1939.5	4.613	0.043	0.727	0.177
bal2b1112	1941.5	4.575	0.135	0.972	0.226
bal2b910	1943.5	4.150	0.115	2.215	0.363
bal2b78	1945.5	4.776	0.188	0.743	0.166
bal2b6	1947	5.610	0.111	1.437	0.247
bal2b5	1948	5.454	0.100	0.802	0.196
bal2b4	1949	6.651	0.093	0.621	0.134
bal2b3	1950	5.463	0.118	1.748	0.301
bal2b2	1951	5.826	0.237	1.389	0.270
bal2b1	1952	6.206	0.164	1.508	0.239
Bal2ABot	1954	4.256	0.106	1.343	0.212
bal2a4950	1956.5	5.489	0.077	1.307	0.215
bal2a4748	1958.5	5.409	0.055	1.571	0.255
bal2a4546	1960.5	5.607	0.073	7.061	0.604
bal2a4344	1962.5	5.539	0.144	29.681	2.004
bal2a4142	1964.5	5.754	0.092	14.015	1.022
bal2a3940	1966.5	5.379	0.072	18.422	1.508
bal2a3738	1968.5	5.600	0.160	8.715	0.733
bal2a3536	1970.5	5.499	0.028	10.529	0.838
bal2a3334	1972.5	5.094	0.115	12.226	1.251
bal2a3132	1974.5	5.227	0.141	11.834	1.030
Bal2A2930	1976.5	4.296	0.039	15.809	0.970
bal2a2728	1978.5	5.995	0.114	11.796	0.963
bal2a2526	1980.5	5.469	0.094	14.662	1.217
bal2a2324	1982.5	6.160	0.125	15.986	1.083
bal2a2122	1984.5	5.665	0.071	18.666	1.198
bal2a1920	1986.5	5.654	0.144	21.087	1.607
bal2a1718	1988.5	5.343	0.123	19.685	1.498

Sample Name	Year	^{127}I (ppm)	^{127}I error	$^{127}\text{I}/^{129}\text{I}$ ($\times 10^{-12}$)	$^{127}\text{I}/^{129}\text{I}$ error ($\times 10^{-12}$)
Baler (continued)					
bal2a1516	1990.5	5.385	0.058	21.793	1.513
bal2a1314	1992.5	5.620	0.197	19.967	1.472
bal2a1112	1994.5	4.919	0.089	26.734	1.812
bal2a910	1996.5	5.145	0.109	20.553	1.644
bal2a78	1998.5	5.268	0.074	19.186	1.424
bal2a56	2000.5	5.424	0.131	19.347	1.483
bal2a34	2002.5	5.455	0.120	16.513	1.276
Parola					
32SPR1C01	1953.5	3.795	0.057	5.990	0.553
33SPR1C02	1954.5	3.793	0.070	2.308	0.249
34SPR1C03	1955.5	3.477	0.097	1.874	0.247
35SPR1C04	1956.5	3.629	0.032	8.202	1.469
36SPR1C05	1957.5	3.724	0.044	13.556	2.832
37SPR1C67	1959	3.821	0.044	18.015	1.958
38SPR1C08	1960.5	3.647	0.085	15.110	2.452
39SPR1C09	1961.3	3.822	0.088	10.199	1.199
40SPR1C10	1961.6	3.792	0.070	16.197	1.574
41SPR1C11	1962.5	3.355	0.032	33.199	6.389
42SPR1C12	1963.5	3.784	0.068	25.046	6.110
43SPR1C1314	1965.25	3.618	0.087	13.346	5.517
44SPR1C1415	1966.25	3.791	0.067	17.138	5.526
45SPR1C1617	1967.5	3.373	0.022	19.532	5.353
spr1c1819	1968.75	5.080	0.056	14.271	1.722
spr1cbot	1970	4.475	0.153	17.509	1.959
31SPR1BBot	1971.5	3.980	0.081	11.590	2.390
30SPR1B15	1973	3.698	0.037	15.717	2.230
29SPR1B14	1974	3.806	0.065	12.576	1.913
28SPR1B13	1975	3.861	0.042	16.659	2.143
27SPR1B12	1976	3.503	0.021	18.884	2.313
26SPR1B11	1977	3.239	0.028	17.925	2.758
25SPR1B10	1977.3	3.406	0.020	28.955	3.329
24SPR1B09	1977.6	3.368	0.054	26.632	4.012
23SPR1B08	1978.5	3.575	0.071	21.505	2.588
22SPR1B07	1979.5	3.613	0.062	26.320	2.520
21SPR1B06	1980	3.578	0.103	29.946	2.715
20SPR1B05	1981	3.826	0.074	23.911	2.491
19SPR1B04	1982.5	3.724	0.073	22.602	2.426
18SPR1B03	1984	3.964	0.081	24.207	2.498
17SPR1B02	1985	4.059	0.059	25.841	2.674
16SPR1B01	1986	3.691	0.051	36.873	3.584
15SPR1ABot	1987.5	4.033	0.051	33.622	2.750
14SPR1A1516	1989.5	3.675	0.041	34.266	2.938
13SPR1A14	1991	3.445	0.042	27.997	2.974

Sample Name	Year	^{127}I (ppm)	^{127}I error	$^{127}\text{I}/^{129}\text{I}$ ($\times 10^{-12}$)	$^{127}\text{I}/^{129}\text{I}$ error ($\times 10^{-12}$)
Parola (continued)					
12SPR1A13	1992	3.665	0.033	31.994	3.377
11SPR1A12	1993	3.572	0.054	24.412	3.438
10SPR1A11	1994	3.758	0.083	33.542	2.699
09SPR1A10	1995	3.351	0.043	29.922	2.888
08SPR1A09	1996	4.008	0.108	37.272	3.405
07SPR1A08	1997	4.052	0.036	34.106	3.201
06SPR1A07	1998	3.838	0.092	25.550	2.570
05SPR1A06	1999	3.978	0.091	36.825	3.453
04SPR1A05	2000	3.828	0.099	22.850	2.239
03SPR1A04	2001	3.731	0.104	35.128	2.996
02SPR1A03	2002	3.597	0.066	38.921	4.144
01SPR1A02	2003	4.112	0.015	29.254	2.762

Appendix B. $\Delta^{14}\text{C}$ and corresponding errors (1σ).

Sample Name	Year	$\Delta^{14}\text{C}$ (‰)	$\Delta^{14}\text{C}$ error (‰)	Sample Name	Year	$\Delta^{14}\text{C}$ (‰)	$\Delta^{14}\text{C}$ error (‰)
Baler				Parola			
BA50	1956	-56.3	4.2	SC01	1953.5	-67.8	6.1
BA49	1957	-56.4	3.0	SC02	1954.5	-67.8	6.0
BA48	1958	-56.8	4.6	SC03	1955.5	-75.5	6.2
BA47a	1959	-48.0	3.6	SC04	1956.5	-64.9	6.4
BA47b	1960	-57.7	5.3	SC05	1957.5	-90.1	9.3
BA45	1961	-37.3	3.4	SC06	1958.5	-60.2	6.2
BA43a	1962	13.8	3.8	SC07	1959.5	-45.2	6.6
BA43b	1963	-24.6	3.9	SC08	1960.5	-44.1	6.6
BA42	1964	-40.3	3.6	SC09	1961.33	-57.1	7.1
BA41	1965	-31.1	3.9	SC10	1961.66	-18.1	6.6
BA40	1966	-8.2	3.6	SC11	1962.5	-5.5	6.8
BA39	1967	-14.3	4.9	SC12	1963.5	2.5	6.8
BA38	1968	16.1	3.6	SC13	1964.5	17.2	6.7
BA37	1969	59.5	3.7	SC14	1966	49.8	6.8
BA36	1970	89.4	3.6	SC15	1966.5	75.2	6.8
BA34	1972	122.3	3.7	SC16	1967	100.9	7.1
BA33	1973	130.5	4.7	SC18	1968.5	148.0	7.2
BA32	1974	110.0	3.7	SC19	1969	147.7	7.2
BA31	1975	144.8	4.9	SCbot	1970	158.1	7.2
BA30	1976	184.6		SBbot	1971.5	162.9	7.3
BA29	1977	189.3		SB15	1973	155.8	7.1
BA28	1978	166.4	3.4	SB14	1974	160.2	7.1
BA27	1979	157.6	3.6	SB12	1976	158.4	
BA26	1980	152.8	3.6	SB11	1977	137.0	
BA25	1981	163.1	5.0	SB10	1977.33	135.9	
BA24	1982	130.2	4.6	SB09	1977.66	144.9	
BA22	1984	143.8	3.6	SB08	1978.5	154.5	7.2
BA21	1985	136.4	3.6	SB07	1979.5	127.7	7.3
BA18	1988	127.7	3.5	SB06	1980	144.2	7.3
BA17	1989	124.2	3.7	SB05	1981	135.9	3.7
BA15-16	1990.5	118.9	3.6	SB04	1982.5	131.4	3.9
BA13-14	1992.5	104.0	4.3	SB03	1984	133.2	3.9
BA12	1994	101.8	4.0	SB02	1985	120.7	3.8
BA11	1995	100.7	4.2	SB01	1986	130.4	4.1
BA10	1996	99.9	4.1	SAbot	1987.5	114.9	4.1
BA09	1997	96.2	4.3	SA16	1989	120.0	3.7
BA07-08	1998.5	76.0	4.8	SA15	1990	116.6	3.8
BA06	2000	76.9	4.5	SA14	1991	108.2	4.1
BA05	2001	75.0	4.4	SA13	1992	102.5	3.9
BA04	2002	65.2	6.2	SA12	1993	101.5	3.9
BA03	2003	77.2	5.1	SA11	1994	108.0	3.9
				SA10	1995	89.9	3.9
				SA09	1996	89.5	4.3
				SA08	1997	81.8	4.3
				SA07	1998	82.3	4.3
				SA06	1999	88.2	4.5
				SA05	2000	57.7	5.8
				SA04	2001	74.2	4.6
				SA03	2002	72.8	5.1

Appendix C. ^{129}I in Greenland SE-Dome ice core and corresponding errors (1σ).

Sample code	h water (m)	estimated age (year)*	I^{129} in ice (10^3 atoms / mL H_2O)	1σ error
SE-139	42.14	1972.9	10.11	0.82
SE-140	42.52	1972.5	3.84	0.39
SE-141	42.90	1972.1	9.98	0.75
SE-142	43.26	1971.7	21.59	1.84
SE-143	43.61	1971.4	4.58	0.42
SE-144	44.03	1971.0	12.89	0.92
SE-145	44.45	1970.6	8.72	0.76
SE-146	44.77	1970.2	11.58	0.80
SE-147	45.18	1969.8	14.64	1.04
SE-148	45.52	1969.5	7.62	0.58
SE-149	45.93	1969.1	21.08	1.24
SE-150	46.30	1968.7	12.07	0.88
SE-151	46.71	1968.3	8.55	0.63
SE-152	47.08	1967.9	12.13	0.87
SE-153	47.45	1967.5	7.86	0.65
SE-154	47.86	1967.1	8.94	0.85
SE-155	48.22	1966.8	5.62	0.51
SE-156	48.61	1966.4	6.91	0.64
SE-157	49.01	1966.0	7.98	0.72
SE-158	49.42	1965.6	9.60	0.77
SE-159	49.78	1965.2	11.09	0.90
SE-160	50.20	1964.8	9.52	0.61
SE-161	50.59	1964.4	6.85	0.59
SE-162	50.99	1964.0	10.67	0.79
SE-163	51.39	1963.6	18.70	1.20
SE-164	51.78	1963.2	21.13	1.34
SE-165	52.18	1962.8	29.81	1.67
SE-166	52.59	1962.4	39.79	2.25
SE-167	52.98	1962.0	37.93	2.14
SE-168	53.38	1961.6	17.84	1.16
SE-169	53.75	1961.3	35.99	1.89
SE-170	54.16	1960.8	16.36	1.24
SE-171	54.59	1960.4	21.78	1.46
SE-172	54.99	1960.0	10.44	0.83
SE-173	55.39	1959.6	6.93	0.76
SE-174	55.80	1959.2	5.58	0.54
SE-175	56.18	1958.8	5.04	0.46
SE-176	56.61	1958.4	8.62	0.77

*based on an accumulation rate of 1 m/yr

Appendix C (continued).

Sample code	h water (m)	estimated age (year)*	I¹²⁹ in ice (10³ atoms / mL H₂O)	1σ error
SE-177	57.05	1958.0	6.14	0.60
SE-178	57.42	1957.6	8.51	0.72
SE-179	57.83	1957.2	15.84	1.10
SE-180	57.98	1957.0	5.19	0.56
SE-181	58.43	1956.6	2.82	0.45
SE-182	58.69	1956.3	4.91	0.60
SE-183	59.09	1955.9	5.40	0.64
SE-184	59.50	1955.5	5.10	0.62
SE-185	59.91	1955.1	7.36	0.69
SE-186	60.32	1954.7	4.71	0.49
SE-187	60.63	1954.4	5.15	0.61

*based on an accumulation rate of 1 m/yr